Factors Affecting the Resolution of Photopolymerized Ceramics

by

Susan Patricia Gentry

A dissertation submitted in partial fulfillment
of the requirements for the degree of
Doctor of Philosophy
(Materials Science and Engineering)
in The University of Michigan
2012

Doctoral Committee:

Professor John W. Halloran, Chair
Professor John Edmond Allison
Professor Brian J. Love
Professor Michael J. Solomon
Professor Suman Das, Georgia Institute of Technology

To God alone be the glory, forever and ever. Amen.

Acknowledgements

I would like to thank my thesis advisor, Prof. Halloran, for his support. I have learned much about all things ceramic from him, and am thankful for the opportunities to gain experience and a breadth of knowledge in ceramics. Specifically, I am also thankful for the encouragement and freedom to look at linewidth in photopolymerizable ceramic suspensions, after years of trials with the stereolithography machine. Furthermore, I appreciated the encouragement to pursue interests outside of my academic work. Four years after I began graduate school, I realize that one of the best decisions I made was choosing a good advisor.

This work was primarily funded by a sponsored research project through Honeywell. I am grateful for the help of my colleagues there (Wil Baker, Dennis Wolski, and Dr. Daira Legzdina) for providing me the opportunity to visit their facilities several times to work with them and learn from them. They have taught me much about airfoils, stereolithography, and the airfoil industry. I would also like to acknowledge my other collaborators on the stereolithography and LAMP projects: Prof. Suman Das and his research group at Georgia Institute of Technology, Walt Zimbeck at Technology Assessment & Transfer, Inc., and Don Deptowicz and others at PCC Airfoils. Thank you for all of the help at various stages of this project, from sharing your knowledge of 3D printing to producing molds and castings for the project.

My labmates also deserve recognition. Pertaining directly to this thesis, Dr. Vladislava Tomeckova provided the experimental sedimentation data used in Chapter 4, and a photograph of a ceramic mold built by Dr. Chang-Jun Bae was included in Chapter 3. Beyond that, the conversations at group meetings and in the office provided many ideas to pursue with my research. From the helpful conversations at work to the camaraderie outside work, it has been a pleasure to work alongside the past and present members of the Halloran group.

And finally, I would like to thank my friends, family, and church family for their support these four years. There have been plenty of ups and downs throughout graduate school, situations where looking back I still don't know whether to laugh or to cry, and I am grateful for your companionship, encouragement, and fun times. Thank you for the perspective you provide, that my identity is not wrapped up in my research or graduate school, "but our citizenship is in heaven. And we eagerly await a Savior from there, the Lord Jesus Christ" (Philippians 3:20).

Table of Contents

List of Figures

List of Tables

Abstract

Direct digital manufacturing of ceramic parts is possible using focused ultraviolet (UV) light to pattern photopolymerizable ceramic suspensions. Ultimate spatial resolution is limited by the size of the UV beam. This dissertation focuses on other limiting factors. First, machine parameters and software can limit practical resolution of the processes. Second, if particle settling occurs, this can change the curing parameters. The effects of sedimentation on curing are modeled by combining the absorption model of sensitivity, the inhibitor exhaustion model for critical energy dose, and the Richardson-Zaki model of Stokes' settling for monodisperse spheres. Finally, resolution can also be limited by "broadening", where the width of a cured line is larger than the size of the UV beam.

To understand the physics of broadening, the effect of energy dose on the cure depth and cure width was determined. It is shown that the cure depth fits the expected Beer-Lambert behavior, where cure depth increases with the logarithm of energy and is described by the sensitivity and critical energy dose. The broadening can be described by the excess width, which fits a quasi-Beer-Lambert behavior as well. The absorption model predicts the effect of photoinitiator and dye on the cure depth, and this model can also be used to describe the excess width. Similarly, the inhibitor exhaustion model predictions for depth can be used to describe the excess width. The broadening depth is defined as the depth of cure when broadening begins. This is given by the cure depth

where the energy dose is equal to the width critical energy dose. Below this broadening depth, no broadening is expected. It is shown that the broadening depth is proportional to the logarithm of the refractive index contrast between the ceramic powder and the liquids in solution. The role of contrast is understood in terms of the total path length in the absorption model using a random walk model. Tracing the photon paths using a hindered random walk model provides insight into the broadening behavior. Accounting for the angular distributions of scattering angles shows that broadening occurs at the expense of the cure depth.

Chapter 1

Introduction to 3D Printing of Investment Casting Molds

1.1 History of Manufacturing

Manufacturing has evolved out of the need for faster and more reproducible production of items. Handcrafts use skilled labor to build parts, whereas manufacturing has found ways to improve this process. As early as 1799, Eli Whitney wrote that the future of manufacturing would feature "expedition, uniformity, and exactness".[1] The American system of manufacture of the 19th century had several characteristics that differed from handcrafts. The labor was increasingly divided, so that workers only handled a portion of the final part. This meant that laborers did not need to be as skilled to complete their portion of their job. Instead, specialized equipment was used in the manufacturing process. Another key advance was the idea of interchangeable, standardized parts. These were visible in the armament industry, as the guns began to contain identical parts so that they could easily be repaired from a box of spare parts. As summed up by the historian Ruth Schwartz Cowan, "the American system of manufacture was the foundation of what would subsequently be called mass production for a mass market."[1] The 20th century featured great gains to improve the speed, reliability, and cost of manufacturing. In the past, manufacturing was largely focused on processes for a large number of parts, ignoring the need for unique or small batch parts in certain applications.

An area of innovation for the 21st century is the mass production of personalized or single use parts which are built directly from computer aided drawing (CAD) files. This process is known as direct digital manufacturing (DDM). In traditional manufacturing, the setup costs can be high as dies must be created for the process. For small runs, these sunk costs do not get spread over a large number of parts, resulting in a high cost per part. In direct digital manufacturing, the CAD file varies between parts, without the need for dies for each design. This is important in areas such as biomedical implants, which need to be fabricated to precisely fit a person's body. All bodies are different shapes and sizes, so the manufacturing must be versatile. A notable modern example of this is the Invisalign® orthodontic appliances. The company produces a series of retainers which fit over a patient's teeth and gradually move them, replacing the need for braces. A series of these retainers are required for each patient, based off of computer models of their mouth. Using DDM, the retainers can be directly built from the CAD files generated by the dental software. Over 30 million individually customized aligners have been manufactured, each with a slightly different geometry. Computers have allowed for the visualization of unique, precise designs that would be difficult to produce individually, with direct digital manufacturing needed to produce a large number of parts with unique designs.

Recent gains have been made in direct digital manufacturing, with the field of three-dimensional printing (3D printing) becoming part of common parlance. To recognize the current relevance of digital manufacturing, one does not need to go any farther than *The New York Times* or *The Economist*. The September 14, 2010 edition of *The New York Times* contained a front-page article titled "3-D Printing Spurs a

Manufacturing Revolution."[2] An April 21st, 2012 special report in *The Economist* focused on "manufacturing and innovation", with the cover article titled "The third industrial revolution". In *The Economist* article, it was suggested that these manufacturing innovations will lead to the "Third Industrial Revolution."[3] Numerous table-top machines are now commercially available, such as the MakerBot Replicator which was priced for $1,749 as of June 10, 2012.[4] These table-top machines generally print simple designs from a variety of plastic compounds. Alternatives include printing food, such as the Choc Creator by Choc Edge, which can be used to print chocolate designs from CAD files.[5] The field of direct digital manufacturing is very current, with a variety applications.

1.2 Application: Ceramic Molds for the Investment Casting of Airfoils

One specific application that is in need of a revolution is that of the manufacturing process for single crystal airfoils. The April 21, 2012 special report in *The Economist* (referenced previously, suggesting that 3D printing will lead to the third industrial revolution) also contains an artful description of airfoils as a technology that will benefit from 3D printing:

> It is small enough to be held in your hand and looks like an unremarkable chunk of metal perforated with tiny holes, but it is fiendishly hard to make. That is because it must spin 12,000 times a minute under high pressure at a temperature of 1,600°C, 200°C above the melting point of the material it is made from. And it must survive that twisting inferno long enough to propel an airliner for 24m km (15m miles) before being replaced. In all, 66 of these stubby blades are used in the rear turbine of a Rolls-Royce Trent 1000 engine, and the British company makes hundreds of thousands of these blades a year.[6]

As will be discussed in this work, modern airfoil designs are very complex and in need of a new manufacturing method.

Desires to increase the operating temperatures of engines have led to innovations in airfoil design. Increasing the operating temperature of engines increases their theoretical maximum efficiency. This has pushed engineers to develop alloys with higher and higher melting points. Additionally, the airfoils in the hottest section of the engine now have hollow designs which allow for cooling air to flow through them, preventing damage to the airfoil from the high heat.[7] Some of this cooling air flows through the main section of the blade, and out of trailing edge of the blade. However, the cooling also comes from film cooling. Some of the cooling air flows out of film cooling holes on the leading edge of the blade, flowing over the outer surface of the blade as it rotates. This provides a thin layer of cool air between the hot combustor air and the delicate airfoil. The complex features of modern airfoils are necessary so that they can be used at temperatures above the melting point of their alloy. The active cooling in a turbine airfoil requires extremely complex interior and exterior features.

The fine features in the ceramic molds have dimensions on the order of hundreds of microns. Figure 1.1 shows the key features and their dimensions. The shell mold forms the exterior of the surface, while the ceramic core forms the complex cooling passages. Note that the shell mold in the figure has had a section removed so that the interior core can be seen. It is important to remember that solid parts in the mold become air gaps in the cast part, and gaps in the mold correspond to metallic regions in the cast part. Thus, the 460 μm diameter leading edge film cooling *rods* in the ceramic core will correspond to 460 μm diameter leading edge film cooling *holes* in the cast airfoil. The

smallest features are the flag tips which are 360 μm thick. These dimensions provide a basis for the optimal resolution that is needed for the direct digital manufacturing of these parts.

Currently airfoil molds are made through a lost wax process with embedded cores. Ceramic cores are made through injection molding a ceramic/wax binder mixture into a die, typically using zircon ($ZrSiO_4$) as the ceramic powder. These green cores undergo binder removal and are fired. They are then prepared and placed into dies for the lost-wax process. The lost wax process is detailed in a 1958 patent by Operhall *et al.*, describing the dip coating of the ceramic slurry onto wax designs.[8] Figure 1.2 shows a schematic of the lost wax process.[9] Wax is injected into a die which holds the ceramic core, forming a wax pattern with the shape of the airfoil. The wax pattern is dipped into ceramic slurries to form the shell mold on the exterior of the wax pattern. The shell is usually made of silica (SiO_2) with a variety of particle size distributions. Removing the wax and firing produces the ceramic investment casting mold for airfoils, with a shell mold containing the ceramic core. One major disadvantage of the lost-wax process is the money and time required to produce new casting designs. At a minimum, modifying a design requires new dies for the injection molding of cores and new dies for the wax injection around the mold. New airfoil designs tend to be fairly conservative as a result of the complexity required to adjust designs within the lost-wax process. A new process is needed which can produce casting molds without the need for tooling of expensive, precise dies for the cores and wax patterns.

It is important to remember that although the research can be applied to a variety of designs, the aviation industry has specific objectives that they must meet. The focus of

this project has been on that of airfoils for turbine engines. A key question to ask is: Do molds meet specifications required for application? The key issues for the application of airfoil molds are as follows:

- The process must be able to build many different mold designs. There are other methods that can still be used for large identical runs, but the impetus for DDM is for small runs and prototype designs.
- There must be predictable shrinkage, with no warping or cracking of the molds.
- The molds must have adequate mechanical properties to withstand single crystal superalloy casting, which occurs around 1600°C and can take up to 8 hours.
- Adequate resolution must be achieved, as defined as surfaces within 50 μm of specification.

Fulfilling these criteria will be important for a new manufacturing method to replace the lost wax method.

1.3 Direct Digital Manufacturing by Photopolymerization

While there are many competing methods of direct digital manufacturing, this dissertation will discuss the use of two layer-by-layer photopolymerization techniques: ceramic stereolithography and large area maskless photopolymerization (LAMP).[10] For simplicity, the remaining chapters will focus on stereolithography, but it should be noted that advances in stereolithography are generally applicable to LAMP. Both of these are layer-by-layer additive manufacturing processes, meaning that the design is constructed from the bottom-up, building layers on top of each other. For example, Figure 1.3 shows a CAD airfoil mold (A) and some of the corresponding slices (B). Each layer is formed through photopolymerization, selectively curing a liquid suspension into a hard plastic. Cumulatively, these layers lead to a green part with the geometry specified in the CAD file. Figure 1.4 shows the part at three of the stages: CAD file of the mold design, the green mold that has been built, and the metallic part after investment casting.

These basic steps will be the same for both stereolithography and LAMP, as they are both layer-by-layer photopolymerization processes.

1.3.1 Stereolithography

Stereolithography is a commercially available photopolymerization process that is commonly used for 3D printing and rapid prototyping. To produce ceramic parts, a ceramic suspension containing monomers and photoinitiator are used in place of the commercial resin. An ultraviolet (UV) laser is used to scan across the surface of the suspension, causing localized curing of the suspension. These green parts are then fired to create sintered ceramic parts. Chapter 2 will discuss in detail the process of building parts with ceramic stereolithography. This process was previously shown to be capable of producing investment casting molds by Chang-Jun Bae.[11; 12] However, more work was needed to achieve the necessary resolution, which is the focus of the research in this dissertation.

1.3.2 Large Area Maskless Photopolymerization (LAMP)

LAMP is a photopolymerization process that is being developed collaboratively by the Suman Das group at the Georgia Institute of Technology and the John Halloran group at the University of Michigan. For a schematic of the LAMP machine, see Figure 1.5. The light source of LAMP is a UV bulb that illuminates a digital mirror device (DMD). The DMD contains an array of micro-mirrors, which form pixels that reflect the light onto the surface of the suspension. These mirrors are rotated between an “on” and “off” position to provide the two-dimensional shape that is polymerized. This

polymerizes a selected area at once, in contrast to the stereolithography beam which must raster back and forth across the surface. Similar to stereolithography, a recoating system is needed to provide a fresh layer of suspension to the surface. When fully developed, LAMP should produce parts much faster than ceramic stereolithography by replacing the laser rastering with flash illumination. Due to the similarities of the photopolymerization processes, it is expected that the chapters in this dissertation on stereolithography will also be fruitful for LAMP.

1.4 Conclusion

Much advancement has been made in the field of manufacturing, with current interest focusing on developing unique parts directly from digital files. One such area is the development of airfoils for turbine engines. Airfoils feature complicated designs to promote active cooling of the blade. This thesis will focus on the ceramic molds that are used for the investment casting of airfoils, which have features as small as 360 μm. These molds can be produced through photopolymerization processes such as ceramic stereolithography and large area maskless photopolymerization (LAMP). This work will primarily focus on ceramic stereolithography, although the work on suspension characterization (Chapters 4-6) is applicable to both processes.

1.5 References

[1] R. S. Cowan, "A social history of American technology," pp. 342. Oxford University Press: New York, (1997).
[2] A. Vance, "3-D Printing Spurs a Manufacturing Revolution." *The New York Times*, September 14, 2010.

[3] "The third industrial revolution," pp. 15. *The Economist*, **Vol. 403**. [8781], April 21, 2012.
[4] "MakerBot," http://www.makerbot.com, Accessed June 10, 2012.
[5] "Choc … Revolutionise Chocolate Making," http://www.chocedge.com, Accessed June 10, 2012.
[6] "Materials: Forging Ahead," pp. 11-13 (Special Report). *The Economist*, **Vol. 403**. [8781], April 21, 2012.
[7] H. A. Weldon, "Coolable turbine airfoil," Patent 4063851 (1977).
[8] T. Operhall, C. W. Schwartz, and D. Van Schoik, "Ceramic Metal Casting," Patent 2961751 (1960).
[9] R. A. Horton, "Investment Casting," pp. 646-61 in *ASM Handbook,* **Vol. 15.** ASM International, 2008.
[10] J. W. Halloran, V. Tomeckova, S. Gentry, S. Das, P. Cilino, D. J. Yuan, R. Guo, A. Rudraraju, P. Shao, T. Wu, T. R. Alabi, W. Baker, D. Legdzina, D. Wolski, W. R. Zimbeck, and D. Long, "Photopolymerization of powder suspensions for shaping ceramics," *Journal of the European Ceramic Society,* **31**[14] 2613-19 (2011).
[11] C.-J. Bae, "Integrally Cored Ceramic Investment Casting Mold Fabricated by Ceramic Stereolithography," Ph.D. Dissertation, University of Michigan, (2008).
[12] C.-J. Bae and J. W. Halloran, "Integrally Cored Ceramic Mold Fabricated by Ceramic Stereolithography," *International Journal of Applied Ceramic Technology* (2010).

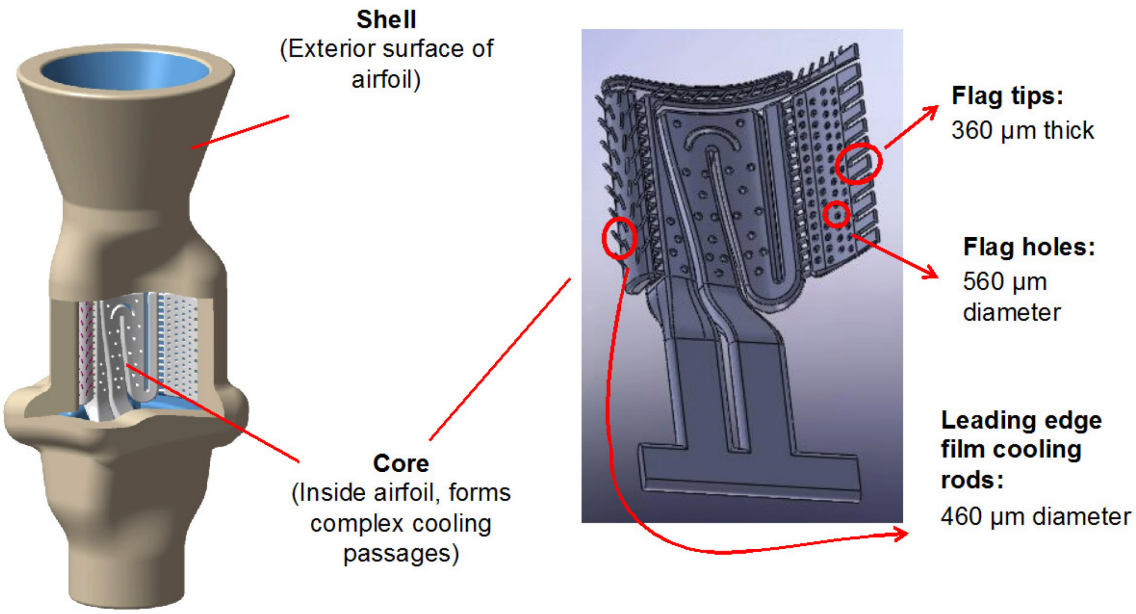

Figure 1.1 Schematic showing the key features in both the core and the shell of the mold.

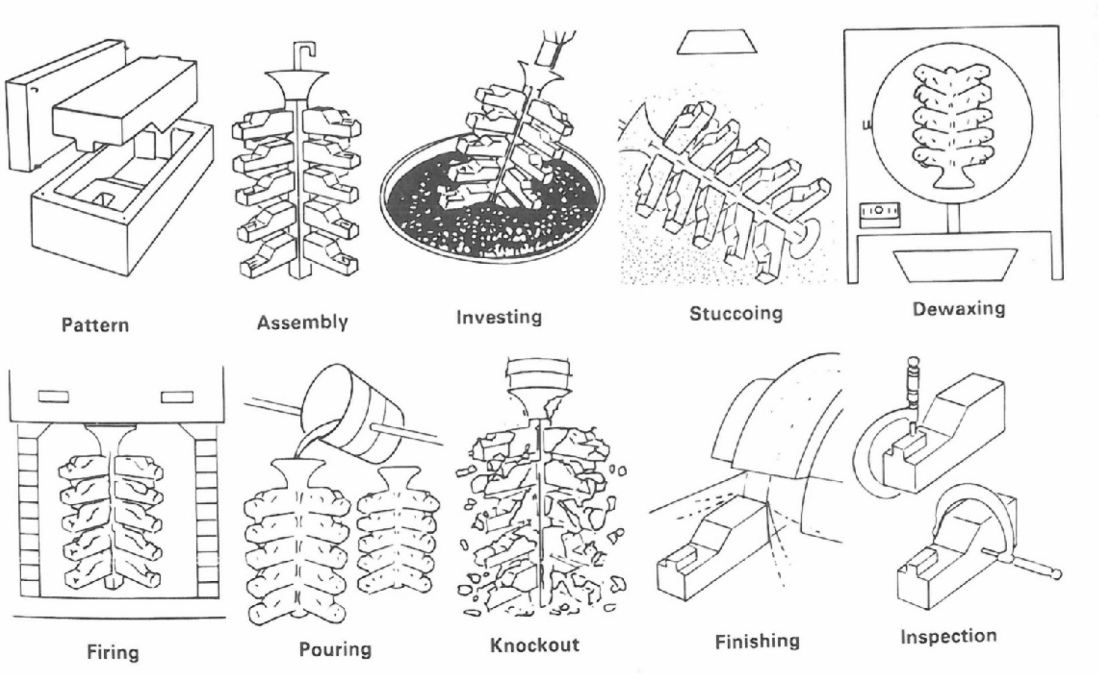

Figure 1.2 Schematic showing the steps in the lost wax process.[9]

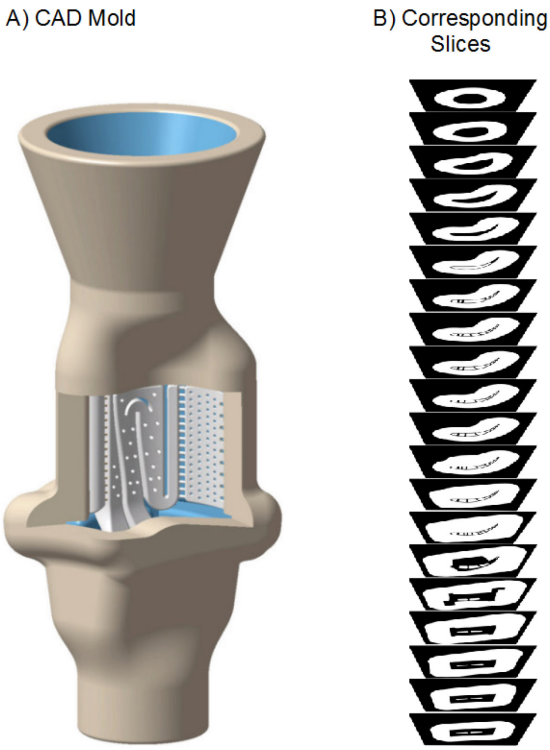

Figure 1.3 Example of a CAD design (A) along with some of the corresponding slices (B).

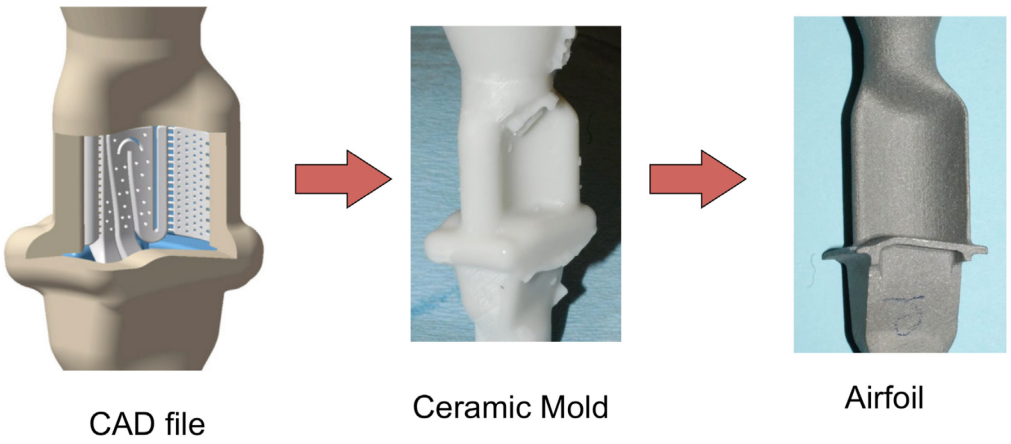

Figure 1.4 Images showing part at different stages: CAD file, ceramic mold, and airfoil (pre-machining).

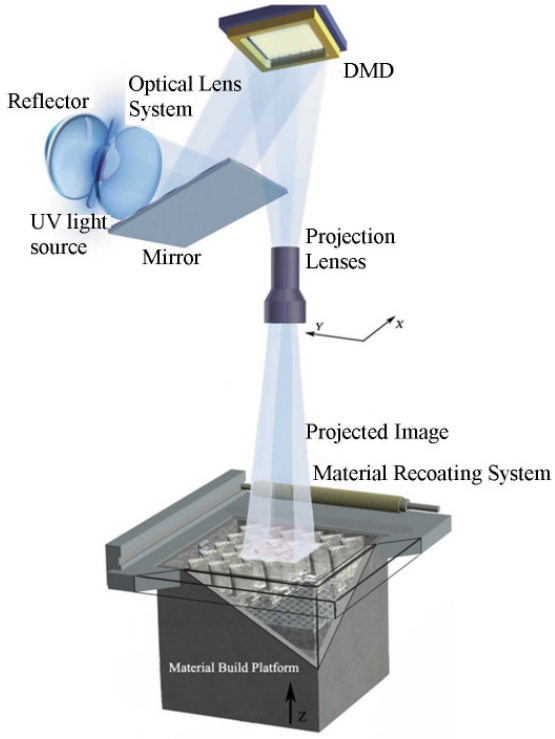

Figure 1.5 Diagram of a machine used for large area maskless photopolymerization (LAMP).

Chapter 2

Overview of Ceramic Stereolithography

2.1 Overview

As introduced in Chapter 1, ceramic stereolithography builds green bodies in a layer-by-layer fashion through photopolymerization. Stereolithography is a commercially available process for creating parts directly from computer aided drawing (CAD) files. Ceramic stereolithography replaces the commercial stereolithography resins with ceramic suspensions. It is important to better understand the fundamentals of ceramic stereolithography so that the resolution of the process can be improved. This chapter will provide an overview to the process, while later chapters will focus on specific methods of improving the resolution of ceramic stereolithography for airfoils.

While there are a variety of ceramic stereolithography apparatuses (SLAs) available, this dissertation will focus on two machines produced by 3D Systems: the SLA-250 and Viper systems. Both of these use an ultraviolet (UV) laser to selectively polymerize the surface of a ceramic suspension. Figure 2.1 contains a schematic of stereolithography machines such as the SLA-250 or Viper. The laser is focused onto a mirror unit, which directs the laser across the surface of the photopolymerizable ceramic suspension contained in the vat. The laser results in localized curing of the ceramic suspension, which forms the layer of the part. The part is built on a platform connected to the elevator, which raises and lowers the part as commanded by the build file. The

main difference between the two machines is that the Viper is an updated SLA compared to the SLA-250, featuring a smaller beam size and minimum layer thickness. A more detailed comparison of these systems is given in Table 2.1.

The ceramic stereolithography process used by both machines is the same, with the process flow diagram given in Figure 2.2. Note that the chapter sections are included in the left column of the process flow chart for reference. Briefly, the file for the design is prepared into a format that is appropriate for the machine. Suspension is prepared and mixed by rolling in a plastic bottle for 24-48 hours. The part is built from the ceramic suspension, resulting in a "green" part that has cured polymer binder holding together the ceramic particles. The part is then removed from the ceramic suspension and rinsed. Finally, the "green" part is fired, pyrolizing the organic binder and resulting in sintering of the ceramic particles. This yields the ceramic part. The status of the part at each stage is also given in Figure 2.2, to show the transformation of the uncured ceramic suspension to a sintered ceramic part. Figure 2.3 contains illustrations of the part at each of these stages (suspension, green part in suspension, "green" part with polymer, and sintered ceramic object with sintering shrinkage). These steps will be explained in further detail in the remainder of this chapter.

2.2 File Preparation

The process of converting a CAD design into a build file can be easy to overlook for materials scientists, although this is not trivial. It is important to understand these steps, as will be shown in Chapter 3. Any information lost at a step will not be recovered later. These steps are shown in Figure 2.4, using a sphere as the sample design. First, the

three-dimensional design is created using a CAD program such as SolidWorks or CATIA (Figure 2.4A). These generate files in the non-uniform rational basis spline (NURBS) format, which approximates the surface as a series of smooth curves. The most accurate resolution is at this stage, as additional steps can lead to the loss of information. The NURBS file is then saved into surface tesselation language (STL) format (Figure 2.4A). This approximates the smooth surfaces of the NURBS format as a set of triangles on the surface. The x, y, and z locations of the triangle vertices are noted as well as the surface normal (to define "interior" and "exterior"). The curves of the sphere are transformed into flat edges, losing the smoothness of the surface. The tessellation algorithm can vary the number and size of the triangles. Increasing the number of triangles (decreasing their size) improves the resolution of features and is more accurate for curved surfaces. However, this also increases the file size, which can become unwieldy for complicated shapes such as airfoil casting molds. The STL file is then loaded into a stereolithography preparation software such as 3D Lightyear 1.5.2 (3D Systems, Valencia, CA). This program divides the STL file into a series of slices, where each slice has a constant thickness given by the layer thickness (Figure 2.4C). In the sphere example, the layer thickness is 100 μm. Note that ideally the slices will be a series of circles with radius varying based on the height in the sphere. However, due to tessellation, these will actually be a series of polygons. The next step is the creation of the vector file, when the laser commands are assigned for each of the slices (Figure 2.4D). Depending on the precision of the drawing mechanism for the laser and the precision of the algorithm, these could result in a series of even more angular polygons for the "sphere" when compared with the slices. Finally, the vector files are used by an SLA to build a part (Figure 2.4E).

The laser causes a photochemical reaction, curing individual layers which are built on top of each other. It can be seen that the built shape can lose some resolution at each step, with the sphere in Figure 2.4A smoother than the built part in Figure 2.4E. Understanding these processes will be important to improving the resolution of ceramic stereolithography.

2.3 Suspension Preparation

Traditional stereolithography uses photopolymerizable resins. The basic components of these are monomers/oligomers, photoinitiators, and UV absorbers. The photoinitiator releases free radicals when illuminated by a sufficient dose of light. These free radicals then cause the polymerization of the monomers/oligomers, forming plastic parts. UV absorbers are included to control the photopolymerization reaction of the system. Since the final product is a plastic part, commercial resins contain oligomers in place of monomers to improve the plastic properties and reduce polymerization shrinkage. These oligomers make the liquid a viscous resin. These resins are commercially available, such as the Somos resins produced by DSM.

Ceramic stereolithography suspensions are not commercially available, and instead must be developed using similar components as commercial resins. Slight modifications are made to the ingredients because of the presence of the ceramic powders. Suspensions for ceramic stereolithography typically include monomers, photoinitiator, UV absorber, ceramic powder at high solids loading (50-65 vol%), and dispersant. Similar to commercial resins, the photoinitiator and UV absorber are included to control the photopolymerization of the monomer due to the reaction of the

photoinitiator. The formulation for ceramic stereolithography must include a low viscosity monomer, so that the suspension will easily flow. Although monomers have a higher polymerization shrinkage than oligomers, it is necessary to use monomers for rheological reasons. Typically, a mixture of bifunctional and tetrafunctional monomers are used, such as the bifunctional 1,6 hexanediol diacrylate (HDDA) and the tetrafunctional ethoxylated pentaerythritol tetraacrylate (EPETA). Note that their chemical structures are given in Figure 2.5.

Suspensions require 24-48 hours for preparation. The monomer(s), dispersant, and UV absorber are combined and mixed together for several minutes, as these are all liquid ingredients. Next, the photoinitiator is added, mixing for 15 minutes until it has fully dissolved in the liquid solution. Finally, the powder is added. For highly loaded (50-65vol%) suspension, the powder is added incrementally in two or three batches, to allow for full incorporation. The ceramic suspension is then milled or rolled for 24-48 hours to allow for further homogenization of the suspension.

2.3.1 Rheology

The suspension rheology is important to consider for ceramic stereolithography. A suspension with a high viscosity will not mix well nor will flow well during recoating. The effect of monodisperse particles on the rheology of a suspension has been modeled by Krieger and Dougherty.[1] It has been shown that the suspension viscosity can be modeled as

$$\eta = \eta_0 \left(1 - \frac{\beta\Phi}{\Phi_0}\right)^{-n_{KD}\Phi_0} \qquad \text{Eq. 2.1}$$

where η is the viscosity of the suspension, η_0 is the viscosity of the solvent, β is the effective packing factor of the ceramic powder due to the dispersant on the surface, Φ is the volume fraction of powder in the suspension, Φ_0 is the Krieger-Dougherty limit (corresponding to the maximum packing fraction of the particles), and n_{KD} is a fitting parameter related to the intrinsic viscosity. The maximum packing for uniform spheres is 0.74 (assuming a closed packed lattice). Since the arrangement of the particles is random, it is expected that the maximum packing fraction will be around 0.64.[2] Note that in the polydispersed case, the Φ_0 can be higher, following the well-known Furnas-type relations. Thus, it is expected that the viscosity will increase significantly for the solids loadings used in ceramic stereolithography (typically Φ=0.60). Chu confirmed that the Krieger-Dougherty limit is significant for ceramic stereolithography suspensions.[3] Additionally, the Krieger-Dougherty limit demonstrates the significance of using a low-viscosity monomer. The viscosity of the suspension will scale with the viscosity of the solvent (in this case the monomer). Since high solids loadings are needed to produce sufficiently dense green bodies, low viscosity monomers must be used to minimize the overall suspension viscosity.

2.4 Stereolithography Photopolymerization of Commercial Resins

Stereolithography uses an ultraviolet laser to control the polymerization of monomers. The photoinitiator releases free radicals when illuminated with sufficient dose of light. The absorbance of photoinitiators is wavelength dependent, so the photoinitiator is chosen based on the wavelength and intensity of the light source. The

free radicals react with the monomer to result in localized polymerization. Thus, the laser must be directed across the surface of the suspension to result in a cured layer.

2.4.1 Resin Characterization

Stereolithography resins are characterized by their photocuring properties. The photopolymerization process is well-understood for commercial resins without powder. Commercial resins can be classified as Beer-Lambert absorbers. This means that energy attenuates logarithmically through the suspension as

$$E(z) = E_0 \exp\left(\frac{-z}{S_d}\right) \qquad \text{Eq. 2.2}$$

where E_0 is the incident energy dose, z is the depth below the surface, and S_d is the "resin sensitivity", which is an attenuation length. Curing occurs locally wherever the dose is above the "critical energy dose" for polymerization, E_d. Thus, the cure depth, C_d, can be defined as the depth at which the local energy dose (E) is equal to the critical energy dose (E_d), or

$$E(z = C_d) = E_d = E_0 \exp\left(\frac{-C_d}{S_d}\right) \qquad \text{Eq. 2.3}$$

More generally, the cure depth can be predicted assuming that the energy dose (E_0) is known

$$C_d = S_d \ln\left(\frac{E_0}{E_d}\right) \qquad \text{Eq. 2.4}$$

The critical energy dose and the sensitivity can be determined from a semilogarithmic plot of the cure depth as a function of energy dose.

2.4.2 Jacobs' Model for Cure Shape

Stereolithography laser beams are usually modeled as having Gaussian intensity distributions, which is the ideal spatial distribution for monomodal beams.[4] A Gaussian beam of width W_o and peak intensity I_{max} has an intensity distribution at the surface which is

$$I(y, z = 0) = I_{max} \exp\left(\frac{-2y^2}{W_0^2}\right) \qquad \text{Eq. 2.5}$$

where y is the distance from the center of the beam and z is the depth from the surface of the suspension. The energy dose at the surface is simply equal to the intensity multiplied by the illumination time (E=I*t). Since time is independent of position, the energy distribution at the surface will have the same shape as the intensity distribution. That is,

$$E(y, z = 0) = E_{max} \exp\left(\frac{-2y^2}{W_0^2}\right) \qquad \text{Eq. 2.6}$$

where E(y,z=0) is the energy at the surface at distance y from the center of the beam, and E_0 is the energy dose at the center of the beam. Since the resin is assumed to be a Beer-Lambert absorber, the energy decreases exponentially as a function of depth. Thus, combining Eq. 2.2 and Eq 2.6 gives the energy distribution within the suspension as

$$E(y, z) = E_{max} \exp\left(\frac{-2y^2}{W_0^2}\right) \exp\left(\frac{-z}{S_d}\right) \qquad \text{Eq. 2.7}$$

Eq. 2.7 can be used to predict the energy at any point within the resin, assuming that the laser is drawing along the x-axis.

Curing occurs by illuminating the suspension for a known period of time, with polymerization confined to the areas where the energy exposure is greater than or equal to the critical energy for polymerization (E_d). The cross-sectional cured shape can be

assumed to be the locus of points where E(y,z)=E_d. It is predicted that a Gaussian source will result in a parabolic cure shape given by

$$z^* = S_d \ln\left(\frac{E_{max}}{E_d}\right) - \frac{2S_d}{W_0^2} y^{*2} \qquad \text{Eq. 2.8}$$

where (y*, z*) gives the locus of points where E=E_d. Figure 2.6 shows the cured profile for a Gaussian beam with a high energy dose (A) or a low energy dose (B). The line width (w) can be defined as the width of the cured region at the surface of the suspension (z*=0). The width of the region cured by a Gaussian beam is noted as w_{Gauss} and is simply 2y* (when z*=0), so

$$w_{Gauss} = W_0\sqrt{2} ln\left(\frac{E_{max}}{E_d}\right) \qquad \text{Eq. 2.9}$$

Based on Eq. 2.9, the surface line width for a Gaussian beam depends on energy dose; this complicates the analysis of the effect of composition on cured linewidth. A further difficulty arises because stereolithography lasers sometimes are multimodal and have complex, non-Gaussian intensity profiles. For non-Gaussian beams, one cannot easily separate the excess line width and cannot directly measure broadening. The spatial distribution of light from the laser results in a cure width that is dependent on the energy dose.

2.4.3 Build Styles

A stereolithography laser drawing across the surface of the suspension results in a thin cured line with a parabolic cross-section as described in the previous section. To cure the entire area of a single layer, the laser must raster across the surface to fill in the cured area. Figure 2.7 shows a schematic of the laser commands. First, the laser is

directed to draw the outer border of the shape it is creating, with the commands given by the "border vector". Then, the laser scans back and forth in the x-direction, followed by scanning in the y-direction, with commands given by the "hatch vector". Hatching produces an approximately uniform layer with the shape specified by the vector file (described in section 2.2). The specifics of these border and hatch parameters are given in the build styles that are used.

"Build styles" are files that are used to specify the beam scans, both within a single layer and between adjacent layers. The hatch spacing (h_s) is the distance between successive lines when filling in a single direction, as illustrated in Figure 2.8A. The hatch spacing should be defined with respect to the beam width. The ratio between the hatch spacing and beam radius must be less than or equal to 1 ($h_s/W_0 \leq 1$) for uniform curing, assuming a non-scattering resin.[5] Figure 2.8B shows a schematic of a hatch spacing that is two times larger than the beam width ($h_s/w_0 = 1$). This results in a cured surface that has a very uneven cure depth, due to the positional variation in the energy at the surface. A smaller hatch spacing of 0.4 times the beam width ($h_s/W_0 = 0.4$) is shown in Figure 2.8C. It is seen that this can be approximated as a uniform energy distribution. The build style is used to relate the desired cure properties to the laser positioning in the vector file.

Note that a variety of build styles are available for use. Some commonly used build styles leave portions of the interior partially polymerized, to reduce curing stresses that result from polymerization shrinkage. This also reduces the drawing time for the laser, speeding up the process. Examples of two build styles are given in Figure 2.9, with the grey parabolas indicating cross-sections of cured lines. The conventional hatch

(Figure 2.9A) draws parallel lines which are aligned with the layer below. In contrast, the staggered hatch build style (Figure 2.9B) draws lines such that they are offset from the lines in the layer below. Note that in both cases, the overcure is the additional cure depth of a given layer into the layer below, to provide adhesion between layers. Depending on the application and polymerization shrinkage, the styles and parameters within the styles (such as hatch spacing and overcure) can be varied. A further description of some of the methods to deal with shrinkage problems can be found in a 1992 patent by Hull *et al* from 3D Systems.[6] The modification of these build styles is through a combination of controlled experiments and trial and error.

2.5 Photopolymerization of Ceramic Suspensions

Understanding the behavior of the photopolymerization process is important for ceramic stereolithography and LAMP.[7] As detailed by the Tomeckova models,[8-10] the resin sensitivity, S_d, and the critical energy dose, E_d, are dependent on the volume fraction of ceramic particles in the suspension as well as the concentration of other ingredients within the suspension.

2.5.1 Tomeckova Predictive Cure Models

As discussed in section 2.4, the suspensions are assumed to be Beer-Lambert absorbers, so the energy dose attenuates exponentially with distance. The attenuation coefficient, α, is simply the reciprocal of the sensitivity $\left(\alpha = {}^{1}/_{S_d}\right)$. Furthermore, the absorption model predicts that the total attenuation coefficient of a ceramic suspension is

simply the sum of attenuation coefficients of each of the components to attenuation: scattering by ceramic particles, absorption by the ceramic particles, absorption by the photoinitiator, and absorption of the UV-absorbing dye.[9; 10] The resin sensitivity (S_d) is simply

$$\frac{1}{S_d} = \alpha_{Sc} + \alpha_{cer} + \alpha_P + \alpha_D \qquad \text{Eq. 2.10}$$

where α_{Sc} is the attenuation of due to scattering caused by the ceramic particles, α_{cer} is the attenuation due to absorbance of the ceramic particles, α_P is the attenuation due to the absorbance of the photoinitiator, and α_D is the attenuation due to the absorbance of the inert dye. Assuming the ceramic is UV transparent, the sensitivity can be predicted in terms of the concentrations of the components and their extinction coefficients, ε, by

$$\frac{1}{S_d} = \frac{1}{l_{Sc}} + (1 - \Phi)(c_P \varepsilon_P + c_D \varepsilon_D) \qquad \text{Eq. 2.11}$$

where l_{sc} is the scattering length of the suspension, Φ is the volume fraction of ceramic powder in the suspension, c_P is the concentration of the photoinitiator in the liquid solution, ε_P is the extinction coefficient of the photoinitiator, c_D is the concentration of the dye in the liquid solution, and ε_D is the extinction coefficient of the dye. Note that the extinction coefficient is wavelength dependent, and that non-laser sources can have a distribution of wavelengths. For these cases, the extinction coefficient must be convoluted with the intensity distribution. Provided that the scattering length, concentrations, and extinction coefficients of the components are known, the sensitivity can be predicted for ceramic suspensions.

It can be seen that there are two additive effects in Eq. 2.11: the scattering effects which are characterized by $1/l_{sc}$ and the absorption effects which are characterized by $(1-\Phi)(c_P\varepsilon_P + c_D\varepsilon_D)$. Generalized, the attenuation can be described as

$$\frac{1}{S_d} = S(\Phi) + A * (1-\Phi) \qquad \text{Eq. 2.12}$$

where S(Φ) is the scattering contribution function (which is dependent on the volume fraction) and A is the absorption term. Note that S(Φ)=$1/l_{sc}$. Wu *et al*. showed that $1/l_{sc}$ increases linearly for small volume fractions and then reaches a maximum for volume fractions near Φ=0.50.[11] The scattering contribution cannot be written in closed form, but can be approximated as a function of solids loading which can be written as

$$S(\Phi) = \beta\Phi - \left(\frac{\beta}{2\Phi_{max}}\right)\Phi^2 \qquad \text{Eq. 2.13}$$

where β is a fitting parameter that describes the rate of change of the scattering contribution with the volume fraction of powder and Φ_{max} is the volume fraction corresponding to the peak of the scattering contribution. The scattering contribution goes to zero as the solids loading approaches zero, as this corresponds to an infinite scattering distance. Generalizing the attenuation allows us to describe the attenuation into one of two primary regions: scattering dominated and absorption dominated. In scattering dominated suspensions, S is much larger than A (that is S(Φ)>>A), so attenuation is expected to decrease with volume fraction of powder. An example of this would be alumina suspensions with a low concentration of absorbing dyes. It is predicted that S_d will decrease with volume fraction powder, reaching a minimum around 50 vol% before increasing. The absorption-dominated region is given by A much larger than S (or A>>S(Φ)), and applies to cases such as silica suspensions with a high concentration of

absorbing dyes. In this case, S_d is expected to increase with volume fraction of powder, leveling out around 50 vol% before decreasing at very high solids loadings. The stereolithography suspensions for airfoils use silica, and are expected to be absorption dominated. The effects of composition on the photopolymerization of ceramic suspensions will be considered in more detail in Chapters 4-6.

Similar to the behavior of the resin sensitivity, the critical energy (E_d) can be predicted from the individual components in the suspension, using the inhibitor exhaustion model.[8; 10] Photons are either absorbed by inhibitors or dye or react with the photoinitiator to release free radicals. These radicals can either be annihilated by the inhibitors in the system or can contribute to free radical polymerization. Inhibitors included native oxygen in the suspension and inhibitors such as quinones which are added to make the monomer stable during storage. In order for polymerization to take place, all of the inhibitor must be consumed by free radicals so that there are excess radicals to propagate the reaction. The inhibitor is exhausted at the critical energy dose, E_d, which is dependent on the composition of the suspension as

$$E_d = (\gamma_{INH} c_{INH} + \gamma_D c_D) \frac{h\nu}{\Omega} \times \left[\frac{\frac{1}{l_{Sc}} + (1-\Phi)(c_P \varepsilon_P + c_D \varepsilon_D)}{c_P^2 \varepsilon_P^2} \right] \quad \text{Eq. 2.14}$$

where γ_{INH} is the number of radicals removed per inhibitor (such as oxygen or added quinone), c_{INH} is the concentration of the inhibitor, γ_D is the number of radicals that were not generated due to the presence of the dye, h is Plank's constant, ν is the frequency of

the light, and Ω is the number of free radicals given off per photon absorbed.[8; 10] Neglecting the higher order terms, this can be written as

$$E_d = (1 - \Phi)\frac{h\nu}{\Omega}(\gamma_{INH}c_{INH} + \gamma_D c_D)\frac{1}{c_P \varepsilon_P} \qquad \text{Eq. 2.15}$$

Below this energy, the inhibitors and dye absorb free radicals and no curing occurs. Above this energy, free radicals are available to propagate of the polymerization reaction and curing occurs. Note that this assumes the system is dose-equivalent and the critical energy dose does not depend on the intensity of the source, only the total energy. For non-dose equivalent systems, such as the slow curing glycol dimethacrylate monomer, the dose dependence must be accounted for. For the case of absorption-dominated, dose-equivalent silica suspensions, the inhibitor exhaustion model predicts that the critical energy decreases linearly as a function of solids loading as

$$E_d(\Phi) = K_6(1 - \Phi) \qquad \text{Eq. 2.16}$$

where K_6 is a combined constant which is given by

$$K_6 = \frac{h\nu}{\Omega}(\gamma_{INH}c_{INH} + \gamma_D c_D)\frac{1}{c_P \varepsilon_P} \qquad \text{Eq. 2.17}$$

Thus, the critical energy can be predicted for the solids loading, provided that the critical energy is measured for a few of the volume fractions.

2.5.2 Cure Shape of Ceramic Suspensions

For ceramic suspensions, the dimensions of the cured area will be much different than for commercial resins. The ceramic particles in the suspensions scatter the light, resulting in much broader cure widths than expected. Hinczewski *et al*. has proposed a model for the linewidth of ceramic suspensions, suggesting that line width in ceramic

suspensions can be predicted by modifying the equation for the linewidth of an ideal suspension using a Gaussian beam (Eq. 2.9). Their model is given by the following equation:[12]

$$w = F_1\sqrt{2}\sqrt{\ln\left(\frac{E_{max}}{E_{Hincz.}}\right)} \qquad \text{Eq. 2.18}$$

where F_1 is the equivalent beam width and E_{Hincz} is the apparent critical energy dose. Note that E_{Hincz} is different than the critical energy dose E_d. F_1 and E_{Hincz} are fitting parameters which depend on the Gaussian beam width and materials parameters (refractive index, solids loadings, etc). This model was shown to fit three ceramic suspensions containing alumina, zircon, or silica.[13] The major limitation of this model is that it is based on a Gaussian source. For higher mode lasers or for more uniform intensity distributions, this is no longer valid. Additionally, the observed cure widths can be many times larger than the beam width, such that the beam shape is less significant. For these reasons, a model is needed which is independent of the light source used for the measurements. The cure shape of ceramic suspensions will be discussed in more detail in Chapters 5 and 6.

2.6 Recoating/Levelling

After a single layer is drawn, the stereolithography machine must move the build down by the layer thickness, and lay a new layer of suspension on the surface. This can be done in several different ways. One way is to move the part down one layer, and then use a doctor blade to drag suspension over the surface of the part. This lays new liquid as well as levels the suspension above the part. For designs with large, flat cross-sectional

areas, the build can have a “deep dip”, in which the part is moved a centimeter or more below the surface of the suspension and then moved back up to the height for the next build layer. This deep dip allows resin to flow over the area, which is then leveled by the movement of the doctor blade. A third option is to use a “Zephyr” blade. This is a modified doctor blade, with an interior chamber, in place of the solid doctor blade. The chamber is kept under a slight vacuum, so that some suspension is held within the doctor blade. When the blade sweeps across the surface, it has a reservoir of additional suspension that can be laid on the surface as needed, regardless of the cured area below. For all three methods, variable recoating speeds can be used, depending on the suspension and part properties. The recoating speed is constrained by the machine limits as well as the suspension and part properties. Assuming that the fluid is Newtonian and that the blade to part geometry can be modeled simply as two parallel plates, the shear stress is related to the speed by

$$\tau = \eta \left(\frac{V}{z_{layer}} \right) \qquad \text{Eq. 2.19}$$

where τ is the shear stress, η is the viscosity of the suspension, V is the blade velocity, and z_{layer} is the layer thickness. Assuming a viscosity of 1 Pa-s, blade velocity of 10 cm/s, and layer thickness of 100 μm, the shear stress is 1000 Pa. Increasing the viscosity or decreasing the layer thickness leads to a proportional increase in the shear stress. Using a more viscous resin or suspension will potentially lead to destructive shear stresses (when τ is greater than the yield stress of the cured region). In those cases, the blade velocity would need to be decreased to account for the resulting shear. Finally, after recoating, a pause (z-wait) is generally added prior to drawing the next layer. This provides additional time for the surface of the suspension to level so that the next layer is

flat. These steps are typically used in stereolithography systems to ensure that a homogenous layer of suspension is laid on top of the previous layer. When this step is completed, drawing and recoating continues until the entire part has been built. For ceramic stereolithography, this part is termed a "green" part, as it contains the ceramic particles with a binder (in this case, the cured polymer).

2.7 Rinsing/Cleaning

When building is complete, the green part must be removed from the suspension and cleaned. This is an important process, as any uncleared suspension will cure during post-processing (firing). The exterior surfaces can be wiped down and hollow parts are drained to allow excess resin to flow off the part. To finish the clearing, some sort of rinse must be used. For rapid prototyping parts created with commercial resins, tripropylene glycol methyl ether (TPM) is typically used to remove the resin. The parts are agitated in a vat of TPM until adequately cleaned. Ceramic stereolithography airfoil molds have the complication that the important surfaces are on the interior of the mold, so extra care must be taken to ensure that these are cleared. Furthermore, the ceramic particles will not simply dissolve in a gentle solvent like TPM. Ceramic stereolithography requires a combination of adequate solvents and agitation to remove monomer and ceramic particles from the complex passages in airfoils.

2.8 Firing

After cured parts have been cleaned of the uncured suspension, they are fired to yield sintered ceramics. The first step during firing is a slow "binder burnout" to remove

the large amount of polymer without damaging the green body. After the binder is removed, a conventional sintering process can take place. The sintering conditions depend upon the material and particle size. For silica ceramic stereolithography suspension for use as airfoil molds, the firing schedule is as follows:

a. 5°C/min to 260°C
b. 3°C/min to 300°C
c. 0.5°C/min to 350°C, hold 2 hours
d. 0.5°C/min to 475°C
e. 3°C/min to 600°C
f. 20°C/min to 1350°C, hold 1 hour
g. 10°C/min to 25°C

Note that the firing schedule is performed in ambient atmosphere, with no control gases needed. The steps up to 600°C (a-e) are the binder burnout steps. It is during these temperatures that the organics are removed through pyrolysis. The rate and temperatures at which the binder is removed can be determined through thermogravimetric analysis (TGA), as shown in Figure 2.10. TGA measures the mass loss as a function of temperature, maintaining a constant heating rate, and shows that much of the ceramic stereolithography binder is lost between 250°C and 500°C. Temperature ranges with a high mass loss are given slower ramp rates and longer hold times, so that there is adequate time for the entire part to heat uniformly and for the gases to be given off. By 600°C, the organics have been removed.

The firing continues to higher temperatures to allow for the sintering of particles. Post-binder burnout, the parts are very delicate to be handled. Sintering is required to provide mechanical strength as the loosely held particles fuse together. The powders used for silica stereolithography are typically amorphous silica. The sintering time and temperature (step f above) are constrained by the transformation of silica from amorphous silica to crystalline β-cristobalite. The nucleation of β-cristobalite is a

stochastic process which occurs between 1100°C and 1470°C, with grains growing over time. A fired part with fully amorphous silica will have sufficient mechanical strength to be handled. However, holding it at high temperatures, such as those used for single crystal castings, will result in "sag" (the industry term for amorphous creep of a self-loaded beam). This will cause distortions of the part from the design. In contrast, a fully crystalline part (100% β-cristobalite) will have the mechanical strength to withstand mechanical loads at high temperature. However, there is a displacive phase transition between α- and β-cristobalite between 268°C and 272°C, with the exact temperature highly dependent on the sample history and test conditions.[14] This results in a 4.9% decrease in volume as the temperature is decreased,[15] which can cause cracking when the part is cooled after firing. For single crystal casting molds, it is important to have appropriate crystallization so that the molds survive single crystal casting without cracking or sagging. After firing, these ceramic molds can be used in the traditional investment casting process.

2.9 Conclusions

Ceramic stereolithography is a complicated manufacturing method of ceramic parts. A commercial machine is typically used, but the commercial resins are replaced with ceramic suspensions that have been developed. The steps of the process, going from a ceramic suspension to a fired part, are given in the sections of the chapter, with a summary in Figure 2.2. The remainder of this thesis will focus on modifying this process to improve the resolution of ceramic stereolithography for airfoil investment casting molds.

2.10 References

[1] I. M. Krieger and T. J. Dougherty, "A Mechanism for Non-Newtonian Flow in Suspensions of Rigid Spheres," *Transactions of the Society of Rheology,* **3** 137-52 (1959).

[2] C. Song, P. Wang, and H. A. Makse, "A phase diagram for jammed matter," *Nature,* **453**[7195] 629-32 (2008).

[3] T. M. G. Chu and J. W. Halloran, "High-temperature flow behavior of ceramic suspensions," *Journal of the American Ceramic Society,* **83**[9] 2189-95 (2000).

[4] E. Kannatey-Asibu, "Principles of laser materials processing,″ pp. xxvi, 819 p. Wiley: Hoboken, N.J., (2009).

[5] P. F. Jacobs and D. T. Reid, "Rapid prototyping & manufacturing: fundamentals of stereolithography.″ Society of Manufacturing Engineers: Dearborn, MI, (1992).

[6] C. W. Hull, S. T. Spence, C. W. Lewis, W. A. Vinson, R. S. Freed, and D. R. Smalley, "Method of and apparatus for production of three-dimensional objects by stereolithography with reduced curl," Patent 5104592 (1992).

[7] J. W. Halloran, V. Tomeckova, S. Gentry, S. Das, P. Cilino, D. Yuan, R. Guo, A. Rudraraju, P. Shao, and T. Wu, "Photopolymerization of powder suspensions for shaping ceramics," *Journal of the European Ceramic Society* (2010).

[8] V. Tomeckova and J. W. Halloran, "Critical energy for photopolymerization of ceramic suspensions in acrylate monomers," *Journal of the European Ceramic Society,* **30**[16] 3273-82 (2010).

[9] V. Tomeckova and J. W. Halloran, "Cure depth for photopolymerization of ceramic suspensions," *Journal of the European Ceramic Society,* **30**[15] 3023-33 (2010).

[10] V. Tomeckova and J. W. Halloran, "Predictive models for the photopolymerization of ceramic suspensions," *Journal of the European Ceramic Society,* **30**[14] 2833-40 (2010).

[11] K. C. Wu, K. F. Seefeldt, M. J. Solomon, and J. W. Halloran, "Prediction of ceramic stereolithography resin sensitivity from theory and measurement of diffusive photon transport," *Journal of Applied Physics,* **98**[2] (2005).

[12] C. Hinczewski, S. Corbel, and T. Chartier, "Ceramic suspensions suitable for stereolithography," *Journal of the European Ceramic Society,* **18**[6] 583-90 (1998).

[13] T. Chartier, C. Chaput, F. Doreau, and M. Loiseau, "Stereolithography of structural complex ceramic parts," *Journal of Materials Science,* **37**[15] 3141-47 (2002).

[14] R. B. Sosman, "The phases of silica,″ pp. x, 388 p. Rutgers University Press: New Brunswick, N.J., (1965).

[15] D. R. Peacor, "High-Temperature Single-Crystal Study of Cristobalite Inversion," *Zeitschrift Fur Kristallographie,* **138** 274-98 (1973).

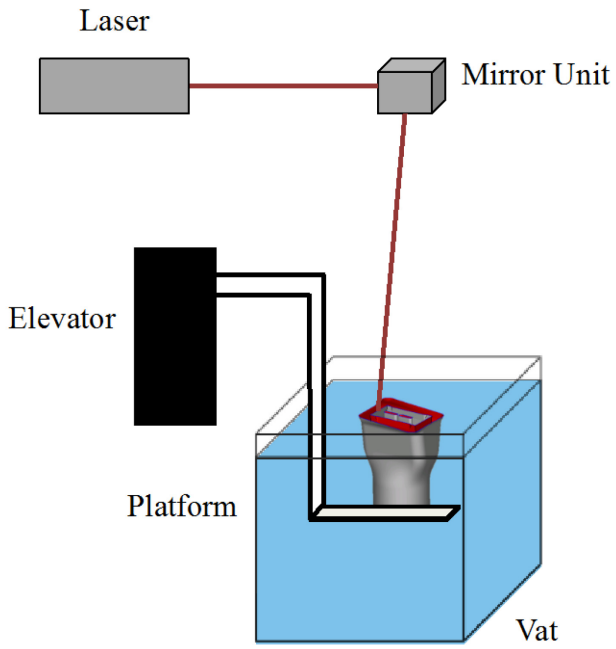

Figure 2.1 Schematic of a stereolithography machine such as the SLA-250 or Viper.

Table 2.1 Comparison of SLA-250 and Viper stereolithography machines.

	SLA-250	Viper
Wavelength of Laser	355 nm	355 nm
Beam Size	150 μm	50 μm
Minimum Layer Thickness	62.5 μm	25 μm
Laser Power	Fixed at 30 mW	Variable up to 100 mW
Software	Buildstation v4.0	Buildstation v5.5

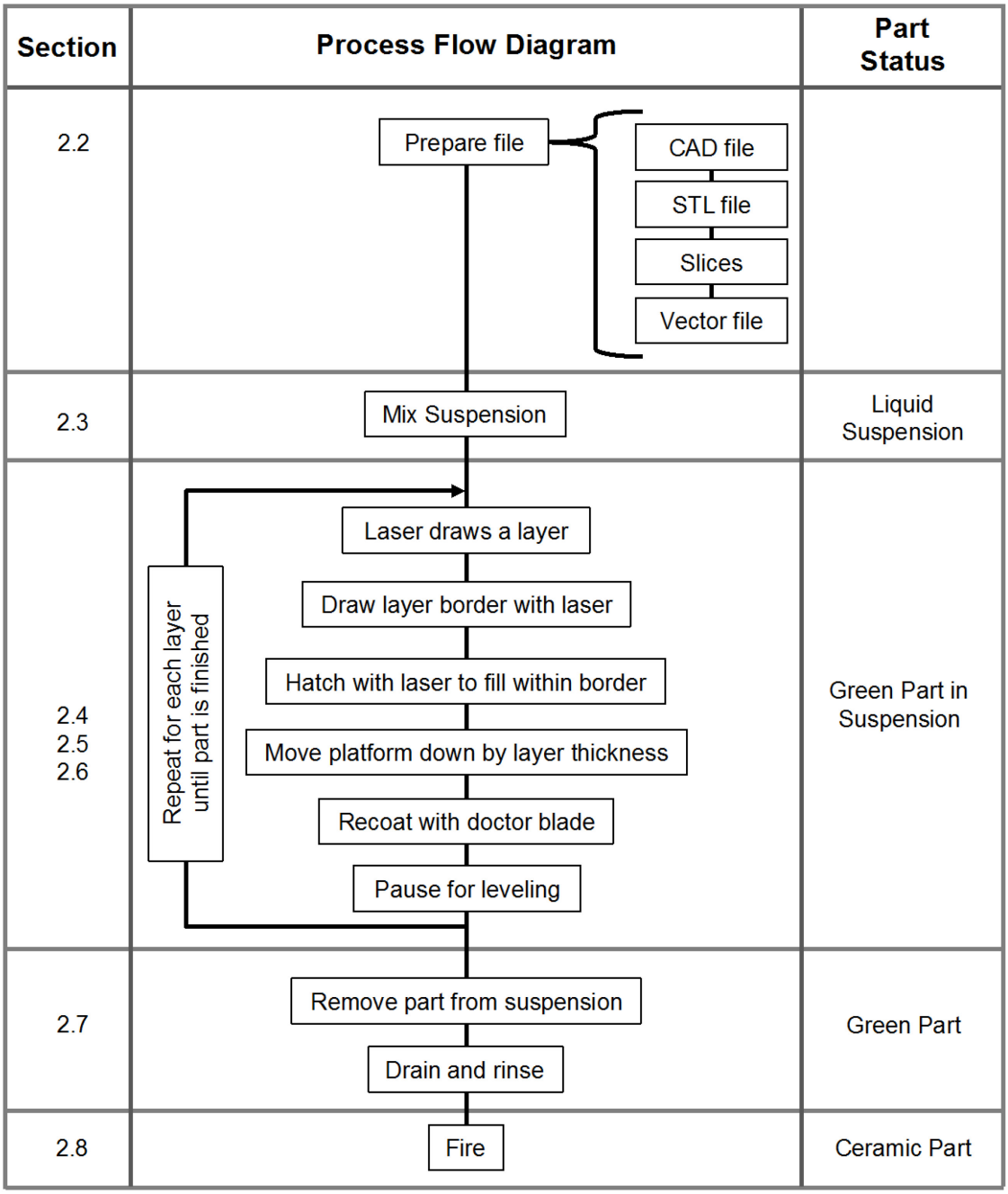

Figure 2.2 Process flow chart showing the steps needed for building ceramic parts with ceramic stereolithography. Included are the section number to refer to for more information and the status of the part.

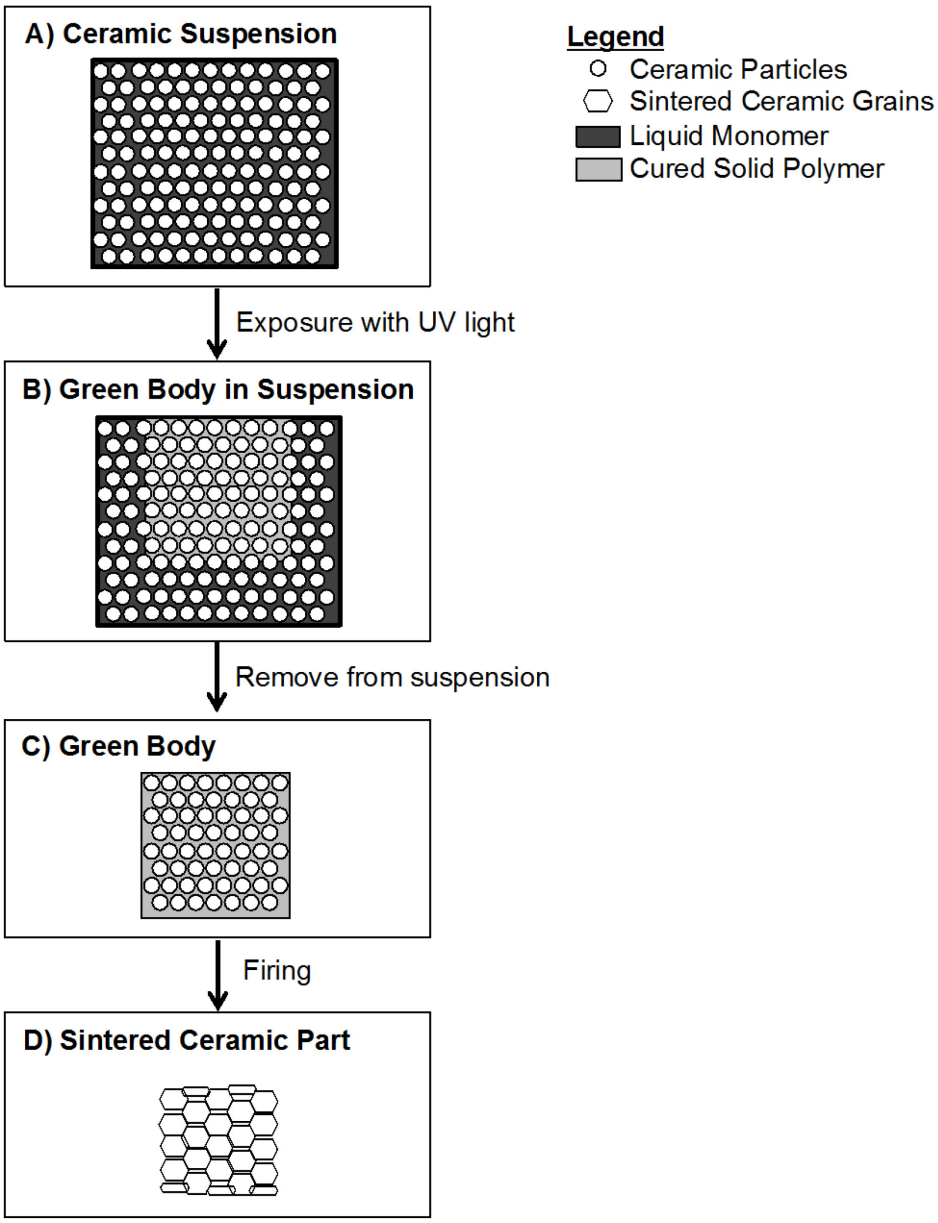

Figure 2.3 Diagram showing the steps from a ceramic suspension to a sintered part. Uncured ceramic suspension (A) is polymerized, resulting in a green body within the suspension (B). The green body is removed from the suspension and rinsed, to give the green body (C). This green body is then fired, resulting in a sintered ceramic part (D). A legend is given in the upper right corner, indicating the ceramic particles, sintered ceramic grains, monomer and polymer.

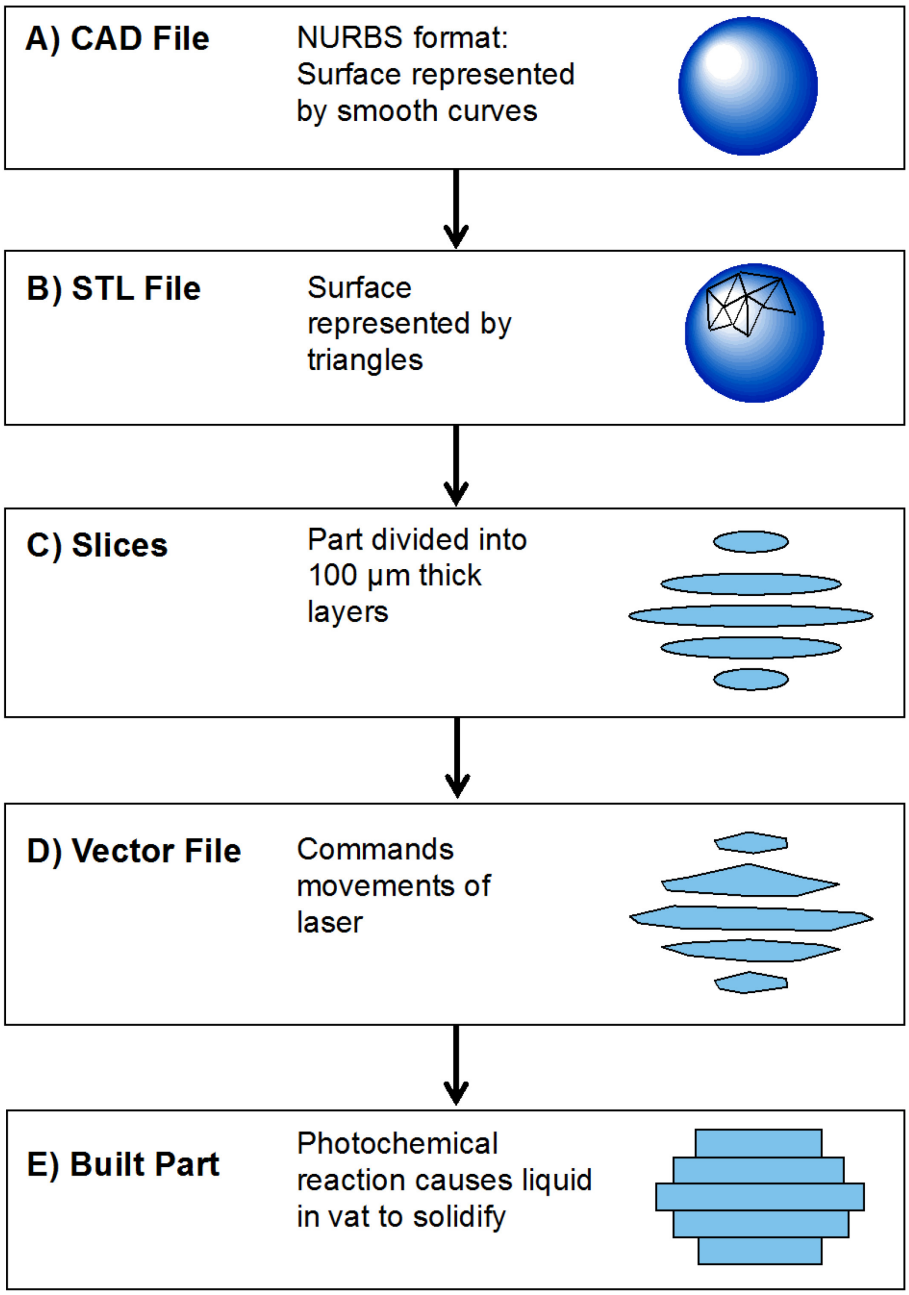

Figure 2.4 Schematic showing the steps converting a CAD file into a finished SLA build. A) First the part is designed as a CAD file, in NURBS format. B) The CAD file is converted to an STL file. C) The STL file is converted into slices. D) Slices are converted into a vector file which commands the laser movements. E) Finally the part is built using an SLA.

A) 1,6 Hexanediol Diacrylate

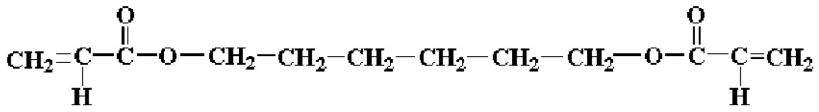

B) Ethoxylated Pentaerythritol Tetraacrylate

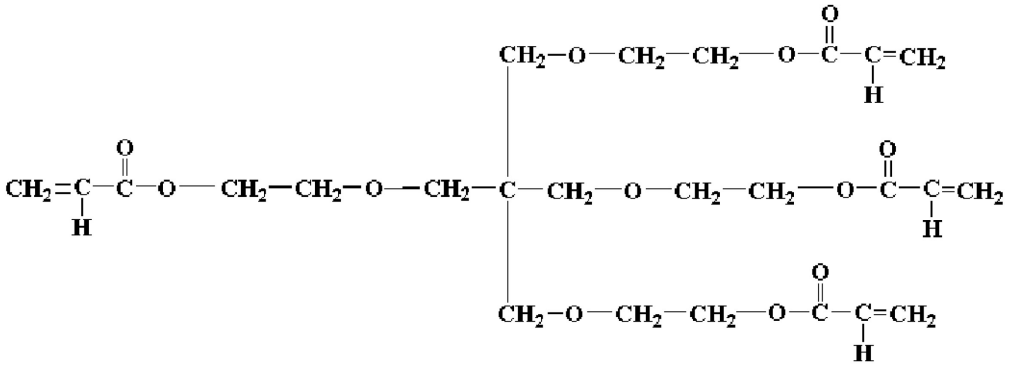

Figure 2.5 Chemical structures of 1,6 hexanediol diacrylate (A) and ethoxylated pentaerythritol tetraacrylate (B), as provided by Sartomer.

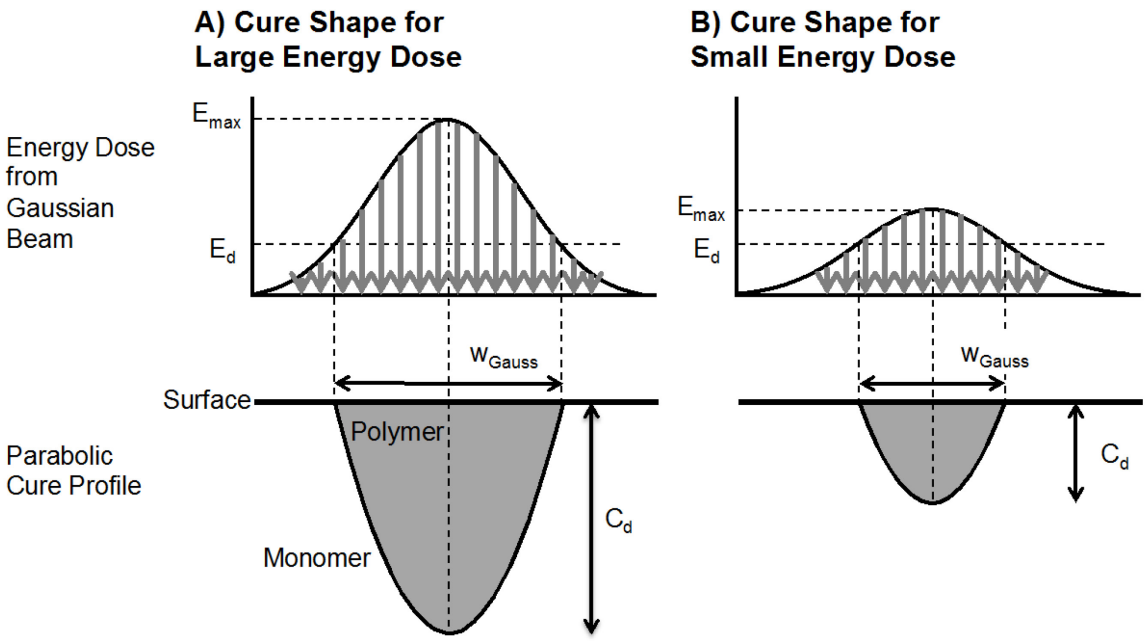

Figure 2.6 Comparison of predicted cure shapes for suspensions cured with a Gaussian beam with a large energy dose (A) and a small energy dose (B). Note that the width (w_{Gauss}) increases and the cure depth (C_d) increases with energy dose.

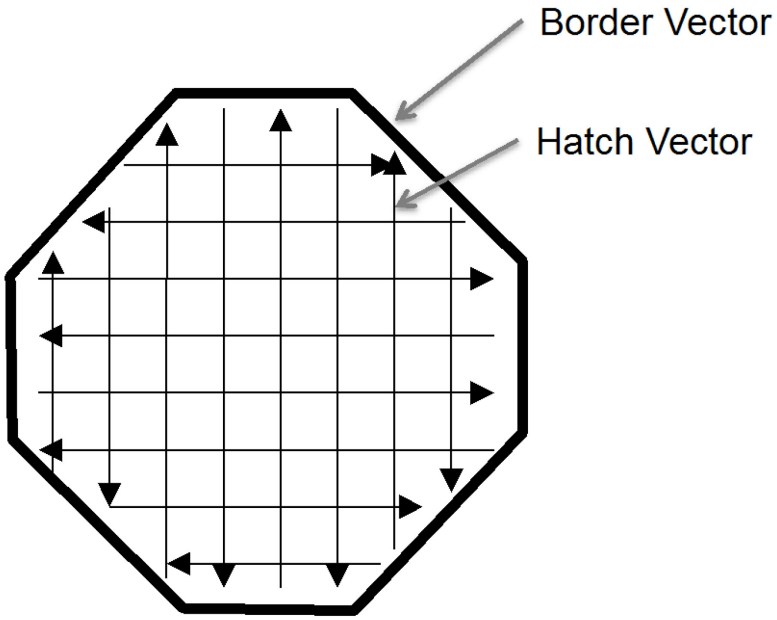

Figure 2.7 Schematic showing the rastering that is used to fill in a cured area. The edge is drawn with the border vector (thick line), and then the center is filled in with hatch vectors (thin lines).

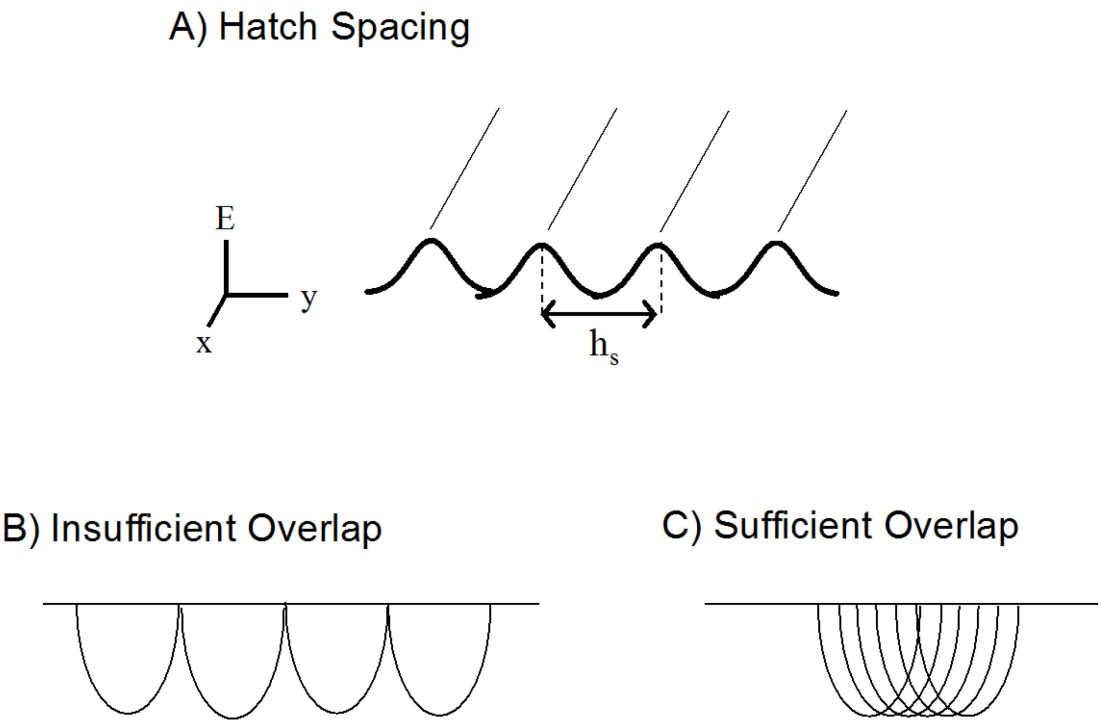

Figure 2.8 Schematic of hatch spacing (A) and examples of hatch spacing with insufficient beam overlap (B, $h_s=2*W_0$) and sufficient beam overlap (C, $h_s=0.4*W_0$)

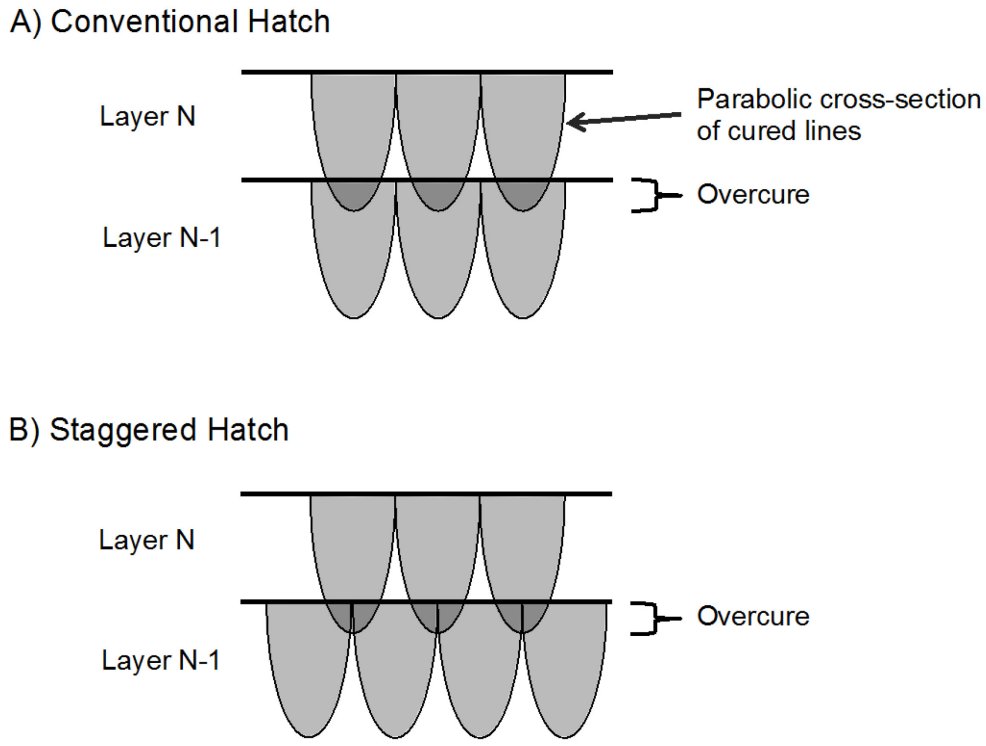

Figure 2.9 Schematic showing two different build styles. The gray parabolas indicate the cross-section of cured lines that were drawn by parallel hatch vectors. Two adjacent layers are shown: layer N and layer N-1. The overcure is the distance that the layer N is cured into the layer below it (layer N-1). A) Conventional hatch style with hatch vectors directly above the hatch vectors from the previous layer. B) Staggered hatch style with hatch vectors of layer N offset from the hatch vectors of layer N-1.

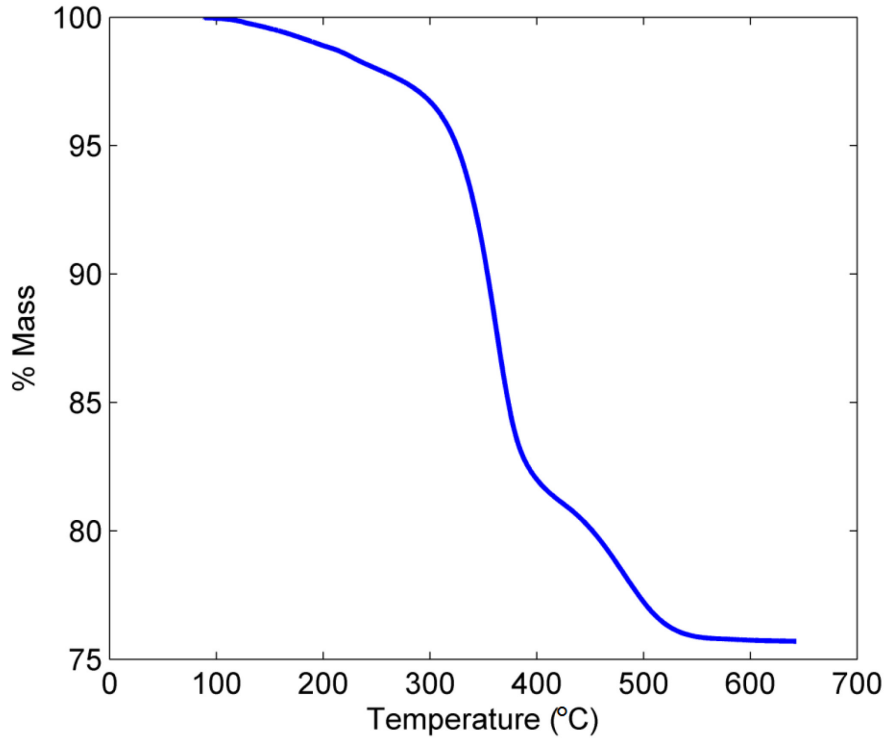

Figure 2.10 Mass loss as a function of temperature for the ceramic green bodies, as measured using thermogravimetric analysis (TGA).

Chapter 3

Limitations on Feature Resolution from Direct Digital Manufacturing Systems

3.1 Introduction

The most basic aspect of resolving fine features with ceramic stereolithography or other photopolymerization processes is the resolution that can be achieved with a given machine. It can be easy to overlook these issues as a ceramist and operate under the assumption that the resolution of the machine is perfect. However, like all systems, ceramic stereolithography is limited by the resolution of the stereolithography machine. It is important to understand these process limitations and how they affect ceramic stereolithography, before continuing to address issues with the suspension formulation. Understanding the process limitations is important to addressing the need to improve resolution in ceramic stereolithography.

Previously, it was assumed that the resolution of ceramic stereolithography was limited by the "building blocks" used. The basis for this is that it is not realistic to assume that a given additive manufacturing process will be able to resolve features that are smaller than the building blocks used to create them. These processes work by adding together features to build a larger, more complex part. For ceramic stereolithography, these "building blocks" include the size of the ceramic particles, laser beam diameter, and layer thickness.

Laser diameter is important to resolving the fine features. As discussed in section 2.4.2, laser beams often have a Gaussian intensity distribution that is characterized by their beam width (W_0) and their peak intensity (I_{max}). Commercial stereolithography machines have beam diameters of 50 to 250 μm. At a minimum, designs that are smaller than the diameter of the beam will either be unresolved or will be larger than designed. Furthermore, the resolution of shapes can be degraded by this larger beam diameter. Figure 3.1 contains an example demonstrating this limitation. A sample design is contained in Figure 3.1A, showing a 450 μm notch protruding from an arced surface. Three schematics are given to demonstrate the resolution of the border vector when drawn with a 75, 150 or 250 μm diameter beam (Figure 3.1B). It can be seen that the corners become much less crisp as the beam width increases, and instead are very rounded. The beam size for stereolithography is typically fixed, although newer machines have the capability of varying their beam width. In these cases, the laser resolution will still be constrained by the minimum beam width of the apparatus. Understanding the effect of the laser beam width is an important building block to understanding the process limitations of ceramic stereolithography.

The layer thickness is another significant building block in ceramic stereolithography resolution. Decreasing the layer thickness is a simple way to increase the resolution. Stereolithography is a layered process in which each layer is a constant thickness. For the SLA-250, the layer thickness is 62.5-250 μm, with layers stacked upon each other. This leads to a phenomena known as stairstepping. Angled surfaces are represented as a series of layers, yielding a surface with ledges. Figure 3.2 shows an example of a triangle as it would be represented in a layered manufacturing process. It

can be seen that the vertical and horizontal surfaces match the design, while the angled surface does not form a straight line. Figure 3.3 shows a segment of a ceramic mold that was built, with the arrow indicating stairstepping lines on a surface that is nearly horizontal. Depending on the use of the part, this accuracy may be acceptable or unacceptable. For a prototype, 200 μm layers might be sufficient to visualize a part, while 50 μm layers might be needed to achieve the required accuracy for a different application. Note that features that are of the thickness of the layer or smaller might not be resolved depending on the slicing algorithm used. For example, a 100 μm horizontal feature might not be drawn if the layer thickness is 250 μm. Methods have been proposed to remove downward-facing stairsteps by varying the energy dose within a layer.[1] Traditionally, stereolithography has used a fixed cure depth, although varying the energy dose can result in a continuous variation in cure depths. This would allow for downward-facing surfaces to be smoothed. However, removing up-facing stairsteps continues to be a difficulty for traditional photopolymerization processes like SLA, as the polymerization begins at the surface of the suspension. It is impossible to remove up-facing stairsteps in traditional stereolithography.

Note that two-photon polymerization microstereolithography uses two laser beams to cure regions below the surface of the suspension.[2] The photoinitiator is chosen such that it requires the additive energy of the two beams to release free radicals, so polymerization only occurs at the intersection of the two beams. However, this is not practical for large builds such as investment casting molds as the cure time would become excessively large. Furthermore, two-photon polymerization requires a medium that is non-scattering, so that the light can propagate directly through the suspension

without any deviations from the beam. Scattering mediums such as the ceramic suspensions for ceramic stereolithography will result in a diffuse energy dose and hinder the fine curing of two-photon polymerization. Two-photon polymerization is not a practical method to improving the resolution of ceramic stereolithography for airfoil casting molds.

Although it might seem ideal to use the minimum layer thickness, the desires for accurate builds must be balanced by the time required to build them. For example, assume a simple cube is to be built, with sides of 1000 μm. This can be done by building four layers that are 1000 μm x 1000 μm x 250 μm. Alternatively, ten layers of 1000 μm x 1000 μm x 100 μm can be built. Since all surfaces are horizontal or vertical, stairstepping is not a consideration. However, the two scenarios will have different overall build times. The total build time (τ_{tot}) can be subdivided into two segments: a recoating time and a drawing time, as given by

$$\tau_{tot} = \tau_{r,tot} + \tau_{c,tot} \qquad \text{Eq. 3.1}$$

where $\tau_{r,tot}$ is the total recoating time and $\tau_{c,tot}$ is the total curing time. The number of layers is simply equal to the total height of part (z_{tot}) divided by the layer thickness (z_{layer}), rounded up to the nearest integer. The recoating time is fixed for each layer, regardless of layer thickness, depending on the speed of the recoating mechanism and any dwell time included. These will be lumped into τ_r, the time to recoat a single layer. A typical recoat time for stereolithography is 10-100 seconds. The total recoat time is given by

$$\tau_{r,tot} = \frac{z_{tot}}{z_{layer}} \tau_r \qquad \text{Eq. 3.2}$$

and is inversely proportional to the layer thickness. Decreasing the layer thickness will increase the total recoating time. The time for curing each layer will depend on the amount of time required to sufficiently illuminate the surface so that the cure depth reaches the specified value. For stereolithography, the writing time for a single layer (τ_c) is given by

$$\tau_c = \frac{A_{ave}}{P_L} E_d \exp\left(\frac{z_{layer}}{S_d}\right) \qquad \text{Eq. 3.3}$$

where A_{ave} is the average cured area of a layer, P_L is the laser power, E_d is the critical energy dose of the suspension, z_{layer} is the layer thickness, and S_d is the resin sensitivity.[3] A typical stereolithography build can take several seconds to several minutes to cure a single layer. The time to cure all layers is given by

$$\tau_{c,tot} = \frac{z_{tot}}{z_{layer}} \tau_c = \frac{z_{tot}}{z_{layer}} \frac{A_{ave}}{P_L} E_d \exp\left(\frac{z_{layer}}{S_d}\right) \qquad \text{Eq. 3.4}$$

This predicts that the total cure time will be maximized for large and small layer thicknesses, with a minimum at intermediate layer thicknesses. The total build time (τ_{tot}) is

$$\tau_{tot} = \tau_{c,tot} + \tau_{r,tot} = \frac{z_{tot}}{z_{layer}} \tau_r + \frac{z_{tot}}{z_{layer}} \frac{A_{ave}}{P_L} E_d \exp\left(\frac{z_{layer}}{S_d}\right) \qquad \text{Eq. 3.5}$$

This shows that the total build time has a complex dependence on the layer thickness. The thinner layers will require less overall time to polymerize than the thicker layers, due to the semilogarithmic relationship between cure depth and energy dose. Doubling the energy dose (and the time for illuminating a layer) does not fully double the cure depth. Instead, some of the additional energy is absorbed and does not contribute to polymerization. The part with thinner layers will cure faster. However, more layers requires more curing steps. Additionally, the recoat time is fixed for each layer, so

increasing the number of layers will result in a longer recoating time. Thus, the desires to minimize stairstepping by using thin layers will be needed to be weighed against the increase in build time for the process. Assuming that a stereolithography build requires 1500 layers (each 100 μm thick, corresponding to a total height of 15 cm), with a recoat time of 15 seconds per layer and a cure time of 1 minute for each layer, the total build time would be 31.25 hours. For industrial processes where time is valuable, additional build time must be allocated to use the thinnest layers possible.

The particle size and particle size distribution are very important to the resolution of ceramic stereolithography. Sufficiently small particles must be used to resolve all of the features. If a part needs resolution within 100 μm, then 125 μm particles cannot be used. This is significant, as typical investment casting molds use several different powders for their cores and molds. A fine zircon powder is used for the core and for the first interior coating of the shell. The wax pattern is then successively dipped into silica slurries containing larger and larger particles. This results in a variation in particle size distribution as the distance increases from the interior surface. The large particles are used to reduce the sintering shrinkage. However, ceramic stereolithography cannot use these large particles to reduce the sintering shrinkage as they would decrease the surface finish and resolution of the part. Small particles must be used to achieve adequate resolution for ceramic investment casting molds.

It has been shown that the "building blocks" are important to the resolution of ceramic stereolithography. However, this chapter will show that there are hardware and software limitations to the stereolithography resolution. These include the design of the mold, the slicing of the molds, and the photocuring parameters of the suspension.

3.2 Design: Overhangs/Unsupported Regions

The design of the mold was found to be significant to the resolution of the process. Stereolithography is a layered process, requiring that all sections of the design be sufficiently supported from below. There are several ways for layers to be supported. Most obviously, layers can be supported by being built directly over the previous layer, resulting in the new layer adhering to the layer below it. Another common method is through the use of support structures, which are removable scaffolds that are built up to support a region of the design. These can be manually removed after building, provided that they are on the *exterior* of the design. However, if the supports cannot be accessed, then there is no method for removing them. The application of ceramic investment casting molds requires complicated *interior* geometries. As explained in section 1.2, the hollow spaces of the mold correspond to the metal of the airfoil. This confined interior is the most important aspect of the mold, with no method of removing the supports. Instead, the mold will have to incorporate the limitations of a layered building process.

Certain design features are more difficult to support than others. Large overhangs are problematic, because the cured region may not have sufficient mechanical strength to withstand drag from the recoating blade. Additionally, internal designs where features are supported from above are impossible to build. An unsupported island is a feature that is free-floating during building (Figure 3.4), even if the feature connects to the rest of the design in a later layer. Recoating will cause the island to move or be destroyed. As discussed in section 2.6, the shear stresses experienced are on the order of 1000 Pa, assuming a viscosity of 1 Pa-s, blade velocity of 10 cm/s, and layer thickness of 100 μm.

Finer features with thinner layers will experience larger shear stresses, as the shear stress is inversely proportional to the layer thickness. Although these are only approximate shear stresses, experiments using similar build conditions have shown that features can be damaged by the recoating process. Evidence of an unsupported island is seen in Figure 3.5, which shows a mold that was built in the vertical orientation. The serpentine passage of the core is unsupported at the bottom (note that this region is the same region indicated in Figure 3.4). Figure 3.5A shows the bottom of the serpentine passage in the computer aided drawing (CAD) file while Figure 3.5B shows the corresponding built part. It can be observed that the bottom of the serpentine passage is missing in the built part. Some failures in the built parts can be attributed to unsupported islands in the design. For internal features, such as the island in Figure 3.4, it is not possible to use supports as there is no way for these to be removed when the build is completed. It is important to look for large overhangs and unsupported islands in designs prior to building them.

One way to address unsupported islands and large overhangs is to adjust the orientation of the part on the build platform. By building molds at an angle, it is possible to remove some unsupported islands. For example, building the cored molds at an angle 45° from vertical removed the island shown in Figure 3.4 and Figure 3.5, as that section was now connected to built regions. However, it is possible that other complicated designs will not have a successful build orientation in which there are no unsupported islands. Airfoil molds have very complex geometries that are optimized for their aerodynamic properties, as described in section 1.2. The design limitation of unsupported regions in ceramic stereolithography must be accounted for when designing the part. Potential airfoil/mold designs must be selected without unsupported regions to

ensure part accuracy. Optimal part design will require collaboration between the aerospace engineers developing the design and the manufacturing engineers building the part so that desired features can be produced.

3.3 Software: Slicing Algorithm

Converting a design from its initial CAD design into machine commands is another aspect of the build process that is significant to the resolution. As detailed in section 2.2, there are a number of steps to prepare the design for building. Each step creates an approximate representation of the design, based on the design from the previous step. This results in errors compounding through the process. The initial CAD file with smooth surfaces is converted into a tessellated STL file. This is then sliced into the layers, and each layer is assigned rastering commands for the laser. The slicing and vectoring algorithm was found to decrease the resolution for certain designs.

One notable example of the slicing algorithm limiting resolution is that of resolving narrow rods on the core segment of the mold. Figure 3.6 shows a segment of a mold core that was built using ceramic stereolithography. This segment is supposed to have narrow rods 450 μm in diameter, but these did not form. Analyzing the commands used to position the laser provided information as to why these small rods did not form during the SLA build. The path of the laser is assigned using the 3D Lightyear 1.5.2 software to slice CAD files and convert the information into commands for the positioning of the laser. These are saved as a vector file, which contains the information regarding the positioning of the laser for each layer. In this file, it can be seen that there are errors in the specified laser path. For example, Figure 3.7 shows a schematic of a

mold that has been sliced at the 415th layer of a mold that will be constructed of about 1500 layers (assuming 100 μm layers). The CAD file is shown in Figure 3.7A, while the corresponding border vector for layer 415 is given in Figure 3.7B. The laser takes the path given by the black line, and then hatches in the x- and y- directions to fill in the cured (shaded) regions. The border vector provides the outer limits of the cured region. Note that the hatch vectors are not shown for clarity. These instructions are saved into the vector file that is one of the files used by the stereolithography apparatus to define a build. An airfoil mold would have about 1500 of these 100 μm layers stacked on top of one another, forming the three-dimensional part. For the application of airfoil casting molds, the polymerized area is the inverse of the airfoil design. The "ceramic mold" is the area that will be the silica mold, and is the area where the laser cured the photosuspension. The "gap for molten metal" is the empty space where the laser did not cure the photosuspension, and will be empty after the build once the uncured liquid is drained out. This gap in the mold will fill with metal during the casting process, resulting in the metal airfoil. Errors in the vector file will correspond to errors in the final metal casting.

Analyzing the slices and beam commands can show why certain features are not resolved in a built part or cast part. Continuing the example from above (Figure 3.6 and Figure 3.7), Figure 3.8 shows the CAD file for a portion of the core and some of the corresponding vector files. Note the two posts indicated in Figure 3.8A. Their locations are indicated in the vector files for layers 415-418 in Figure 3.8B-E. As a reminder, the black lines indicate the border vector drawn by the stereolithography machine, the shaded regions indicate the ceramic mold (corresponding to air gap or surfaces of the metal after

casting), and the white regions indicate the gap in the ceramic mold (corresponding to metal after casting). In layer 415 (Figure 3.8B), it can be seen that the posts have begun to be drawn by the border vector, and are protruding from the semi-circular section of the ceramic mold. As the build continues, a fresh layer of suspension is deposited by the recoating system and layer 416 (Figure 3.8C) is drawn directly above layer 415. It can be seen that post 1 was not drawn at all in layer 416, while post 2 continues to grow from the surface of the semicircle. The build continues with layer 417 (Figure 3.8D) where post 1 reappears and is drawn, while the border vector of post 2 is angular and inverted instead of oval. In layer 418 (Figure 3.8E), post 1 is again not drawn by the laser. In this layer, post 2 continues to be drawn apart from the semicircle, as expected. Additional layers would be built above layer 418, until the entire build is finished. A three-dimensional build is simply the stacking of these layers on top of one another.

Overlaying the border vectors for adjacent layers allows for the visualization of how segments will form, similar to a topographical map. The slices from Figure 3.8B-E are compiled and overlaid in Figure 3.9A. The black lines indicate the border vectors, which define the laser path for the edges of the cured region. It can be seen that the segments for post 1 barely form. This is significant, because if the laser is not given the proper commands, it cannot be expected that the posts will form. The overlay for post 2 is better, although it shows that the layers are non-contiguous; that is, some of the layers do not overlap with the layers below them. These segments will be floating, unsupported islands that will be damaged during recoating (similar to the features discussed in section 3.2). The missing posts illustrated in Figure 3.6 can be attributed to the corresponding vector file that did not have adequate resolution to draw them (shown in Figure 3.9A).

It was noted that updating the software used to run the stereolithography machine provides much more adequate slices for the same geometry. The slices shown in Figure 3.8 and Figure 3.9A are created for the 3D systems' Buildstation v4.0 software, which is used to run an SLA-250 such as the one at the University of Michigan. Newer machines, such as 3D Systems' Viper SLA unit, use an updated version of the software (Buildstation v5.5). This uses an updated slicing algorithm that is better at resolving certain fine features. Figure 3.9B shows the overlays for the same slices generated for Buildstation v5.5. It can be seen that the posts are much better formed, with overlapping ovals. These have the correct shape (ovals) and are contiguous with the layer below (preventing unsupported islands), unlike the slices in Figure 3.9A. Note that no change has been made to the design, rather the slicing algorithm was changed. This might seem like a simple discovery, that the most-up-to-date software available should be used. However, it is important to understand all of the limitations of a process, as it can often be costly to continually upgrade software. Commercial machines, such as the SLA-250 manufactured by 3D Systems, have the advantage that the software has already been developed, allowing users to focus on other aspects of their work, such as producing high-quality casting molds. However, they have the disadvantage that when issues arise in the software or hardware, it can be complicated to solve these problems, since the source code is not readily provided. It is important to understand these competing drives, between the convenience of a commercial machine, which requires costly upgrades, and the personalization available with newly developed processes such as LAMP. There have been groups that have created their own build styles for stereolithography,[4] but the complexities of doing this must be weighed against the advantages. This discovery of the

software limiting the resolution is important to producing fine features in ceramic investment casting molds.

3.4 Hardware: Beam Intensity Fluctuations

Fluctuations in the laser intensity can also limit the resolution of stereolithography. The behavior of suspensions under illumination is well-defined for simple systems without power fluctuations. Photons cause the photoinitiator to release free radicals which cause polymerization of the crosslinking monomers. The resin photocuring is characterized by two parameters: the resin sensitivity to light, S_d, and the critical energy dose required for curing, E_d. As described in Chapter 2, the cure depth is related to the energy by[5]

$$C_d = S_d \ln\left(\frac{E_0}{E_d}\right) \qquad \text{Eq. 3.6}$$

where C_d is cure depth and E_0 is energy dose at the surface. The power in Watts is related to the energy dose in J/m^2 by

$$E_0 = \frac{P_L}{V_L h_s} \qquad \text{Eq. 3.7}$$

where P_L is the laser power, V_L is the velocity of the laser on the surface of the suspension, and h_s is the center to center distance between adjacent lines of the laser. Thus, the cure depth can be related to laser power by

$$C_d = S_d \ln\left(\frac{1}{E_d}\frac{P_L}{V_L h_s}\right) \qquad \text{Eq. 3.8}$$

These equations are derived assuming a constant intensity energy source.

In reality, the laser power is not constant and this results in fluctuations in the cure depth. The laser power was measured at different times, and it was found that the laser power fluctuations, *f*, are about 3-5% for our system (Figure 3.10). To find the effect of the laser power fluctuations on the cure depth, take the derivative of the cure depth with respect to the laser power. This gives

$$dC_d = S_d \frac{1}{P_L} dP_L \qquad \text{Eq. 3.9}$$

Note that the fluctuations, *f*, can also be expressed as

$$f = \frac{1}{P_L} dP_L \qquad \text{Eq. 3.10}$$

Therefore, the change in cure depth due to the laser power fluctuations is simply given as

$$dC_d = S_d f \qquad \text{Eq. 3.11}$$

Alternatively, the cure depth can be expressed as a function of the power fluctuations

$$C_d(f) = S_d \ln\left(\frac{1}{E_d}\frac{P_L}{V_L h_s}\right) + S_d \ln(1+f) = C_{d,0} + S_d \ln(1+f) \qquad \text{Eq. 3.12}$$

where $C_{d,0}$ is the cure depth in the absence of fluctuations. This predicts the variation in cure depth that is expected for a suspension with known sensitivity and a system with known power fluctuations.

The resin sensitivity becomes very important when power fluctuations are incorporated into the cure depth analysis. From Eq. 3.12, the sensitivity, S_d, dictates how much the cure depth varies from the nominal cure depth $C_{d,0}$. Note that the cure depth in the absence of fluctuations (f=0) remains unchanged. Additionally, the critical energy dose (E_d) does not factor into the fluctuations in the cure depth; the critical energy dose only affects the nominal cure depth. For suspensions with variable intensity, the fluctuations will result in changes in cure depth that are dependent on the sensitivity of

the suspension. Using a suspension with a large sensitivity will result in large changes in cure depth and a decrease in vertical resolution. For example, assume that the nominal cure depth is 100 μm in a system that has cure fluctuations given by Figure 3.10. The predicted cure depths for this system are shown in Figure 3.11 for suspension sensitivities of 100 and 1000 μm. It can be seen that the fluctuations for the suspension with a sensitivity of 100 μm are small, with cure depths varying between 97 and 102 μm. In contrast, much larger cure depth fluctuations are expected for a suspension with a sensitivity of 1000 μm. For this suspension, the cure depths vary between 71 μm and 120 μm. It is important to limit the sensitivity when developing suspensions, so that minor fluctuations in intensity do not significantly affect the cure depth.

A maximum sensitivity can be calculated, assuming a given allowable variation in cure depth (ΔC_d) and given power fluctuations:

$$S_d \leq \frac{\Delta C_d}{f} \qquad \text{Eq. 3.13}$$

Assuming that a ±5 μm fluctuation in cure depth is acceptable and the beam has 3% laser fluctuations, S_d must be no larger than 170 μm for satisfactory curing. Understanding these fluctuations provides guidance for designing a suspension with appropriate resin sensitivity.

3.5 Conclusions

Understanding the process limitations allows for users to improve the resolution of ceramic stereolithography. It has been shown that the CAD mold must be designed around the constraints of ceramic stereolithography, so that there are no unsupported regions. Furthermore, the slices of the files should be analyzed when features are missing

or flawed. It is possible that these issues are due to the slicing algorithm, rather than limitations of the suspension. Finally, the suspension must be designed in accordance with the limitations of the machine. There are natural fluctuations in the laser power which will in turn result in variations in the cure depth. The allowable sensitivity will have a range with the maximum given by the ratio of the acceptable cure depth difference divided by the laser power fluctuations. For a ceramic suspension used with a light source that has 3% power fluctuations and ±5 μm variation in the acceptable cure depth, the sensitivity of the resin must be limited to below 170 μm. These are the process conditions that are important to understand in order to improve the fine feature resolution in ceramic stereolithography. However, there are additionally issues with the ceramic suspensions that must be addressed, and these will be dealt with in the following chapters.

3.6 References

[1] B. Sager and D. W. Rosen, "Use of parameter estimation for stereolithography surface finish improvement," *Rapid Prototyping Journal,* **14**[4] 213-20 (2008).

[2] S. Kawata, H.-B. Sun, T. Tanaka, and K. Takada, "Finer features for functional microdevices," *Nature,* **412**[6848] 697-98 (2001).

[3] C.-J. Bae, "Integrally Cored Ceramic Investment Casting Mold Fabricated by Ceramic Stereolithography," Ph.D. Dissertation, University of Michigan, (2008).

[4] S. Rahmati, Y. Norouzi, and Y. Hojjat, "A novel lattice structure for SL investment casting patterns," *Rapid Prototyping Journal,* **15**[4] 255-63 (2009).

[5] P. F. Jacobs and D. T. Reid, "Rapid prototyping & manufacturing: fundamentals of stereolithography.″ Society of Manufacturing Engineers: Dearborn, MI, (1992).

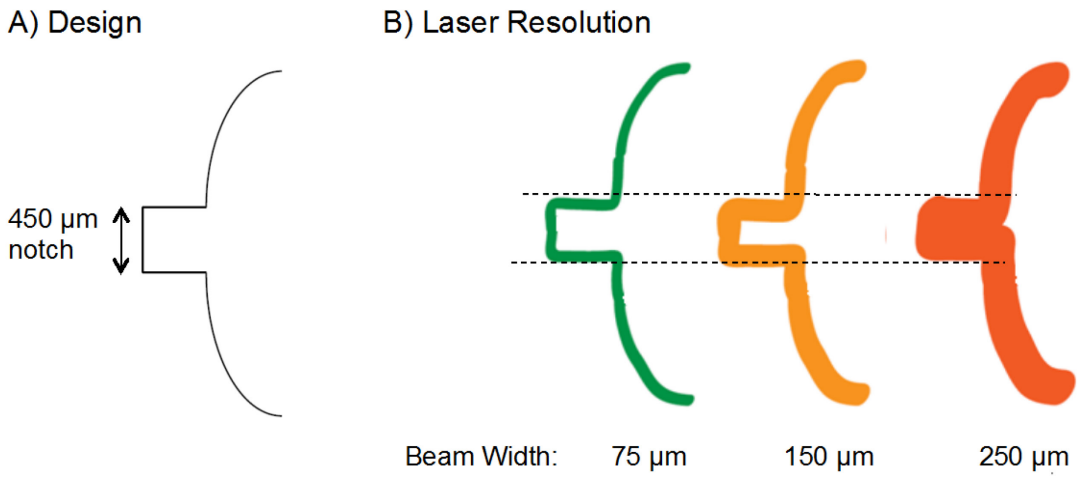

Figure 3.1 Effect of beam size on the resolution capabilities of stereolithography.

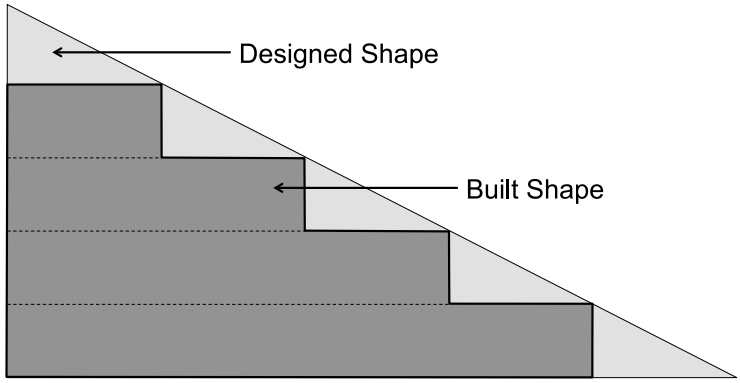

Figure 3.2 Schematic showing stairstepping on a triangular part. The built region (darker gray) is overlaid on the designed shape (lighter gray), showing the deviations in the built shape from the designed shape.

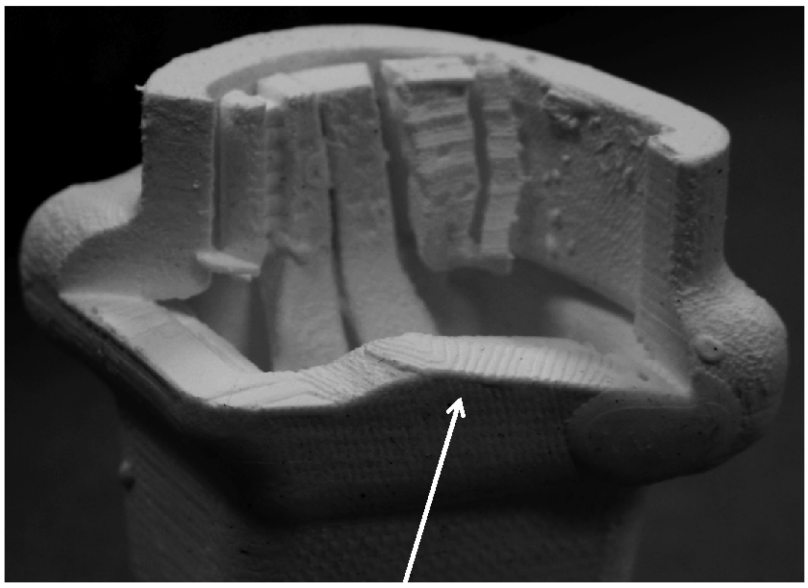

Figure 3.3 Segment of a mold illustrating stairstepping on a low-angle surface. Note that the mold was built by Chang-Jun Bae.

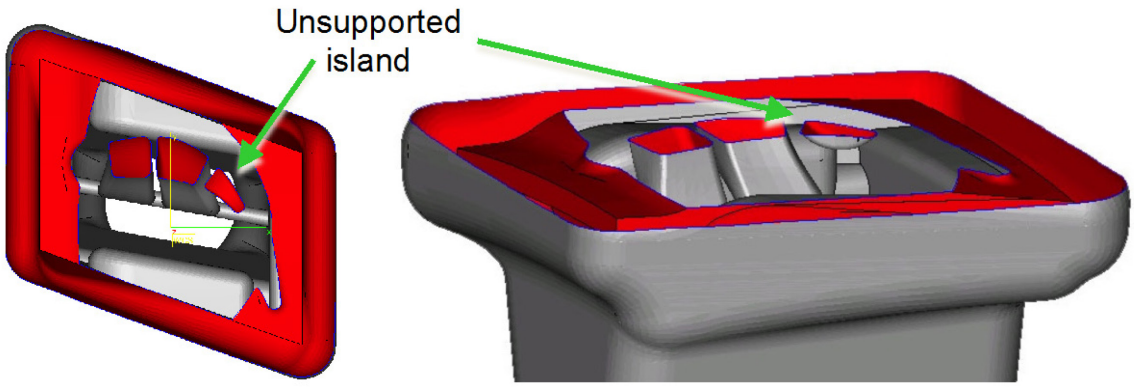

Figure 3.4 An unsupported island in a stereolithography design. The red layer indicates the current layer being drawn, and the gray section of the design indicates the part that has already been built. From the two views, it can be seen that the segment is not connected to the rest of the design from the side or below.

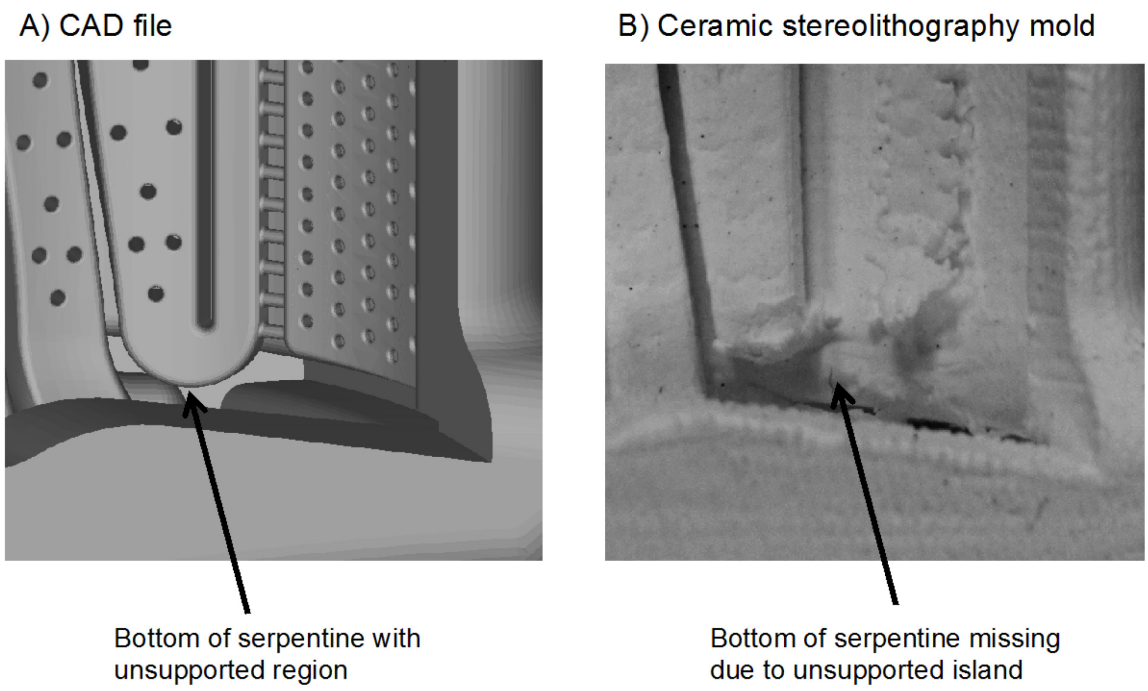

Figure 3.5 Example of an unsupported island in a mold. A) CAD file showing the bottom of the serpentine passage to be built. B) Ceramic mold missing the bottom portion of the serpentine. Note that the mold was built by Chang-Jun Bae.

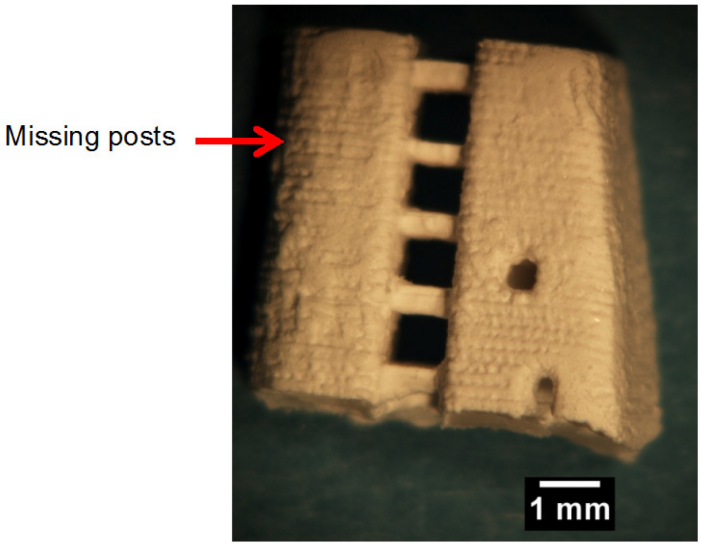

Figure 3.6 Segment of mold that is missing posts which are designed to be 450 µm in diameter.

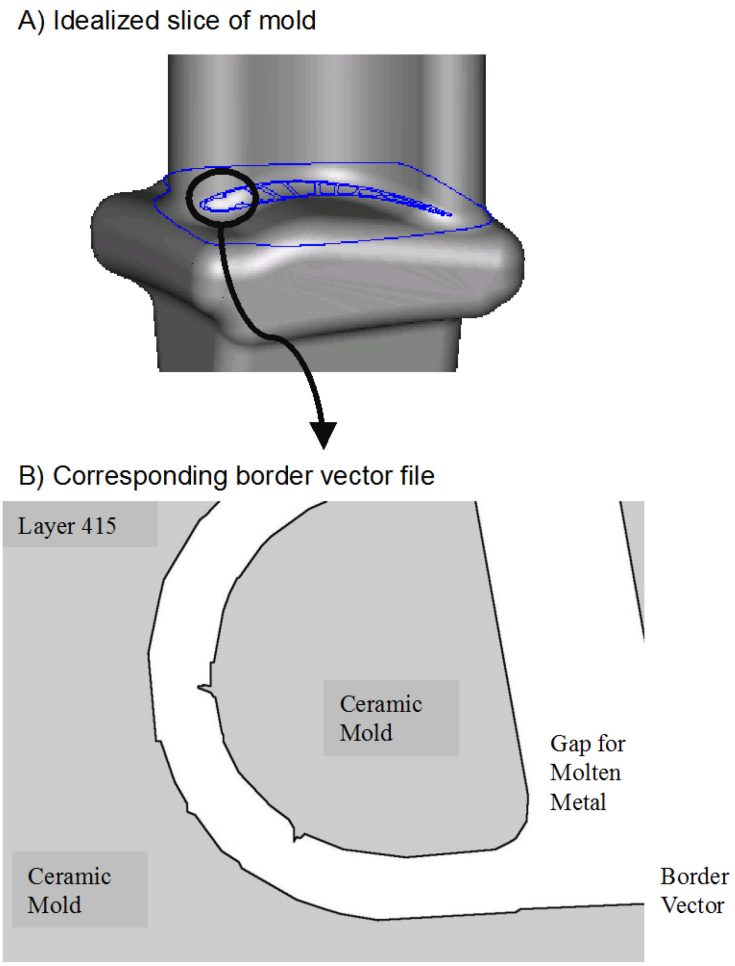

Figure 3.7 Schematic showing a slice of a cored mold at layer 415 (assuming 100 μm layers). A) Illustration showing the location of the slice and approximate geometry. B) Corresponding vector file showing the border vectors (black line) to be drawn around the outside of the cured regions. The cured region of the ceramic mold is shaded for clarity, while the gap for the molten metal is white.

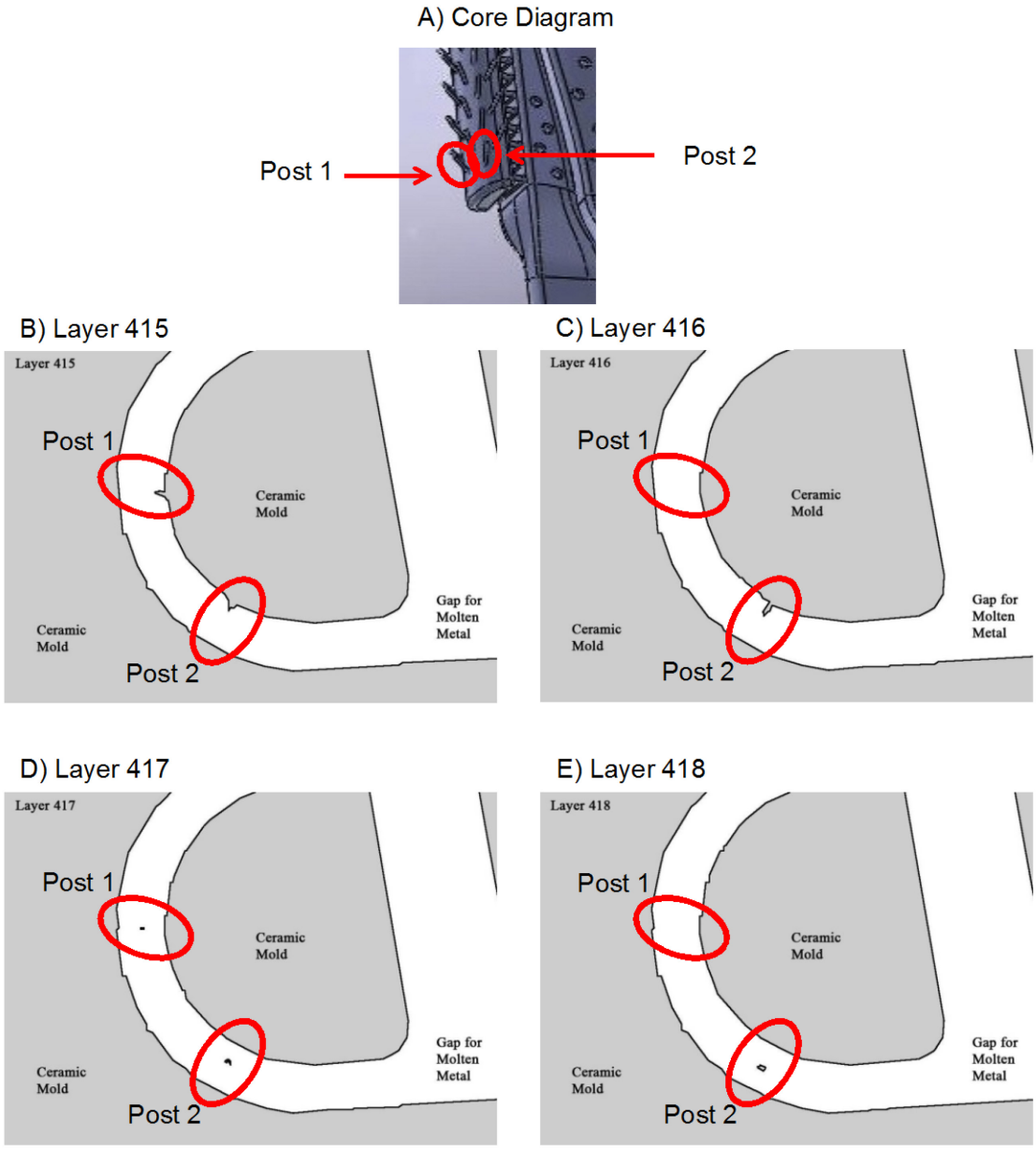

Figure 3.8 A) Model indicating two posts, post 1 and post 2, which are indicated in the vector files in B-E. Note that the vector files are prepared assuming 100 µm layers. B) Vector file of layer 415. C) Vector file of layer 416. D) Vector file of layer 417. E) Vector file of layer 418.

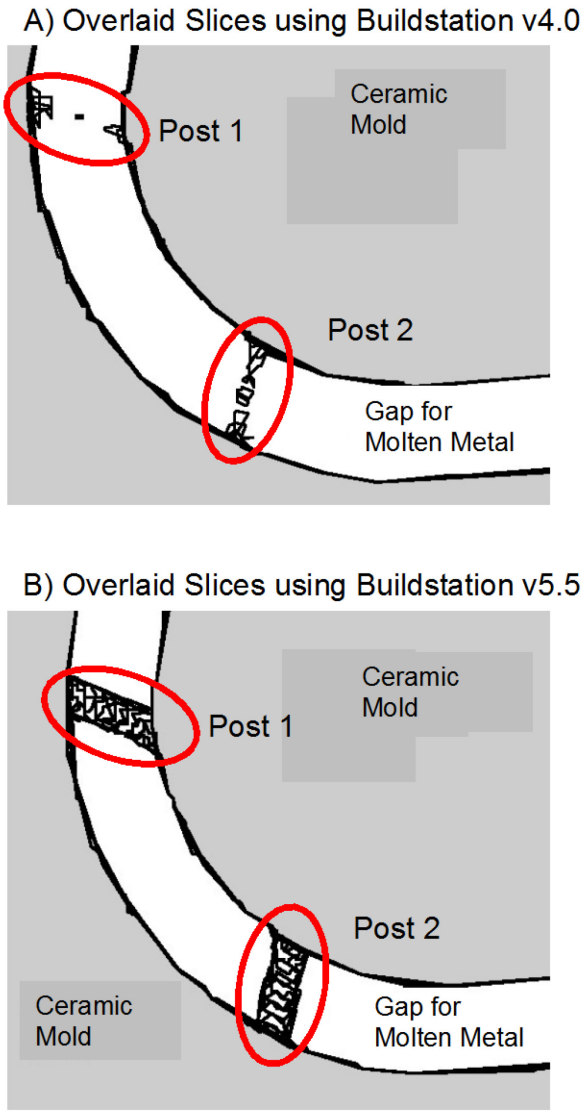

Figure 3.9 Overlay of slices using the software for Buildstation v4.0 (A) and v5.5 (B). Note that four of the slices overlaid in (A) are shown in Figure 3.8B-E. The black lines indicate the border vector, which defines the edge of the cured region. The white region is the gap for molten metal and the shaded region is the ceramic mold.

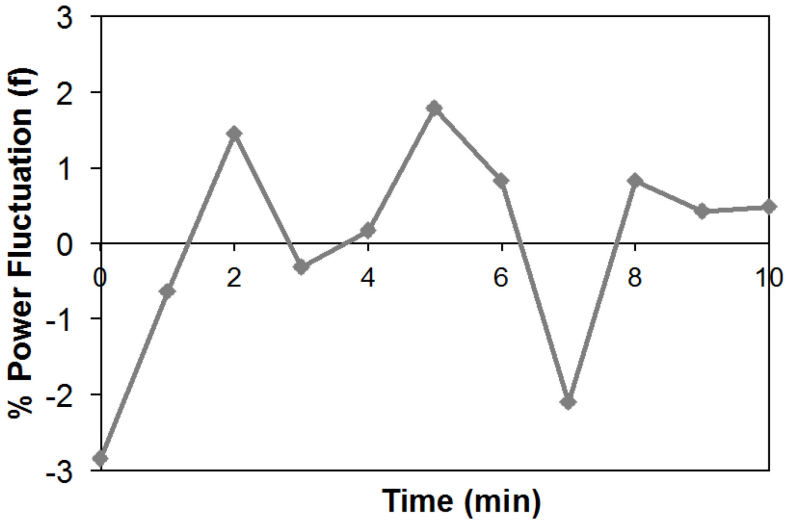

Figure 3.10 Fluctuations in laser power as a function of time, normalized by the average power.

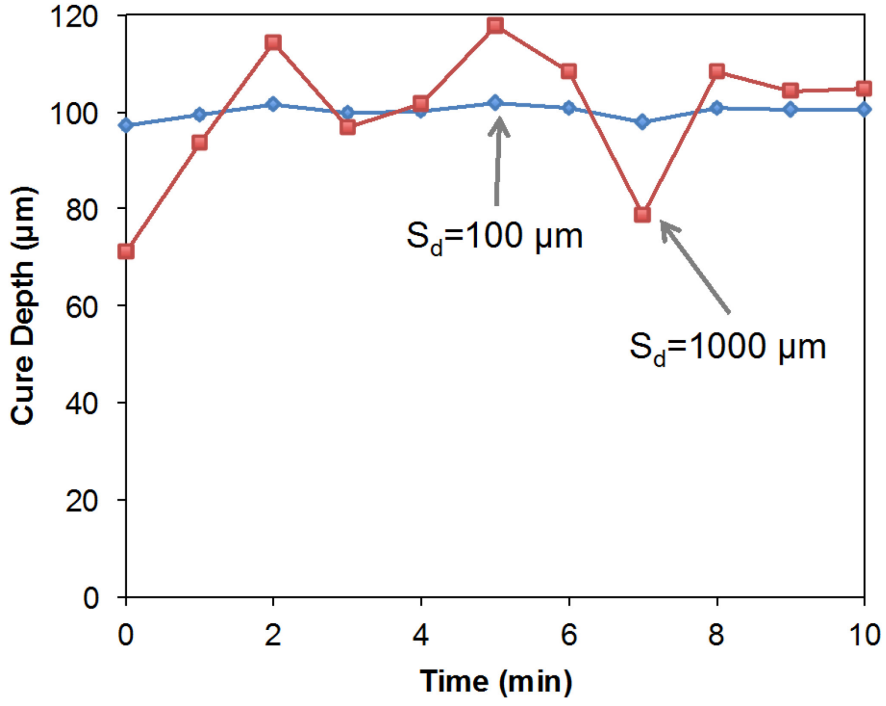

Figure 3.11 Predicted change in cure depth as a result of the power fluctuations shown in Figure 3.10, assuming a nominal cure depth of 100 µm and a sensitivity of 100 µm or 1000 µm.

Chapter 4

Effect of Sedimentation on Cure Depth

4.1 Introduction

Photopolymerization in ceramic stereolithography and LAMP occurs at the surface of the suspension, so it is important that the surface be level and have known properties. Ceramic stereolithography vats can be 30 cm deep, although only the top 50-250 μm are significant to the curing of the suspension. Building a single layer involves curing the layer plus recoating the surface. A delay is typically incorporated between layers as a way to increase the surface smoothness. A longer delay gives the resin more time to flow off of the cured regions, so that the layers are smooth for building. Alternatively, the suspension viscosity can be reduced so that it flows better and the surface becomes more even. It is assumed that these changes do not affect the properties of the surface layer with respect to the bulk properties of the suspension.

However, for ceramic suspensions, the suspension at the surface can be very different than the suspension in the bulk. The ceramic particles dispersed within the liquid medium are susceptible to the effects of gravity. Increasing the delay time between layers increases the time for settling of the particles within the suspension. Settling of ceramic particles has been observed in ceramic stereolithography on both the microscopic and macroscopic levels. Long delay times have been linked to segregation of particle sizes within a given layer.[1] Similarly, sediment has been observed at the

bottom of the vat after long builds. The analysis of sedimentation has focused on the problems of having a green body with a variable solids loading, potentially resulting in cracks. However, settling can also result in changes to the photocuring parameters (E_d, S_d) of the suspension. This chapter will focus on the changes to the photocuring behavior of the suspension as the ceramic particles sediment within the suspension.

4.1.1 Settling Velocity

The most basic analysis of settling is the case of a single particle in a fluid medium. Stokes' law predicts the settling velocity is simply due to the effects of gravity on a particle. The Stokes' velocity, v_s, is

$$v_s = \frac{(\rho_p - \rho_f) g d^2}{18\eta} \qquad \text{Eq. 4.1}$$

where ρ_p is the particle density, ρ_f is the fluid density, g is gravity, d is the particle diameter, and η is the viscosity of the fluid. The assumption that particles are non-interacting requires large distances between particles, which is relevant only for very dilute suspensions. For concentrated suspensions, such as those used for stereolithography, Stokes' law grossly overestimates the sedimentation rate.

Richardson and Zaki investigated the sedimentation of uniform spheres at volume fractions from 5% to 60.6%, and proposed a simple correction factor to account for hindered settling of uniformly sized particles in a fluid medium. In this case, the velocity of the particles decreases due to the drag from other nearby particles. The increased drag is the only interparticle interaction that is considered; other forces such as electrostatic forces are ignored. The hindered velocity, v_h, is related to the Stokes' velocity by

$$v_h = v_s(1 - \Phi)^{n_{RZ}} \qquad \text{Eq. 4.2}$$

where v_s is the Stokes' velocity, Φ is the volume fraction of the particles and n_{RZ} is the correction exponent.[2] Maude and Whitmore followed this up with a more generalized study that also accounts for the Reynolds number of the particles.[3] More recently a comparison of four models was performed by Koo, who found that all the models converged for volume fractions larger than about 40%, with the Richardson-Zaki model accurate assuming n_{RZ}=5.5.[4] For this work, the hindered velocity will be taken as the Richardson-Zaki model with the Koo exponent of 5.5.

The Stokes' and hindered Stokes' models lead to a simplistic settling behavior since particles are assumed to be of uniform size and have the same settling velocity. Initially (t=0) the ceramic suspension is uniform. Over time (t>0), a denuded layer forms which is void of particles (Φ=0). The thickness of the denuded region is equal to the product of velocity and time (thickness=v*t), as shown in Figure 4.1. A dense sediment forms at the bottom, but this will be ignored as it does not contribute to the curing properties at the surface. It will be assumed that the suspension vat is sufficiently deep that the sediment at the bottom does not affect the sedimentation of the remainder of the suspension.

Sedimentation can change the composition of the suspension near the surface, which can change the curing behavior. This chapter addresses the change in curing in terms of the cure parameters (sensitivity and critical energy dose), then uses these to predict the cure depth as a function of time. This analysis will be for spherical monodispersed powders, to simplify the sedimentation behavior. However, experiments use ceramic powders that have broad particle size distributions, so the effect of this will

also be discussed. There is no closed-form solution for the sedimentation rate of these suspensions; instead, the change in solids loading as a function of depth can be characterized using an analytic centrifuge. Practically, the significance of sedimentation will depend on the amount of mixing that occurs between layers. For LAMP, where a new layer of suspension is laid down for each layer, the relevant sedimentation time is on the order of seconds to minutes. However, if little mixing occurs at the surface of a 24-hour stereolithography build, then sedimentation is significant over this entire time interval.

4.1.2 Predictive Curing Models

Understanding the behavior of the photopolymerization process is important for ceramic stereolithography and LAMP.[5] As detailed by the absorption model and inhibitor-exhaustion model[6-8] explained in Chapter 2, the resin sensitivity, S_d, and the critical energy dose, E_d, are dependent on the volume fraction of ceramic particles in the suspension. E_d and S_d will be affected by the sedimentation of particles, so the cure depth is also expected to vary with settling time.

As detailed in Chapter 2, the resin sensitivity, S_d, of ceramic suspensions is given by:

$$\frac{1}{S_d} = \frac{1}{l_{Sc}} + (1 - \Phi)(c_P \varepsilon_P + c_D \varepsilon_D) \qquad \text{Eq. 4.3}$$

where l_{sc} is the scattering length, Φ is the volume fraction of ceramic powder in the suspension, c_P is the concentration of the photoinitiator, ε_P is the extinction coefficient of the photoinitiator, c_D is the concentration of the dye, and ε_D is the extinction coefficient of the dye.[7; 8] The scattering contribution is a function of solids loading as

$$\frac{1}{l_{Sc}} = S(\Phi) = \beta\Phi - \left(\frac{\beta}{2\Phi_{max}}\right)\Phi^2 \qquad \text{Eq. 4.4}$$

where β is a fitting parameter that describes the rate of change of the scattering contribution with the volume fraction of powder and Φ_{max} is the volume fraction corresponding to the peak of the scattering contribution.[8] The scattering contribution goes to zero as the solids loading approaches zero, as this corresponds to an infinite scattering distance. This chapter will focus on silica-based suspensions, which can be characterized as absorption-dominated. In this case, S_d is expected to increase with volume fraction of powder, reaching a maximum around 50 vol%.

Similarly, the critical energy dose (E_d) can be predicted from the individual components in the suspension using the inhibitor exhaustion model (see Chapter 2). For the absorption-dominated silica suspensions, the critical energy dose decreases linearly as a function of solids loading as[6; 8]

$$E_d(\Phi) = E_d(\Phi = 0) - K_6\Phi = K_6(1 - \Phi) \qquad \text{Eq. 4.5}$$

where $E_d(\Phi=0)$ is the critical energy dose in the absence of powder and K_6 is a combined constant. This constant is given by

$$K_6 = \frac{h\nu}{\Omega}(\gamma_{INH}c_{INH} + \gamma_D c_D)\frac{1}{c_P\varepsilon_P} \qquad \text{Eq. 4.6}$$

where γ_{INH} is the number of radicals removed per inhibitor (such as oxygen or added quinone), c_{INH} is the concentration of the inhibitor, γ_D is the number of radicals that were not generated due to the presence of the dye, h is Plank's constant, ν is the frequency of the light, and Ω is the number of free radicals given off per photon absorbed. Thus, the critical energy dose can be predicted for any solids loading.

4.2 Suspension Properties

Assuming a homogeneous suspension, the predictive models can be used to determine the expected photocuring characteristics of a ceramic suspension. However, the settling in ceramic suspensions can significantly alter the cure behavior. To find the cure depth when particles are settling, the solids loading at each increment of depth must be known. The energy dose can then be calculated for each depth, along with the new sensitivity (S_d) and critical energy dose (E_d) for the composition at that depth. Wherever the energy is above E_d, curing occurs. For example, assume that a silica suspension has the composition given in Table 4.1. Stokes' law predicts a settling velocity of 5300 μm/hr, while the hindered Stokes' velocity is only 34 μm/hr. The Richardson-Zaki model predicts that hindered settling decreases the velocity by a factor of 150. The photocuring parameters of the denuded layer and the bulk can be extracted from the information in the Tomeckova papers, as the compositions are very similar.[6-8] From these papers, the relationship between scattering coefficient, S, and volume fraction can be found, and is shown in Figure 4.2. It is predicted that the scattering coefficient increases parabolically as given by Eq. 4.4. However, it was observed that the scattering coefficient only has a linear dependence, with β of 14.111 cm^{-1}. This indicates that the second order term is much smaller than the linear term, and can be neglected. The linear dependence has the scattering coefficient approaching zero as the volume fraction approaches zero, as expected. The resin sensitivity can be predicted from

$$\frac{1}{S_d} = \beta\Phi + (1-\Phi)(c_P\varepsilon_P + c_D\varepsilon_D)$$
$$= 0.00141\ \mu m^{-1} \times \Phi + (1-\Phi)\ 0.00778\ \mu m^{-1} \quad \text{Eq. 4.7}$$

The resin sensitivity in the bulk suspension, $S_d(\Phi=60\%)$, is 255 μm and the sensitivity in a denuded suspension without particles is given by $S_d(\Phi=0\%)=129$ μm. Similarly, extrapolated data from the Tomeckova papers predicts that K_6c_p is equal to 3.1 mJ-mol/cm^2-L. For a concentration of 0.20 mol/L of photoinitiator, this gives K_6 as 15.5 mJ/cm^2. Thus, the critical energy dose can be predicted as

$$E_d(\Phi) = (1-\Phi)K_6 = (1-\Phi)15.5\,\frac{mJ}{cm^2} \quad \text{Eq. 4.8}$$

The critical energy dose for the bulk suspension, $E_d(\Phi=60\%)$, is 6.2 mJ/cm^2 and the critical energy dose for a denuded suspension without particles is given by $E_d(\Phi=0\%)=15.5$ mJ/cm^2. The predicted resin sensitivities and the critical energies are given in Figure 4.3, showing their dependence on volume fraction of powder.

4.3 Hindered Stokes' Model

First, the attenuation as a function of time will be analyzed for the model system of monodisperse spheres. This will assume that the sedimentation velocity of the particles is uniform. The solids loading is high (60 vol%), so the particles are expected to interact while settling and the hindered Stokes' velocity should be used. For the composition given in Table 4.1, the hindered Stokes' velocity (v_h) is 34 μm/hour. This means that after one hour, it is expected that the suspension has a 34 μm denuded layer above a homogenous suspension.

4.3.1 Time Dependence: S_d

Assuming that the segments (the denuded layer and the bulk suspension) are individually Beer-Lambert mediums, the energy attenuation can be plotted as a function of distance for any given time. For example, assume that the suspension is exposed to an energy dose of 25 mJ/cm^2 at the surface. The energy attenuation after three hours is shown in Figure 4.4 with the dashed line indicating the division between the denuded layer and the bulk suspension. The energy attenuates through the denuded region with a sensitivity of 129 μm. The energy has attenuated to 11.4 mJ/cm^2 at the depth of the interface between the denuded region and the bulk suspension, located 102 μm below the surface of the suspension. As the light propagates deeper, it goes through the bulk ceramic suspension which has a sensitivity of 255 μm. Overall, the sensitivity of liquid is dependent on the depth due to the settling of ceramic particles. The overall suspension is no longer a Beer-Lambert medium, since the slope of the logarithm of energy versus depth is no longer linear throughout the entire suspension.

A similar analysis can be performed for a variety of settling times. Figure 4.5 shows how the energy attenuation varies over time. It can be seen that initially, after zero hours of setting, the logarithm of energy decreases linearly with depth, indicating that the suspension is a Beer-Lambert absorber. As time increases from one hour to six hours, the depth of the denuded region increases from 34 to 204 μm, resulting in a change in the inflection point when the logarithm of energy is plotted versus depth. The result is that after six hours, the energy dose is much smaller at a depth of 200 μm than it is after only one hour of settling. This is significant, as stereolithography can require 24-36 hours to

build a single part. Depending on the specifics of the recoating mechanism, there might be little or no mixing during recoating.

4.3.2 Time Dependence: E_d

Furthermore, the Tomeckova models predict that the critical energy dose of the suspension will be dependent on the solids loading of the suspension. Since the simple settling models predict the formation of a denuded layer, this will result in a discontinuity in E_d as a function of depth.

Continuing the example from above, the denuded layer and the ceramic suspension have different critical energies as given by Eq. 4.8. Wherever the energy is above the critical energy dose, curing occurs. Figure 4.6 shows the energy over the depth of the suspension along with the critical energies in each region, for suspensions after 0, 1, 3, or 6 hours of settling. The shaded regions indicate the depths where curing occurs, whether in the bulk suspension or the denuded region. The simplest case is that of immediate curing (t=0 hrs, Figure 4.6A). Curing occurs in the suspension up to a depth of 356 μm, at which point the energy is equal to the critical energy dose. At larger depths, the energy dose remains below the critical energy dose, so no curing occurs. After one hour of settling (Figure 4.6B), the denuded region has a depth of 34 μm. The energy attenuates from 25 mJ/cm^2 to 19.2 mJ/cm^2 over this region. This entire region is above the critical energy dose for 0% powder, so the entire denuded region is cured. The energy continues to propagate through the bulk suspension, attenuating with the sensitivity of the bulk. Curing occurs for all depths in the bulk where the energy is above $E_d(\Phi=60\%)$. This corresponds in curing in the ceramic suspension from a depth of 34 μm

to 322 μm. The overall cure depth for a suspension that has sedimented for one hour is 322 μm, with the cured region consisting of 34 μm of denuded region and 288 μm of cured suspension containing ceramic particles. Skipping ahead to a settling time of six hours (Figure 4.6D), the interface between the denuded region and the bulk suspension is at a depth of 204 μm. The energy attenuates from 25 mJ/cm^2 to 5.14 mJ/cm^2 over this region. This results in curing up to a depth of 61 μm. The energy dose in the ceramic suspension is below that of the critical energy dose, so the ceramic region does not cure. The cured region after six hours of settling is 61 μm deep, and does not contain ceramic particles.

The curing behavior after three hours (Figure 4.6C) is more complicated. At this time, the denuded region has a depth of 102 μm. Over this region, the energy dose attenuates from 25 mJ/cm^2 to 11.3 mJ/cm^2. Since the critical energy dose of the denuded region is 15.5 mJ/cm^2, only 61 μm of the denuded region cures. Even though the denuded region did not completely cure, the energy continues to propagate through the ceramic suspension, beginning this region with an energy dose of 11.3 mJ/cm^2. Since this is above the critical energy dose of polymerization for the ceramic region ($E_d(\Phi=60\%)$=6.2 mJ/cm^2), the ceramic region begins to cure. The curing occurs over a depth of 102 μm to 254 μm in the ceramic suspension, at which point the energy dose is again equal to the critical energy dose. The overall cured region at this time is a cured denuded region with a depth of 61 μm, followed by a denuded liquid gap from 61 μm to 102 μm, followed by curing of ceramic from 102 μm to 254 μm. The cured region is not continuous for this condition.

4.3.3 Curing Conditions

Generalized, the discontinuity in critical energy dose, E_d, over distance can lead to a few possible curing scenarios that are distinguished by two characteristic times, t_1 and t_2. The three curing scenarios are:

- Case 1: The entire denuded layer is solidified along with part of the ceramic suspension (Figure 4.7A). This occurs when the settling time is small ($t < t_1$).
- Case 2: The denuded region and the ceramic suspension partially cure, with a liquid denuded layer in between the solid regions (Figure 4.7B). This occurs for intermediate time scales ($t_1 < t < t_2$).
- Case 3: The entire denuded layer is solidified but none of the ceramic suspension is solidified (Figure 4.7C). This occurs for large settling times ($t > t_2$).

These occur when the interface between the denuded layer and bulk ceramic suspension has reached certain levels. These critical depths, D_1 and D_2, are dependent on the incident energy and the photocuring characteristics of the suspension. Alternatively, the separations between the curing conditions can be expressed as characteristic times, t_1 and t_2, given a certain settling velocity. The first characteristic depth (D_1) and time (t_1), describes when the curing between the denuded region and the bulk suspension becomes discontinuous. The first critical depth is

$$D_1 = S_d(\Phi = 0) \times \ln\left(\frac{E_0}{E_d(\Phi = 0)}\right) \qquad \text{Eq. 4.9}$$

where E_0 is the incident energy dose, $S_d(\Phi=0)$ is the resin sensitivity in the denuded region (where $\Phi=0$), and $E_d(\Phi=0)$ is the critical energy dose in the denuded region. The characteristic time is given as

$$t_1 = \frac{S_d(\Phi = 0)}{v_h} \times \ln\left(\frac{E_0}{E_d(\Phi = 0)}\right) \qquad \text{Eq. 4.10}$$

The second characteristic depth, D_2, is the depth at which curing no longer occurs in the bulk suspension (with powder). This represents the end of the discontinuous curing. D_2 is given by

$$D_2 = S_d(\Phi = 0) \times \ln\left(\frac{E_0}{E_d(\Phi = 60\%)}\right) \qquad \text{Eq. 4.11}$$

where $E_d(\Phi=60\%)$ is the critical energy dose in the denuded region. The second characteristic time, t_2, is given by

$$t_2 = \frac{S_d(\Phi = 0)}{v_h} \times \ln\left(\frac{E_0}{E_d(\Phi = 60\%)}\right) \qquad \text{Eq. 4.12}$$

These characteristic times and depths can be used to predict the curing scenario for a given ceramic suspension.

4.3.4 Cure Depth for Short Times

The effect of sedimentation on the cure depth can be described for suspensions with continuous curing. Discontinuous curing is not desired for ceramic stereolithography suspensions, so the times will be limited to those less than t_1. For the suspension described in the above sections, the change in cure depth can be plotted over time. The sedimenting ceramic particles cause the effective photoinitiator and dye concentration to be larger in the denuded region than in the bulk suspension, increasing the absorption and limiting the depth of cure. Using the hindered settling model, the cure depth is expected to decrease linearly as a function of time. This is predicted for the model suspension, as demonstrated in Figure 4.8.

4.4 Comparison of Particle Sizes

One method of decreasing the effect of particle sedimentation on curing is through the use of smaller particles. From Stokes' equation (Eq. 4.1), it can be seen that the sedimentation velocity is proportional to the square of the particle size. Thus, decreasing the particle size by a factor of two will result in a decrease in sedimentation by a factor of four. Figure 4.9 shows the settling velocity as predicted with the Stokes' model (A) and hindered Stokes' model (B). Note the large differences between the Stokes' velocities and the hindered Stokes' velocities. Assuming a suspension with 60 vol% powder, the hindered Stokes' velocities will be 150 times larger than the simple Stokes' model, due to the interparticle interactions related to the Reynolds number of the suspension (as given by the Richardson-Zaki model with Koo exponent of 5.5). It can be seen from Figure 4.9 that small decreases in particle size are effective at reducing the sedimentation. For example, compare three suspensions with particle diameters of 1 μm, 4.84 μm, and 8.5 μm (indicated with markers in the graphs of Figure 4.9 and Figure 4.10). Stokes' model predicts that 8.5 μm particles settle 3 times faster than 4.84 μm and 72 times faster than 1 μm particles.

For curing, the suspensions can still be characterized by t_1 and t_2, as shown in Figure 4.10. Note that the effects of particle size on the scattering coefficient are ignored in this analysis. The critical times scale as $1/d^2$, so the characteristic times for the small particles are much larger than the large particles. This corresponds to more time for uniform curing, without worrying about discontinuities in the cured region. The cure depth can be plotted as a function of time (over the region of continuous curing where

$0 \leq t \leq t_1$), as shown in Figure 4.11. It can be seen that the sedimentation of the 1 μm particles is very small, and only results in small variations in cure depth over 24 hours. In contrast, the 4.84 μm and 8.5 μm particles both have serious sedimentation over that same time, and are expected to exhibit delaminated curing after 1.8 and 6.0 hours, respectively.

4.5 Real Suspension Behavior

The ceramic suspensions used for ceramic stereolithography have broad particle size distributions, unlike the ideal monodisperse suspensions considered above. This broad particle size distribution results in a complicated distribution of settling velocities for the particles; there is no closed-form equation for the sedimentation velocities. In this section, experimental sedimentation velocities are used to predict the change in cure depth as a function of time.

4.5.1 Sedimentation Behavior

A polydisperse ceramic suspension has a range of sedimentation velocities, with large particles settling faster than the smaller particles. The smaller particles dominate the sedimentation behavior, such that all settling velocities are lower than if the suspension contained uniform particles with size given by the average particle size (d_{50}) of the powder. This is particularly important for ceramic stereolithography, as the ceramic powders used typically have broad particle size distributions. One such powder is the silica CE44CSS powder (PCC Ceramics) with particle size distribution shown in Figure 4.12. Note that the particle size distribution was measured by Particle Technology

Labs using a Malvern® Mastersizer 2000. Particle size distributions are characterized by its average particle size, or d_{50}. The average particle size is volume-weighted, so that 50 vol% of the particles have a diameter of d_{50} or smaller. Similarly, a d_{10} and d_{90} can be specified for the particle size distribution, describing the breadth of the distribution. For the CE44CSS powder, d_{10}=2.03 μm, d_{50}=8.5 μm, and d_{90}=36.8 μm. There is no closed-form solution for predicting the settling velocity of a continuous size distribution, but this can be measured using an analytical centrifuge.

An analytical centrifuge can be used to measure the sedimentation velocities of suspensions. Once the distribution of sedimentation velocities is known for a suspension, this distribution can be multiplied by the sedimentation time to provide the volume fraction at a given cure depth as a function of time. The sedimentation velocities for the CE44CSS powder at a solids loading of Φ=60% were measured by Vladislava Tomeckova; the ceramic content as a function of depth after 1 hour of settling is shown in Figure 4.13.[9] For comparison, the predicted behavior (assuming the hindered Stokes' model) is also indicated for a monodisperse powder with a particle diameter of 8.5 μm; this predicts a front that has removed all particles to a depth of 34 μm after one hour of settling. As expected, the actual sedimentation is much less than predicted for a monodisperse suspension due to small particles hindering the motion of larger particles. Additionally, the variation in volume fraction with depth is much more gradual for the polydisperse case. These sedimentation characteristics for the polydisperse suspension are expected to change the curing behavior over time, as compared to an ideal monodisperse suspension.

4.5.2 Curing Behavior

The continuous variation in solids loading prevents discontinuous curing, but can still result in significant changes in cure depth over time. Combining the sedimentation data from Figure 4.13 with the curing models in section 4.1.2 allows the cure depth to be determined as a function of time. For each increment of time, the distribution of solids loading is found by multiplying the velocities by the time. Then, for each increment of depth, the sensitivity and critical energy are determined. This allows the energy attenuation to be calculated, even though the suspension is not homogeneous with depth. At each depth, the local energy is compared with the critical energy dose at that depth, to determine whether curing occurs. This continues until curing no longer occurs for the suspension. This has been done for a suspension with the same properties as in section 4.2 and Table 4.1, so the sensitivity is given by Eq. 4.7 and the critical energy dose is given by Eq. 4.8. The cure depth over time for an energy dose of 25 mJ/cm^2 is plotted in Figure 4.14. In this case, most of the particles have settled after 50 hours, such that the cure depth is decreased by a factor of 5. This framework can be used to determine the change in cure depth over time for any sensitivity and energy dose, provided that the sedimentation behavior is known.

Calculating the expected cure depth for a given energy dose allows for an analysis of the effect of the sedimentation on the cure properties of real suspensions. Suppose a build specified 250 μm layers with 100 μm of overcure (such that the overall cure depth was 350 μm), with sedimentation behavior given by Figure 4.14. In this case, only 100 μm of the layer would be curing after 48 hours of building, despite a nominal cure depth of 250 μm and the platform moving down 250 μm for each layer. This would

prevent adhesion between adjacent layers. This suspension would require a mechanical means to mix the suspension, so that it remained sufficiently homogeneous throughout the build. In an absorption-dominated suspension, the cure depth will decrease over time as the surface region loses ceramic particles due to settling. The loss of powder results in an increase in the relative concentration of the dye and photoinitiator within the suspension, leading to more absorption. For a scattering dominated case, such as an alumina suspension without any absorbing dyes, the cure depth could increase with time, as a result of the changes to the scattering behavior. Regardless of whether the cure depth increases or decreases over time, this is going to lead to a loss of resolution, as the cure properties are no longer well-defined. These changes might be within tolerance, or might require adjustments to improve the suspension homogeneity through means such as mechanical mixing. The analysis in this chapter demonstrates the importance of understanding how the cure parameters change over time and how they affect the part resolution.

4.6 Conclusion

It has been shown that sedimentation is significant to the curing properties of suspensions. For absorption dominated suspensions, decreasing the volume fraction of powder results in an increased critical energy dose and an increased resin sensitivity, causing the cure depth to decrease as a function of time. Two systems were investigated: a model system with monodisperse particles and an experimental system with a range of particle size distributions. The effect of sedimentation on the cure properties was predicted for both.

For the model system containing monodisperse particles, it was found that three curing scenarios are possible. Characteristic times, t_1 and t_2, can be used to separate these three regions. The first scenario is defined as $t \leq t_1$, and has curing occurring continuously in the denuded and bulk regions. The entire denuded zone is cured, along with a segment of the bulk. The second scenario occurs for $t_1 < t < t_2$, and results in discontinuous curing in the denuded and bulk regions. There is a portion of the denuded zone which cures, and then is followed by denuded liquid, and then curing again begins in the bulk region at the interface between the denuded and bulk regions. The final scenario occurs for $t \geq t_2$. In this case a portion of the denuded region is cured, and none of the bulk region containing ceramic particles cures. It was shown that decreasing the particle size results in slower sedimentation velocities. This results in less change in cure depth over time, and can be characterized by increases in t_1 and t_2.

For the real suspension, the predictive model was applied to a suspension with measured sedimentation velocities. It was shown again that for this absorption-dominated suspension the cure depth decreased as a function of time. Understanding the change in the cure depth over time is important for maintaining high resolution of ceramic stereolithography.

4.7 References

[1] C.-J. Bae, "Integrally Cored Ceramic Investment Casting Mold Fabricated by Ceramic Stereolithography," Ph.D. Dissertation, University of Michigan, (2008).

[2] J. Richardson and W. Zaki, "The sedimentation of a suspension of uniform spheres under conditions of viscous flow," *Chemical Engineering Science,* **3**[2] 65-73 (1954).

[3] A. D. Maude and R. L. Whitmore, "A generalized theory of sedimentation," *British Journal of Applied Physics,* **9**[12] 477 (1958).

[4] S. Koo, "Estimation of hindered settling velocity of suspensions," *Journal of Industrial and Engineering Chemistry,* **15**[1] 45-49 (2009).
[5] J. W. Halloran, V. Tomeckova, S. Gentry, S. Das, P. Cilino, D. Yuan, R. Guo, A. Rudraraju, P. Shao, and T. Wu, "Photopolymerization of powder suspensions for shaping ceramics," *Journal of the European Ceramic Society* (2010).
[6] V. Tomeckova and J. W. Halloran, "Critical energy for photopolymerization of ceramic suspensions in acrylate monomers," *Journal of the European Ceramic Society,* **30**[16] 3273-82 (2010).
[7] V. Tomeckova and J. W. Halloran, "Cure depth for photopolymerization of ceramic suspensions," *Journal of the European Ceramic Society,* **30**[15] 3023-33 (2010).
[8] V. Tomeckova and J. W. Halloran, "Predictive models for the photopolymerization of ceramic suspensions," *Journal of the European Ceramic Society,* **30**[14] 2833-40 (2010).
[9] V. Tomeckova, Personal Communication, 2010.

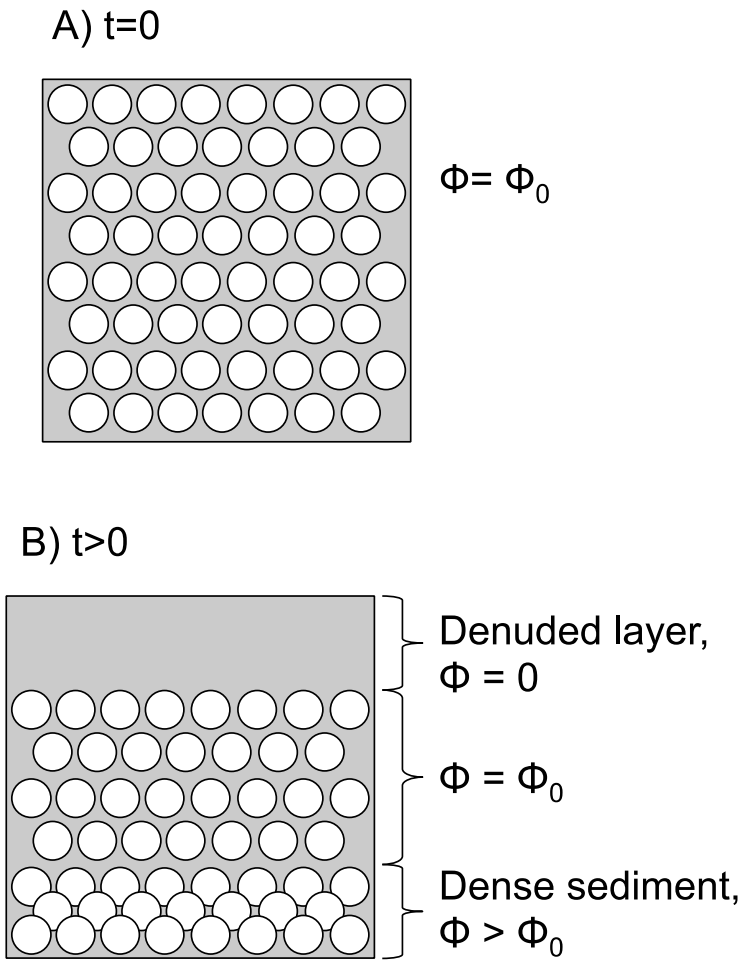

Figure 4.1 Schematic of the effect of simple sedimentation on the particle distribution in the ceramic suspension. A) At t=0, the particles are uniformly distributed. B) At t>0, a denuded layer has formed at the surface, which is free of particles. Below this, the bulk of the suspension has a solids loading given by the initial solids loading. A dense sediment has formed at the bottom due to the extra particles that have settled.

Table 4.1 Sample composition of a ceramic suspension. Note that the extinction coefficients are from Tomeckova *et al.*, at a wavelength of 355 nm.[7]

Chemical Name (Common Name)	**Description**	**Properties**
1,6-Hexanediol Diacrylate (HDDA)	Fluid Medium/ Monomer	Viscosity: 31 mPa-s Density: 1.04 g/cm^3
SiO_2 (Silica)	Particles	Average Particle Diameter: 8.5 μm Density: 2.2 g/cm^3 Volume Fraction in Suspension: 60% UV Absorption: transparent
1-Hydroxy-cyclohexyl-phenyl-ketone (Irgacure 184)	Photoinitiator	Concentration: 0.20 mol/L liquids Extinction Coefficient: 49 L/mol cm
Isomer mixture from the alkylation of 2-(2Hbenzotriazol-2-yl)-p-cresol with dodecane (Tinuvin 171)	UV Absorber	Concentration: 0.005 mol/L liquids Extinction Coefficient: 13600 L/mol cm

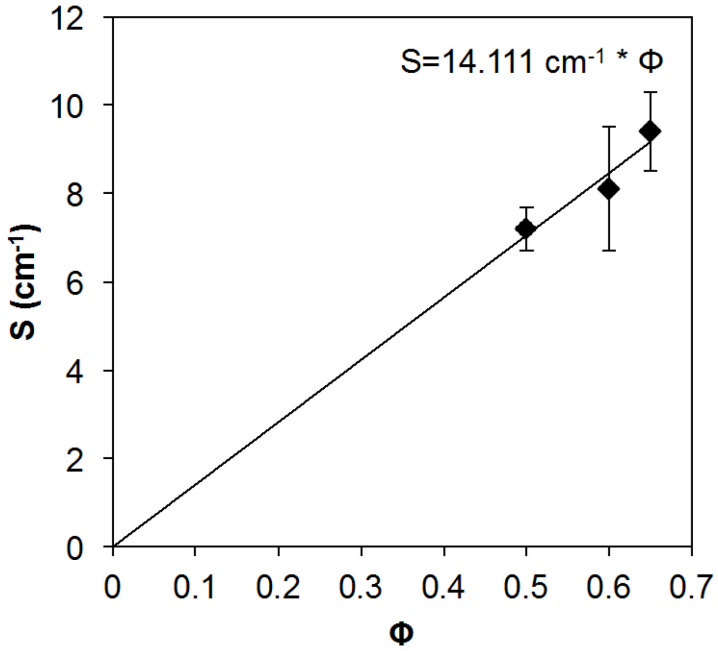

Figure 4.2 Scattering coefficient as a function of the volume fraction powder, showing their linear relationship. Note that the data points were obtained from the Tomeckova paper.[7]

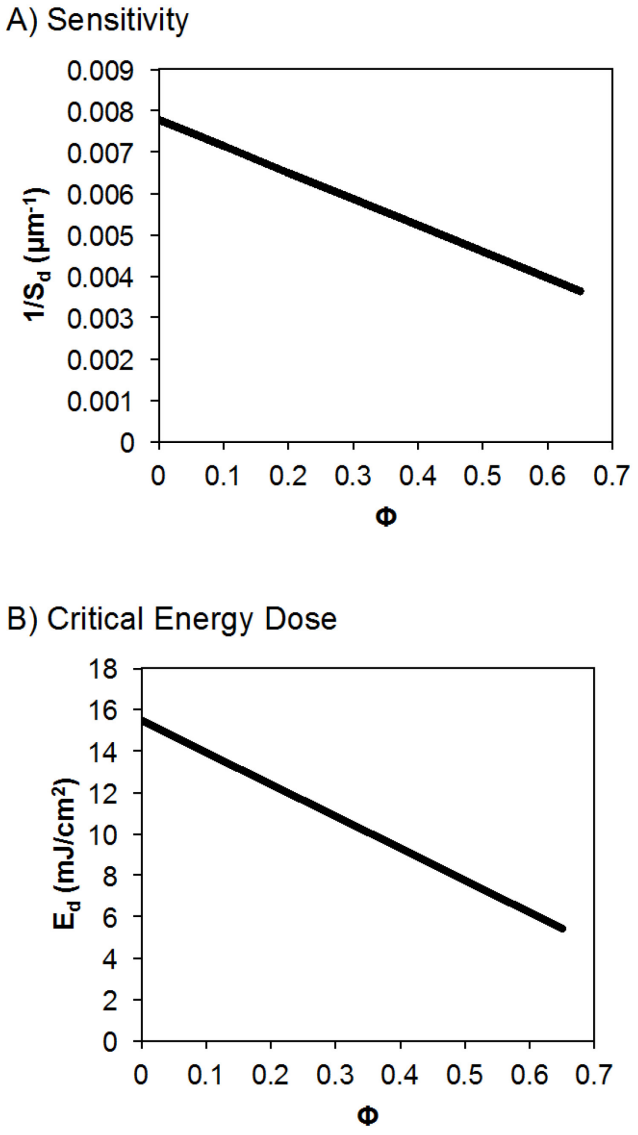

Figure 4.3 Predicted photocuring properties (sensitivity (A) and critical energy dose (B)) for the ceramic suspension as a function of solids loading.

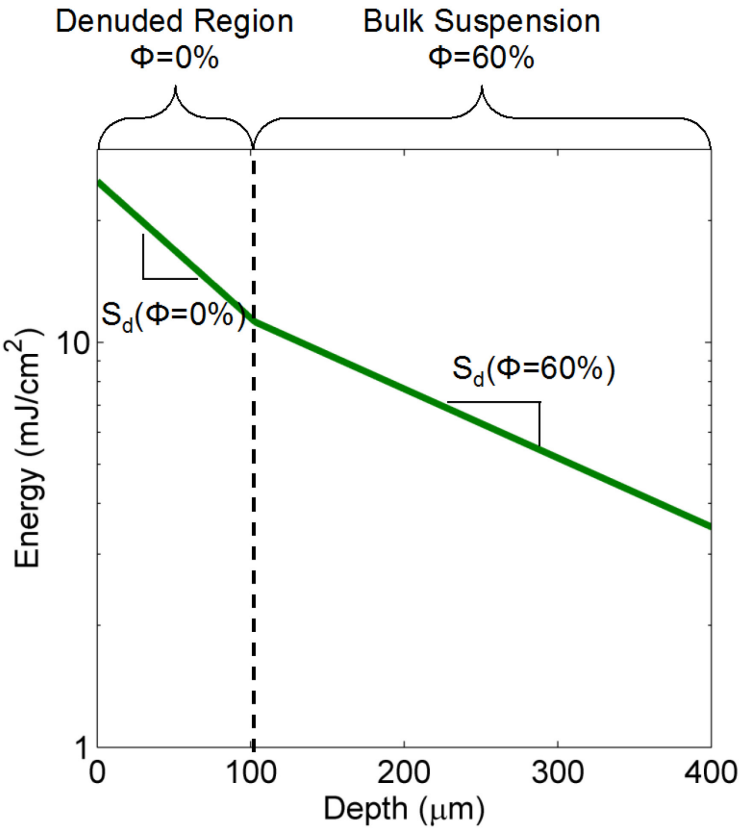

Figure 4.4 Energy attenuation as a function of depth after 3 hours of settling. The dashed line marks the boundary between the denuded layer and the uniform ceramic suspension.

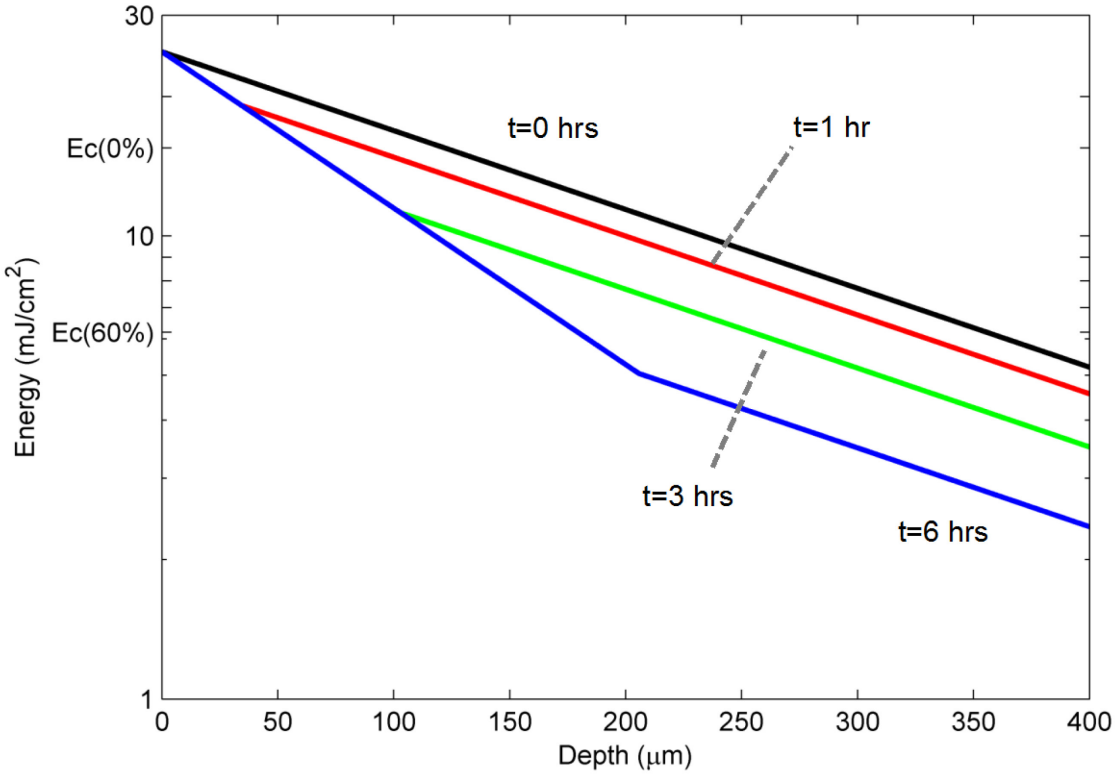

Figure 4.5 Attenuation of 25 mJ/cm^2 of incident energy dose as a function of depth after 0, 1, 3, and 6 hours of settling, assuming the settling velocity is given by the hindered Stokes' model.

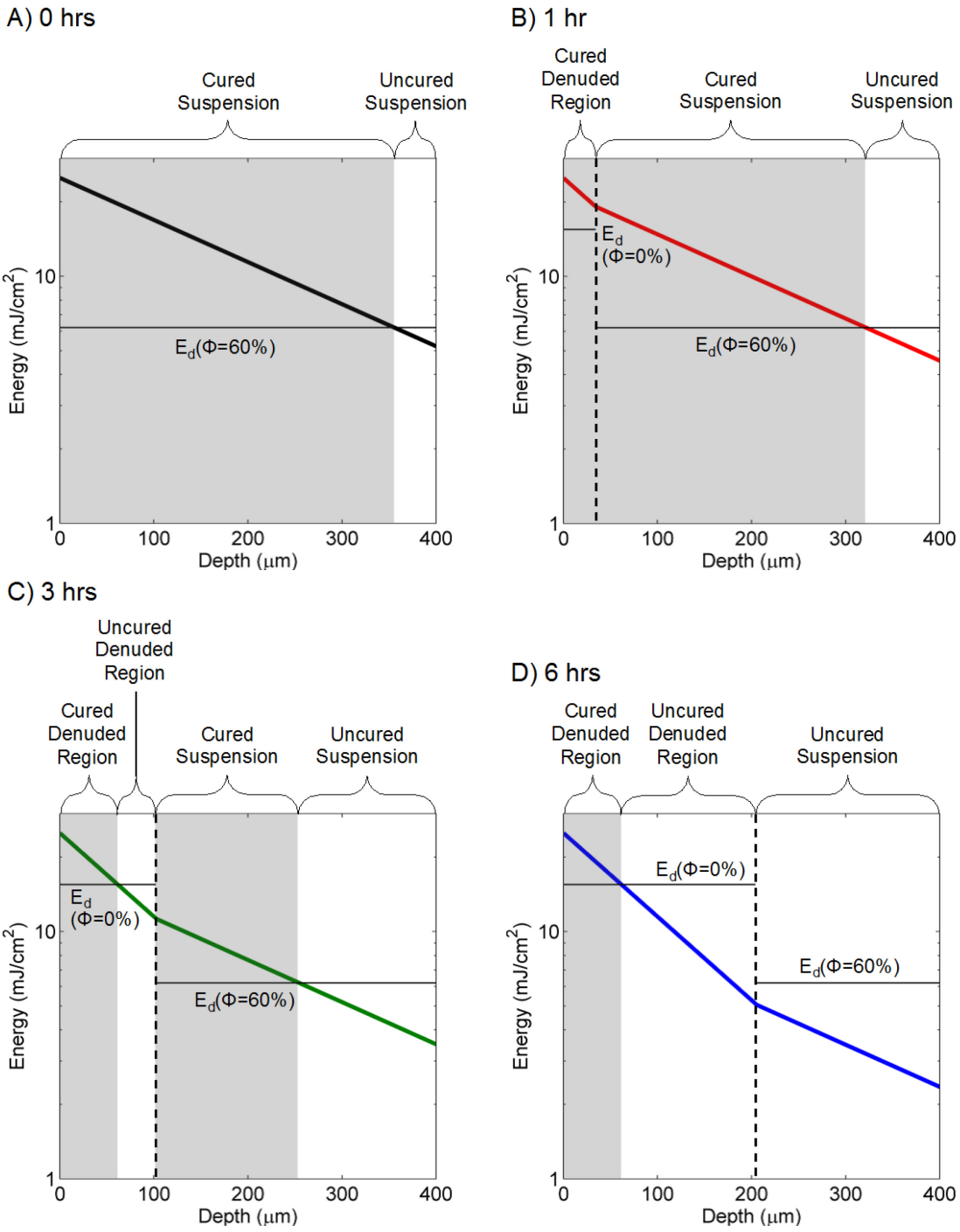

Figure 4.6 Plots of energy attenuation as a function of depth showing the curing conditions at 0, 1, 3, and 6 hours (A-D, respectively). The initial dose is 25 mJ/cm^2. The interface between the denuded region (Φ=0%) and the bulk ceramic suspension (Φ=60%) is indicated with a vertical dashed line. The gray region indicates the portion that is cured. Note that the critical energy dose for each region is indicated by the solid horizontal line (E_d(Φ=0%)=15.5 mJ/cm^2 and E_d(Φ=60%)=6.2 mJ/cm^2).

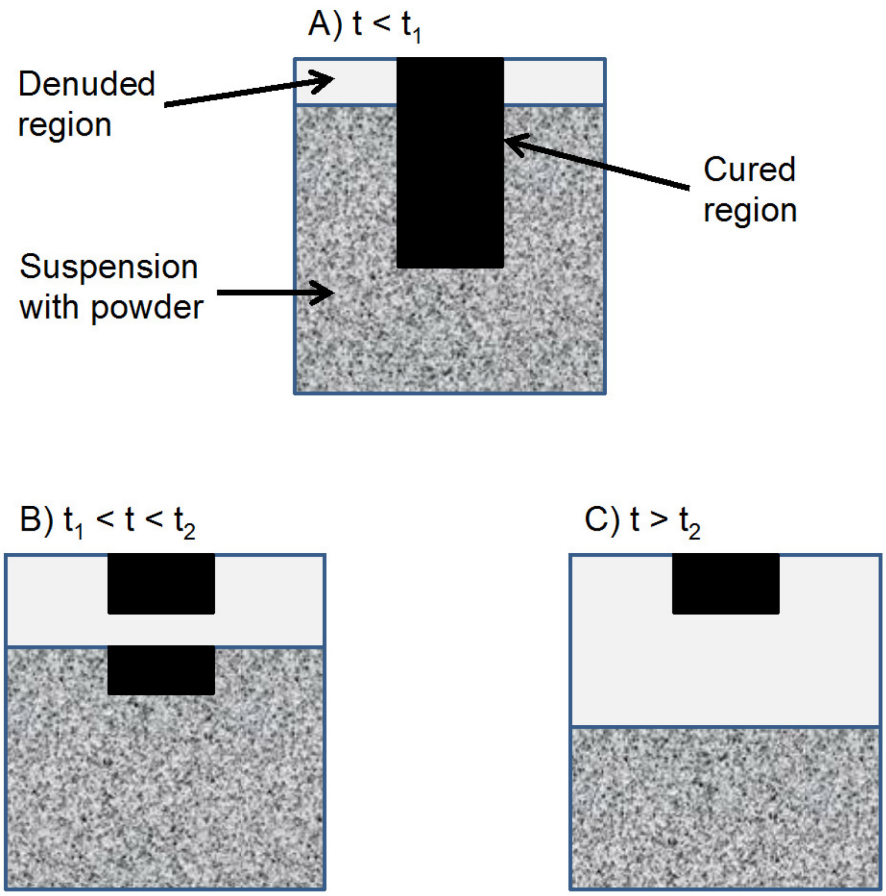

Figure 4.7 Schematics showing the three possible curing conditions that occur at short times (A), intermediate times (B) and long times (C).

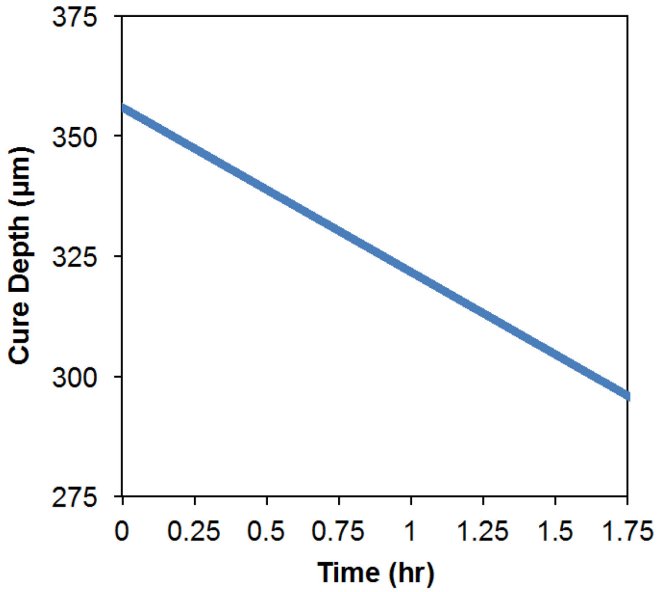

Figure 4.8 Change in cure depth over time for model suspension.

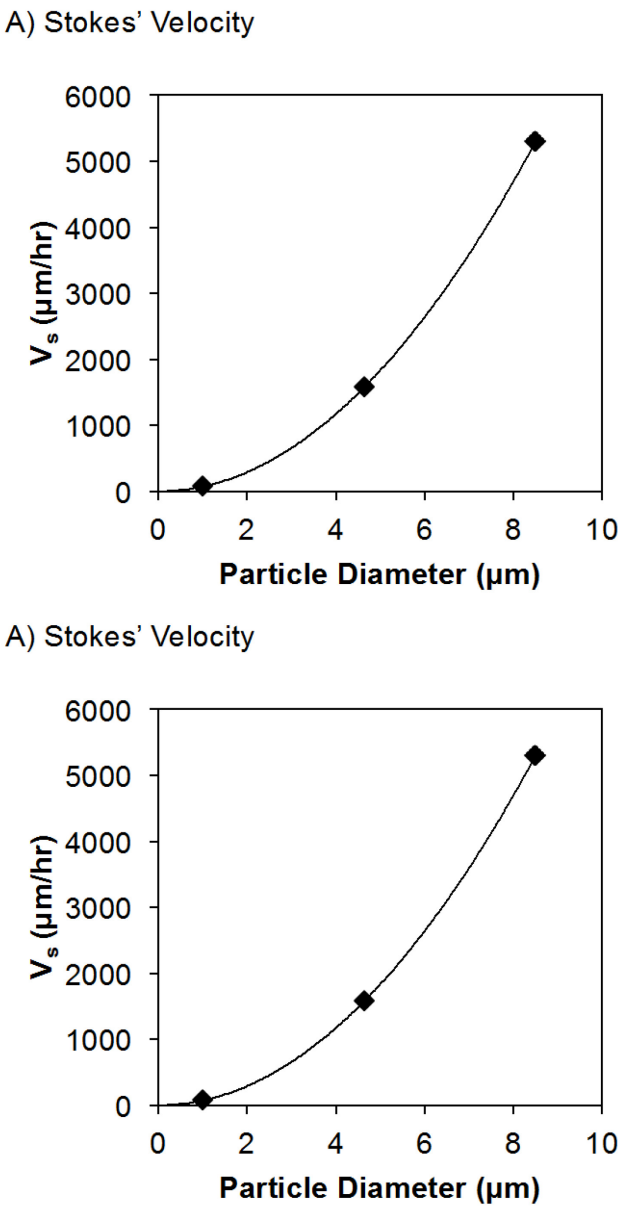

Figure 4.9 Predicted increase in sedimentation velocity as a function of particle size diameter, using Stokes' equation (A) and the hindered Stokes' model (B). Note the difference in axes for the two plots.

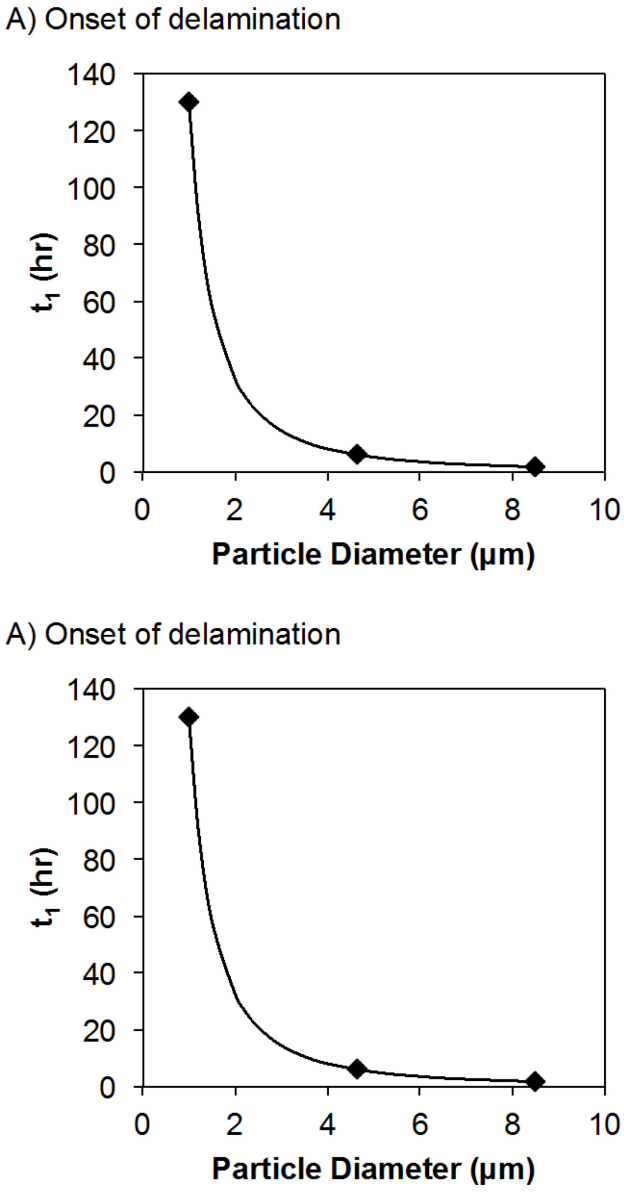

Figure 4.10 Change in critical times as a function of particle diameter. The onset of delamination (A) is given by t_1 and indicates when the cured regions are no longer continuous. The denuded curing time (B, given by t_2) indicates when only the denuded region cures.

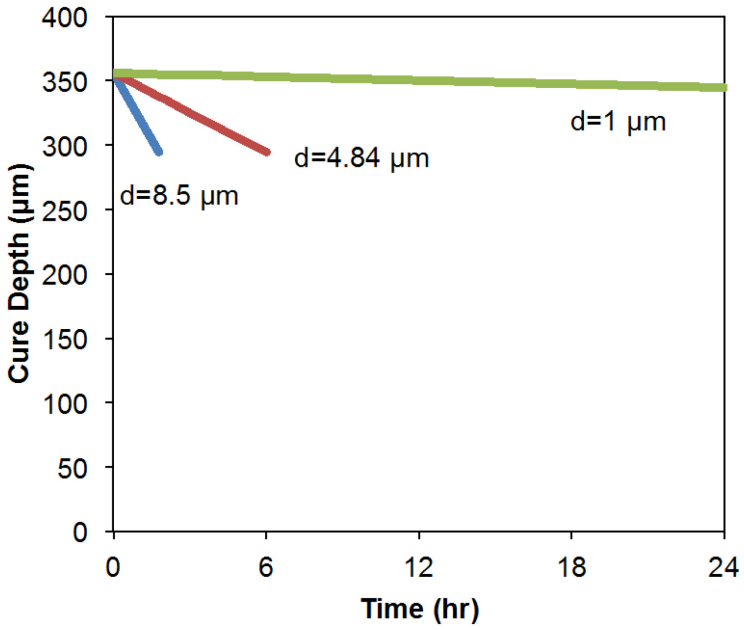

Figure 4.11 Effect of particle size on the decrease in cure depth over time. Note that cure depths are only shown until the onset of delamination (corresponding to t_1 and D_1).

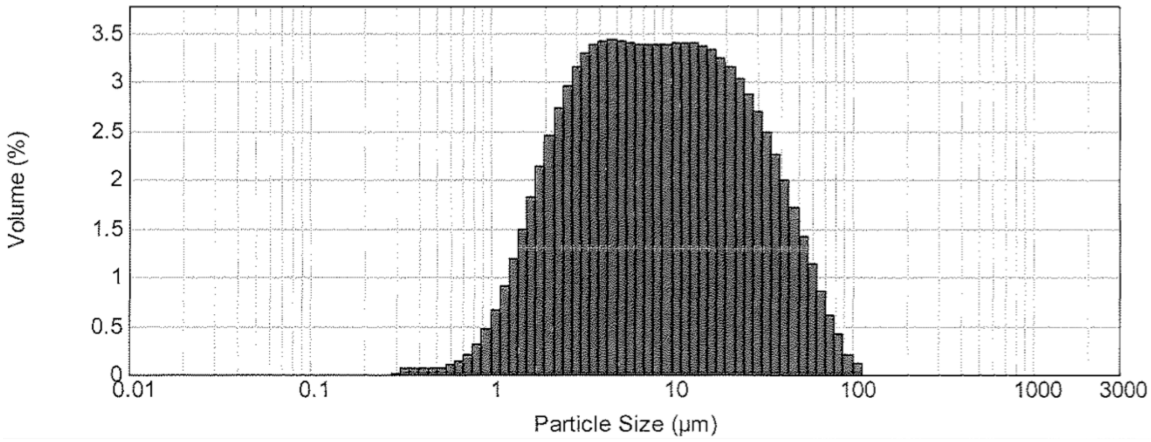

Figure 4.12 Particle size distribution for CE44CSS powder, as measured by Particle Technology Labs.

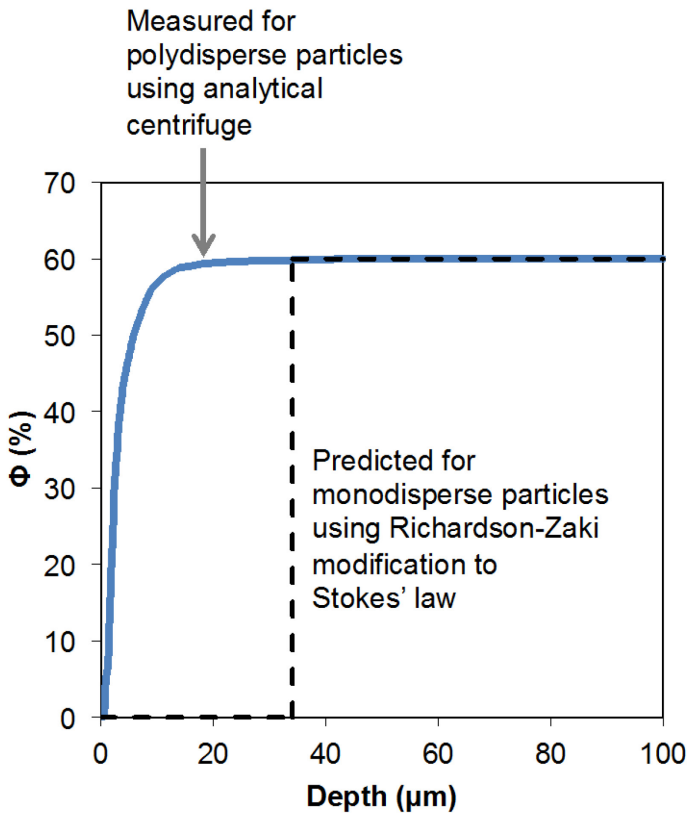

Figure 4.13 Change in solids loading as a function of depth after one hour of settling for a polydisperse suspension, as measured using an analytical centrifuge.[9] The particles have a size distribution characterized by d_{10}=2.03 μm, d_{50}=8.5 μm, and d_{90}=36.8 μm. For comparison, the prediction for hindered Stokes' settling is also shown, assuming a particle diameter of 8.5 μm. This predicts a front that has removed all particles to a depth of 34 μm.

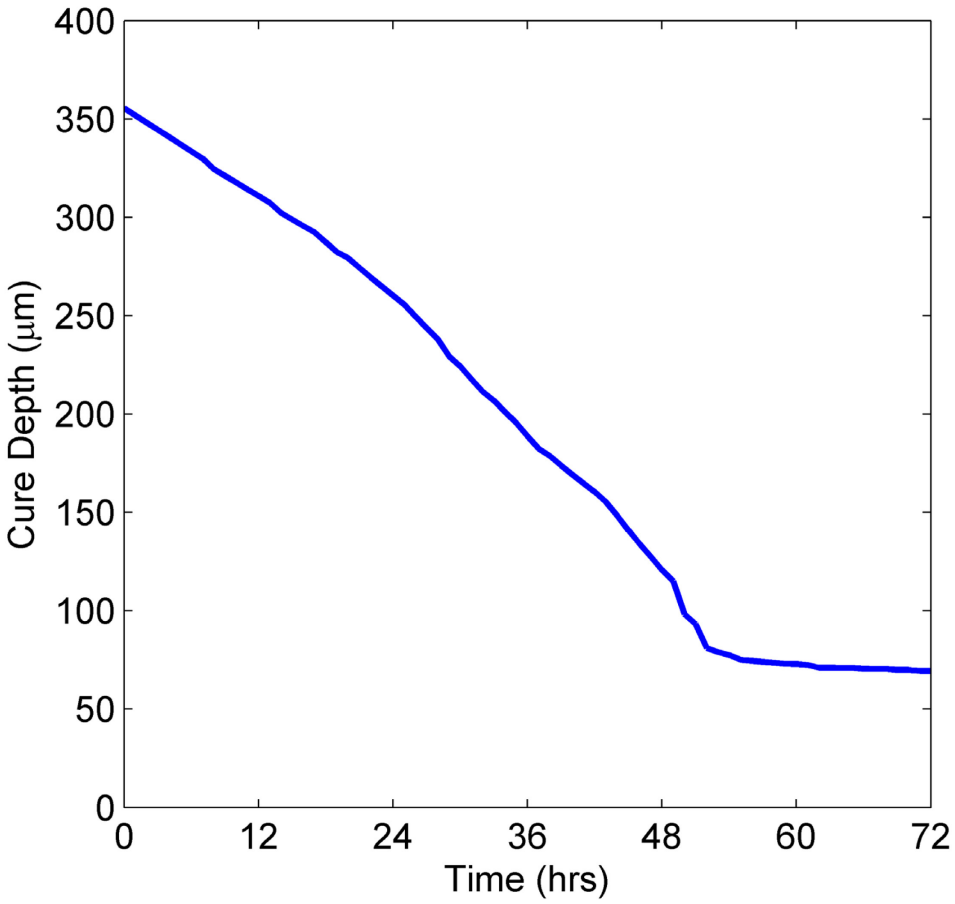

Figure 4.14 Change in cure depth as a function of time for a suspension exposed with an energy dose of 25 mJ/cm^2, calculated from sedimentation velocities measured using an analytical centrifuge.

Chapter 5

Linewidth in Absorption-Dominated Systems

5.1 Introduction

This chapter addresses the issue of predicting the cured shape that results from the photopolymerization of ceramic suspensions. A new apparatus has been developed to easily measure the cure shape for a variety of suspensions; this will be presented and verified in the chapter. Chapter 5 will also discuss the cure shape in absorption-dominated systems, looking at the effects of the dye concentration and photoinitiator concentration. Chapter 6 will focus on the effect of scattering on the properties, through the refractive index contrast as well as the solids loading in the suspension. The refractive index contrast will be adjusted using both inert diluents to vary the refractive index of the solution as well as a variety of powders with different refractive indices.

5.1.1 Motivation

One important aspect for improving ceramic stereolithography is understanding the shape of the cured profile that results from the incident illumination. For stereolithography, the size of the incident illumination is given by the beam width of the laser. The incident energy dose is adjusted to control the depth of polymerization, so that it is matched to the layer thickness of the recoating mechanism. However, different compositions of ceramic suspensions cured with the same incident beam and dose will

not necessarily have the same cure depth and cure width. One ceramic suspension may cure much wider than another ceramic suspension, given the same beam width. A larger cure width hinders the ability to create fine features, similar to the limitations of a large laser beam width (section 3.1). As discussed in section 2.4, stereolithography parameters include the spacing between cured lines and the distance from the nominal edge of the part to the edge of the laser beam. Line broadening due to the composition of the suspension will affect these and other parameters. A suspension that has a large cure width may be able to use a larger line spacing than a suspension that has a narrow cure width. Determining relationships between composition, energy dose, cure depth, and cure width are important for improving the resolution of the process.

5.1.2 Predictions for Suspensions Without Powder

As discussed in Chapter 2, stereolithography laser beams are usually modeled as having Gaussian intensity distributions, characterized by the beam width (W_o) and peak intensity (I_{max}). The energy decreases logarithmically through the suspension, following the Beer-Lambert equation. The rate of change with distance is described by the resin sensitivity, S_d. The energy at any location within the suspension, E(y,z), is

$$E(y,z) = E_{max} \exp\left(\frac{-2y^2}{W_0^2}\right) \exp\left(\frac{-z}{S_d}\right) \qquad \text{Eq. 5.1}$$

where E_{max} is the energy dose at the center of the Gaussian beam, y is the horizontal distance from the center of the Gaussian beam, and z is the depth from the surface of the suspension. Curing occurs in the suspension wherever the energy dose is greater than or equal to the critical energy dose for polymerization (E_d). For the single-phase

commercial resins, the cure shape is well-defined for ideal laser beams. The cured profile is parabolic, with a maximum cure depth (C_d) of

$$C_d = S_d \ln\left(\frac{E_0}{E_d}\right) \qquad \text{Eq. 5.2}$$

where E_0 is the energy dose at the surface. The cured width at the surface, w_{Gauss}, is

$$w_{Gauss} = W_0\sqrt{2} \ln\left(\frac{E_{max}}{E_d}\right) \qquad \text{Eq. 5.3}$$

where E_{max} is the energy at the peak of the Gaussian distribution. Note that the surface line width for a Gaussian beam depends on energy dose, complicating the linewidth analysis. Increasing the energy dose increases the expected line width. A further difficulty arises because stereolithography lasers sometimes are multimodal and have complex non-Gaussian intensity profiles. For non-Gaussian beams, the excess line width cannot easily be separated from the beam width and it is not possible to directly measure broadening. The shape of the beam results in a cure width that is dependent on the energy dose.

An alternate method of characterizing the suspension is through a simple square wave beam. Ideally, collimated light could pass through a slit, providing an incident illumination distribution which is a square wave where $I(y) = I_o$ over a defined source width, which is the width of the slit. Due to diffraction effects, a perfectly square beam is not possible. However, it will be shown that the collimated slit apparatus can be used to provide a known intensity distribution.

5.1.3 Powder Suspensions

The resin sensitivity (S_d) has been shown in Chapter 2 to be due to the effects of the absorption coefficients of each of the individual components as well as the scattering off of the ceramic particles. Assuming the ceramic is UV transparent, the absorption model predicts the sensitivity of a suspension in terms of the scattering length, the concentrations of the components and their extinction coefficients as

$$\frac{1}{S_d} = \frac{1}{l_{Sc}} + (1-\Phi)(c_P\varepsilon_P + c_D\varepsilon_D) \qquad \text{Eq. 5.4}$$

where l_{sc} is the scattering length of the suspension, Φ is the volume fraction of ceramic powder in the suspension, c_P is the concentration of the photoinitiator, ε_P is the extinction coefficient of the photoinitiator, c_D is the concentration of the dye, and ε_D is the extinction coefficient of the dye.[1; 2] This chapter will focus on absorption-dominated suspensions, such as silica suspensions, which have small refractive index differences and are expected to have large scattering lengths. The absorption of the dye and photoinitiator are expected to be much larger than the scattering length for these suspensions. The relationship between sensitivity and the photoinitiator concentration and dye concentration will be investigated for cured lines. For suspensions without dye (c_D=0), it is predicted that the sensitivity will change with photoinitiator concentration as

$$\frac{1}{S_d} = \frac{1}{l_{Sc}} + \big((1-\Phi)\varepsilon_P\big)c_P \qquad \text{Eq. 5.5}$$

For suspensions varying the concentration of dye, the predicted behavior can alternatively be written as

$$\frac{1}{S_d} = \frac{1}{S_d(c_D=0)} + \big((1-\Phi)\varepsilon_D\big)c_D \qquad \text{Eq. 5.6}$$

where $S_d(c_D=0)$ is the resin sensitivity for the suspension without any absorbing dye. Note that

$$\frac{1}{S_d(c_D=0)} = \frac{1}{l_{sc}} + (1-\Phi)(c_P\varepsilon_P) \qquad \text{Eq. 5.7}$$

Eq. 5.6 predicts that the y-intercept of the reciprocal of resin sensitivity with respect to the concentration of dye is simply the resin sensitivity in the absence of dye, and the slope is $(1-\Phi)\varepsilon_D$. The resin sensitivity can be predicted provided that the extinction coefficients and scattering lengths are known.

Similar to the behavior of the resin sensitivity, the critical energy dose (E_d) can be predicted from the individual components in the suspension using the inhibitor exhaustion model. The inhibitors are exhausted at the critical energy dose which is dependent on the composition of the suspension as

$$E_d = (\gamma_{INH}c_{INH} + \gamma_D c_D)\frac{h\nu}{\Omega} \times \left[\frac{\frac{1}{l_{Sc}} + (1-\Phi)(c_P\varepsilon_P + c_D\varepsilon_D)}{c_P^2\varepsilon_P^2}\right] \qquad \text{Eq. 5.8}$$

where c_{INH} is the concentration of the inhibitors (such as oxygen or added quinones, etc), γ_{INH} is the number of radicals removed per inhibitor, γ_D is the number of radicals that were not generated due to the presence of the dye, h is Plank's constant, ν is the frequency of the light, and Ω is the number of free radicals given off per photon absorbed.[2; 3] Neglecting the higher order terms, this can be written as

$$E_d = (1-\Phi)\frac{h\nu}{\Omega}(\gamma_{INH}c_{INH} + \gamma_D c_D)\frac{1}{c_P\varepsilon_P} \qquad \text{Eq. 5.9}$$

Below this energy dose, the inhibitors absorb the free radicals that are generated, and no curing occurs. Above this energy dose, free radicals are available to cause propagation of the polymerization reaction and curing occurs. This predicts that the critical energy dose

will increase linearly with $1/c_P$, with the critical energy dose going to zero as the photoinitiator concentration goes to infinity ($1/c_P$ goes to zero). When the concentration of dye is increased, it is expected that the critical energy dose will increase linearly. For this case, the terms can be grouped as follows

$$E_d = E_d(c_D = 0) + (1 - \Phi)\frac{h\nu}{\Omega}(\gamma_D c_D)\frac{1}{c_P \varepsilon_P} \qquad \text{Eq. 5.10}$$

where $E_d(c_D=0)$ is the critical energy dose in the absence of dye. Note that

$$E_d(c_D = 0) = (1 - \Phi)\frac{h\nu}{\Omega}(\gamma_{INH} c_{INH})\frac{1}{c_P \varepsilon_P} \qquad \text{Eq. 5.11}$$

It can be seen from Eq. 5.10 that the rate of increase of the critical energy dose with the dye concentration is dependent on the volume fraction of the powder, the quantum efficiency, the number of free radicals that are prevented from forming due to the dye, the concentration of photoinitiator and the extinction coefficient of the photoinitiator.

These predictive models for sensitivity and critical energy dose are based on measurements of the cure depth at a variety of energy doses. However, they do not describe how the cure width changes with composition and dose. The focus of chapters 5 and 6 is to quantify the relationships between composition, energy dose, cure depth and cure width.

5.1.4 Broadening in Ceramic Suspensions

Limited work has previously been done using stereolithography to show how broadening changes with energy dose and composition. It has been shown that varying the particle concentration, size, and refractive index can change both the cured width and the cured depth in the suspension.[4-9] The concentration of UV absorber and

photoinitiator affect both the cure width and the cure depth at constant energy dose.[10; 11] Furthermore, the volume fraction of powders and the particle size will change the cure response for both the cure width and cure depth.[6; 7; 12] These observations are limited in that they are only measuring the width at two or three energy doses. They do not provide a comprehensive look at the relationship between the compositional factors and the changes that occur at a range of energy doses. Some reported on the process parameters, such as the illumination time or the drawing speed, which further limits the scope of which their results are useful. A more thorough understanding of the compositional factors is needed, so that these results can be applied broadly to photopolymerization processes.

The ceramic particles used in ceramic stereolithography significantly modify the polymerization process, due to the effects of light scattering. The effect of ceramic particles on the scattering process is related to their refractive index contrast,

$$\frac{\Delta n}{n_0} = \frac{n_{cer} - n_0}{n_0} \qquad \text{Eq. 5.12}$$

where n_{cer} is the refractive index of the ceramic particles and n_0 is the refractive index of the liquid medium. The scattering of light from ceramic particles can be approximated by the Mie model, incorporating a structure factor to account for the cross-interactions that arise for the high volume fraction of ceramic powders.[8] For suspensions that have a small contrast, the majority of the energy propagates in the forward direction. Only a small fraction of the energy is scattered to the side. Increasing the refractive index contrast (Δn) increases the portion of the energy that is scattered. The scattering behavior can be quantified by the scattering length, l_{sc}, which is the distance over which a photon must travel before its propagation direction becomes randomized. A large scattering

length corresponds to minimal scattering, while a small scattering length indicates a large degree of scattering.

It is expected that the scattering length in ceramic suspensions will be related to the shape of a cured line. A ceramic suspension with a large scattering length is expected to have a cured profile that is closer to that of an ideal resin. Hinczewski *et al*. have proposed a model for the linewidth of ceramic suspensions, suggesting that line width in ceramic suspensions can be predicted by modifying the equation for the linewidth of an ideal suspension (Eq. 5.3). Their model is given by the following equation:[13]

$$w = F_1\sqrt{2}\sqrt{\ln\left(\frac{E_0}{E_{Hincz.}}\right)} \qquad \text{Eq. 5.13}$$

where F_1 is the equivalent beam width and E_{Hincz} is the apparent critical energy dose. Note that E_{Hincz} is different than E_d. Essentially, F_1 and E_{Hincz} are fitting parameters which depend on the Gaussian beam width and materials parameters (refractive index, solids loadings, etc). For an ideal suspension, F_1 would be equal to one and E_{Hincz} would be equal to E_d. Chartier *et al*. showed that the model fit for three ceramic suspensions containing either alumina, zircon, or silica, with F_1 and E_{Hincz} decreasing with refractive index.[10] However, the major limitation of this model is that it is based on a Gaussian source. For higher mode lasers or for more uniform intensity distributions, this is no longer valid. The observed cure widths in the Chartier paper were up to 30 times larger than the beam width, such that the beam shape is less significant. Furthermore, the effects of composition on F_1 and E_{Hincz} were not quantified, to allow for predictions in the curing behavior of the suspensions. For these reasons, a model is needed which is independent of the light source used and which also can be used to summarize the compositional effects.

5.1.5 Proposed Model: Quasi-Beer-Lambert Broadening

For ceramic suspensions that exhibit broadening, a model is needed to describe their behavior. The width of a cured line can be broken into two components: the width of the source and then the excess width on either side of the light source width. In the absence of broadening, the cured width is simply equal to the width of the energy distribution that is above the critical energy dose of the suspension. For a stereolithography beam, this width will be highly dependent on the energy dose. In contrast, the cured width from a collimated slit will only have a slight dependence on energy for ideal suspensions. The excess width for ideal suspensions is equal to zero.

It will be shown that the broadening behavior of individual cured lines of ceramic suspension can be quantified through analysis of the quasi-Beer-Lambert behavior of the excess width and the cure depth. As shown in Chapter 2 for traditional suspensions, the cure depth, is given by Beer-Lambert behavior:

$$C_d = S_d \ln\left(\frac{E_0}{E_d}\right) \qquad \text{Eq. 5.14}$$

where E_0 is the incident energy dose, S_d is the sensitivity in the depth direction (with units of length), and E_d is the critical energy dose in the depth direction. The cure width (w) can be separated into the width due to the illumination width (w_{beam}) and the excess width (w_{ex}) due to broadening in the ceramic suspension, where

$$w_{ex} = \frac{w - w_{beam}}{2} \qquad \text{Eq. 5.15}$$

For an apparatus with a Gaussian lightsource, w_{beam} is equal to w_{Gauss} (see Eq. 5.3); w_{beam} is equal to the slit width for the collimated slit apparatus. Experiments presented here fit

the excess width (w_{ex}) to a similar expression as the cure depth, using quasi-Beer-Lambert behavior:

$$w_{ex} = S_w \ln\left(\frac{E_0}{E_w}\right) \qquad \text{Eq. 5.16}$$

where S_w is the resin sensitivity in the horizontal direction (units of length) and E_w is the apparent critical energy dose in the width direction. The width sensitivity (S_w) is analogous to the depth sensitivity (S_d), and the width critical energy dose (E_w) is analogous to the depth critical energy dose (E_d). This is called quasi-Beer-Lambert because the energy attenuates similar to the Beer-Lambert equation, even though the incident light is not in the horizontal direction. This behavior arises because a portion of incident light is scattered to the sides. The suspension remains a Beer-Lambert absorber, so it follows that the broadening behavior would also fit a semilogarithmic model.

It is important to note that the measured parameters (sensitivity and critical energy dose) are direction dependent. The width parameters are often different than the depth parameters of the suspension. It is expected that the broadening parameters (S_w, E_w) are affected by both the scattering of light off of the ceramic particles as well as the absorption and critical energy dose of the monomer solution. The scattering is affected by the refractive index difference between the ceramic powder and monomer, the solids loading of the ceramic suspensions, and the particle size distribution. The absorption and critical energy dose of the monomer solution are affected by the concentrations of the photoinitiator and the ultraviolet-absorbing dye. The depth parameters are also slightly changed since some of the energy that was contributing to the reaction in the forward direction has now been redirected to the side. A key aspect of this chapter will be to

quantify the relationship between the depth and width values, and see if the width constants follow the same trends as the depth constants as composition is varied.

Practically, it is important to limit the amount of broadening when curing ceramic suspensions. This can be done through several ways: decreasing the width sensitivity so that the excess broadening is kept as small as possible or increasing the width critical energy dose so that it is larger than the incident energy dose. These conditions may be achieved by tuning the composition of the ceramic suspension, as described in chapters 5 and 6. The ideal ceramic suspension would allow for a large range of cure depths without any broadening. This can be described by the broadening depth (D_b), which is the depth of cure at the onset of broadening (C_d=D_b when E_0=E_w). In terms of the suspension parameters,

$$D_b = S_d \ln\left(\frac{E_w}{E_d}\right) \qquad \text{Eq. 5.17}$$

It can be seen that the broadening depth is greater for large depth sensitivities and width critical energy doses and small depth critical energy doses. Note that the composition of the suspension is typically designed for the best depth critical energy dose (E_d) and depth sensitivity (S_d) for the illumination system. Thus it will be important to consider the broadening and light source together. A large value for D_b indicates that a suspension can be cured deeper before beginning to broaden, while a small D_b indicates that broadening will occur at a shallower cure depth with broadening. This has a practical consequence, since deep and narrow features cannot be cured using suspensions with a small broadening depth.

5.2 Experimental Procedure

5.2.1 Materials

Photopolymerization experiments were performed on a commercial stereolithography resin as well as formulated ceramic suspensions. The commercial stereolithography resin used was Somos 8110 (DSM Somos). Formulated for He-Cd laser systems, Somos 8110 has a depth critical energy dose of 6.0 mJ/cm^2 and a depth sensitivity of 135 μm, measured at a wavelength of 325 nm.

Photopolymerizable ceramic suspensions were prepared for a variety of compositions. Silica (SiO_2) powders (Tecosphere-A, CE Minerals, density=2.2 g/cm^3, n_D=1.4603, d_{50}=4.64 μm) were used at a 60 vol% solids loading. The suspensions contained 4.17 ml of dispersant (Variquat CC-59, Evonik, 1.1 g/cm^3) for each 100 ml of powder, for a dispersant addition of 2.08 wt% on the basis of the silica powder. For each liter of total liquids, the silica suspensions contained 0.046-0.18 mol of a ketone photoinitiator (Irgacure 184, Ciba, molecular weight=204.3 g/mol) with no dye or 0.092 mol of photoinitiator and 0-0.00283 mol of an inert triazole dye (Tinuvin 171, Ciba, molecular weight=395 g/mol). The extinction coefficient of the photoinitiator is 20 L/mol-cm at a wavelength of 365 nm and the extinction coefficient of the dye is 8680 L/mol-cm at a wavelength of 365 nm.[1] The remainder was the monomer, 1,6 hexanediol diacrylate (SR238B, Sartomer, Exton, PA, molecular weight of 226 g/mol). The suspension medium had a density of 1.020 g/cm^3 and a refractive index of 1.4560. Suspensions were allowed to homogenize by rolling on a ball mill without milling media for 24 hours.

5.2.2 Method

A collimated slit apparatus (Figure 5.1) was constructed to standardize the distances when performing experiments and to ensure a well-defined beam shape of the incident light. Additionally, this has the advantage that the suspension is illuminated from below, through a glass coverslip, eliminating the potential of variable oxygen inhibition on the surface of the suspension. A small amount of suspension is placed in a rubber o-ring sitting on a glass coverslip, which serves as the vessel to hold the suspension. The suspension is illuminated from the bottom by collimated light (High Power LED Collimator Source, Mightex Systems) with a wavelength of 365 nm and angular divergence of 1.7°. The collimated light is passed through a slit 200 μm wide by 3 mm long (National Aperture).

The incident intensity distribution is given by Figure 5.2, as determined using a CMOS sensor (OV7670, Omnivision) with pixel size 3.6 μm x 3.6 μm. The measured intensity distribution is in agreement with the expected width, assuming a 200 μm slit. An analysis of the Fresnel diffraction through the slit does not account for the broadening in the intensity beyond the 200 μm slit width. Rather, there is an additional 23 μm divergence width on either side of the slit corresponding to the 1.7° divergence of the light source over the distance of the optical slit holder and coverslip. The total illumination width is 246 μm. Energy dose was adjusted by changing the illumination times at constant intensity, using the Mightex driver software. Energy was calibrated using a UV radiometer (UV Integrator PC-2008, Hanovia).

A sample of suspension was illuminated using the collimated slit apparatus, resulting in a 3 mm long cured line that had adhered to the glass coverslip. The coverslip

and cured line were rinsed with isopropanol, and then allowed to dry. Micrographs of the cross-section of the cured lines were taken with a stereomicroscope (SMZ 1000, Nikon) with a camera (Go-3, QImaging). Cure width and depth were measured using ImageJ (NIH), with the cure width defined as the width at the top (depth of z=0).

5.3 Results and Discussion

5.3.1 Commercial Resin

To validate the experimental setup, linewidth samples were measured for the commercial stereolithography resin at several energy doses. Micrographs were taken of the long, narrow profile, and points were selected on this to define the outline of the cured profile. Two of these outlines are shown in Figure 5.3, for energy doses of 6.75 mJ/cm^2 (A) and 27.0 mJ/cm^2 (B). Note that the samples are not cut, as this would damage the shape. Rather, images are captured when the outer edge is in focus in the microscope. There was a 23% increase in width of the cured profile between the two energy doses, while there was a 140% increase in depth. The depth of the cured profile increases with the logarithm of energy (Figure 5.4), as predicted for a Beer-Lambert absorber. The depth sensitivity (S_d) was found to be 727±53 μm. The depth critical energy dose (E_d) of the resin was found to be 2.36 mJ/cm^2 with one standard deviation of the lognormal distribution falling within an error range of 1.96-2.84 mJ/cm^2. Note that the sensitivity and critical energy dose provided by the manufacturer assume a light source with a wavelength of 325 nm, in contrast to the 365 nm light source used in the collimated slit apparatus. The absorption of the photoactive species is highly dependent on the wavelength of the light source, so these measured values cannot be directly

compared. For instance, the photoinitiator Irgacure 184 has an extinction coefficient of 20 L/mol-cm at a wavelength of 365 nm, but this increases to 49 L/mol-cm at a wavelength of 355 nm.[1] This is an increase of almost 2.5 times, over 10 nm of wavelength. The properties of the Somos resin are not available at 365 nm, so a direct comparison is not possible. However, Figure 5.4 shows that the cure response for the collimated slit apparatus is Beer-Lambert, with no anomalies noted.

The cured profile was compared to the predicted profile for the energy distribution. Figure 5.5 contains a comparison of the observed cure shape and the predicted cure shape at energy doses of 6.75 mJ/cm^2 (A) and 27.0 mJ/cm^2 (B). The predicted cure shape was calculated assuming the incident energy dose had the energy distribution of the collimate slit apparatus (Figure 5.2) and the resin is a Beer-Lambert suspension with S_d of 727 μm and E_d of 2.36 mJ/cm^2. The observed behavior was consistent with the expected behavior for non-scattering Beer-Lambert suspensions for both of the energy doses. Most importantly, the broadening was negligible. The cure width varied between 200 μm and 240 μm, while the cure depths varied from 800 μm to 1800 μm. It was confirmed that the collimated slit apparatus is a valid technique for determining the cure properties for photopolymerizable suspensions.

5.3.2 Cured Profile in Ceramic Suspensions

In contrast to the narrow cure profiles seen for the commercial unfilled resins, ceramic suspensions can exhibit large amounts of broadening. Figure 5.6 shows the broadening profiles of a ceramic suspension containing 60 vol% silica and 0.092 mol/L photoinitiator, along with the width of the incident illumination. At an energy dose of 54

mJ/cm^2 (E_1), the cured profile was 390 μm wide at the surface and 850 μm deep. The cured profile has ballooned out, with the largest broadening occurring below the surface of the suspension. When the energy dose was increased to 135 mJ/cm^2 (E_2), the width became uniform between the cured region at the surface and below the surface of the suspension. At this dose, the cure width was 1050 μm and the cure depth was 1020 μm. Increasing the energy dose to 203 mJ/cm^2 (E_3) and 405 mJ/cm^2 (E_4) caused continued broadening. The suspension cured to 1740 μm wide and 1200 μm deep at an energy dose of 203 mJ/cm^2 and 2950 μm wide and 1490 μm deep at an energy dose of 405 mJ/cm^2. Increasing the energy dose has resulted in a cured profile that is much broader with only a moderate increase in the cure depth.

As mentioned above, at some intermediate energy doses the profiles were observed to balloon out, as demonstrated at an energy dose of 54 mJ/cm^2 in Figure 5.6. This balloon shape is characterized by a neck of cured material at the surface of the suspension, with the maximum cured width occurring near the middle of the cure depth. This is likely due to the Mie scattering of the ceramic particles, especially for suspensions containing silica. The refractive index of the monomer (n=1.4560) is closely matched to that of silica (n=1.4603), so much of the light is scattered in the forward direction. The light must travel a large distance in the silica suspensions before its direction becomes randomized. At high energy doses, the light undergoes many scattering events before the energy falls below the critical energy dose, so the effects of the forward scattering are not apparent. Scattering that is primarily in the forward direction can lead to balloon-shaped cured profiles at intermediate doses, as will be shown in more detail in section 6.5.

5.3.3 Quasi-Beer-Lambert Broadening Behavior

The changing size of the cured profile can be described by the semilogarithmic behavior for both the cure depth and excess width, as seen in Figure 5.7. The excess width (w_{ex}) is defined as the additional surface broadening in the suspension, as illustrated in Figure 5.6. The excess width is omitted for samples that are less than 600 μm wide (3 times larger than the slit width), since these narrow samples are affected by the precise illumination distribution as well as ballooning effects. This cut-off provides a means of differentiating between broadening of the distribution versus broadening due to the ceramic suspension. Note that the slopes (S_d/S_w) and dose intercepts (E_d/E_w) for the cure depth and excess width are different. The depth sensitivity is 306±35 μm whereas the width sensitivity is 876±33 μm. The depth critical energy dose is 4.1 mJ/cm^2 with an error range of 2.3-7.4 mJ/cm^2, while the width critical energy dose is 90 mJ/cm^2 with an error range of 79-102 mJ/cm^2. For this composition, the broadening depth, as defined by Eq. 5.17, was 940±140 μm. The depth dependence on energy dose was found to increase linearly with the logarithm of the energy dose, as expected for Beer-Lambert behavior, The linear relation between the width and the logarithm of the energy dose is referred to as quasi-Beer-Lambert behavior.

When these suspensions are used for ceramic stereolithography, the energy dose will be set to cure to a desired depth. Each stereolithography system will have a different preferred range of energies that can be used, depending on the laser intensity and speed of the drawing mechanism. As calculated in section 3.4, a small resin depth sensitivity is usually desired to prevent large variations in cure depth with energy fluctuations. However, the width parameters will also need to be accounted for when designing

ceramic suspensions. It is important to understand the width and depth parameters for the given system to be used.

5.3.4 Effect of Photoinitiator Concentration

Cure width and depth were measured as a function of energy dose for silica suspensions containing 0.046-0.18 mol/L photoinitiator with no UV absorber. As predicted by Eq. 5.5, the reciprocal of the sensitivity should increase linearly with concentration of photoinitiator. The slope of the best fit line is expected to be simply equal to the volume fraction liquids (1-Φ) multiplied by the extinction coefficient (ε), or (1-Φ)ε. The y-intercept of the line for the suspensions varying photoinitiator predicts the scattering length of the ceramic suspension. It can be seen (Figure 5.8) that the reciprocal of the width sensitivity and the reciprocal of the depth sensitivity are both linear with concentration of photoinitiator, as predicted by the absorption model. Fitting the sensitivities to a linear equation allows the extinction coefficients to be determined for the suspension, as given by Eq. 5.5. The measured extinction coefficients and scattering lengths for the absorption model are given in Table 5.1, along with the literature value of the extinction coefficient for comparison. The measured extinction coefficients are 2 to 13 times larger than the literature value of 0.0020 L/μm-mol. The extinction coefficient from the depth sensitivity is 0.0265 L/μm-mol and the extinction coefficient from the width sensitivity is 0.0043. These differences can be attributed to the path length effects, which will be discussed in more detail in Chapter 6. The scattering lengths were 410 μm for the width direction and 1040 μm for the depth direction. The source of this discrepancy is not known. The physics of the absorption model predict that the scattering

length and extinction coefficient will be the same in both the depth and width directions, but this was not observed.

The effect of photoinitiator concentration on the critical energy doses was also measured for these ceramic suspensions. From the inhibitor exhaustion model (Eq. 5.9), the critical energy dose is expected to increase linearly with the inverse of the concentration of photoinitiator, with the critical energy dose going to infinity in the absence of photoinitiator. It was found that both the depth critical energy dose (Figure 5.9A) and width critical energy dose (Figure 5.9B) increase linearly with the reciprocal of photoinitiator concentration. Thus, these results are consistent with the predicted behavior of the inhibitor exhaustion model. However, it is important to note that the width critical energy doses are more than an order of magnitude larger than the comparable depth critical energy doses. This large difference is likely due to the small scattering angles in the nearly index-matched silica suspensions ($\Delta n=0.0043$). Increasing the energy dose effectively increases the path length travelled by the photons, so they can begin propagating sideways. Below the width critical energy dose, there is expected to be some scattering to the side, but its effect is minimal. The large width critical energy doses are advantageous for ceramic stereolithography and other photopolymerization systems, because a significant portion of depth can be cured prior to the broadening depth.

It was found that changing the concentration of the photoinitiator has no effect on the broadening depth (Figure 5.10). This is surprising, as there was a clear dependence of the width and depth parameters on the concentration of photoinitiator. The reciprocal sensitivities both increased with concentration of photoinitiator (Figure 5.8), as did the

critical energy doses (Figure 5.9). However, the uniform broadening depths indicate that these changes offset each other. This is a beneficial finding, because it allows the concentration of photoinitiator to be tailored to the incident energy source without contributing to broadening. For instance, concentration of photoinitiator can be increased to ensure that polymerization occurs rapidly, increasing the efficiency of the process. This change will not affect the broadening of the ceramic suspension.

5.3.5 Effect of Dye Concentration

The effect of dye concentration on the photocuring properties of the suspension was also determined. The resin sensitivity was measured as a function of the dye concentration as shown in Figure 5.11. The silica suspensions contained 60 vol% powder and 0.092 mol/L photoinitiator, with 0-0.00283 mol/L dye. The dye acts by absorbing photons that are propagating through the suspension, so that they cannot penetrate deeper or participate in the curing reaction. Note that the extinction coefficient of the dye is high (0.868 L/mol-μm), so only small concentrations (on the order of mmol/L) are required to change the curing properties of the suspensions. The absorption model (as given by Eq. 5.6) predicts that the reciprocal of the sensitivity should increase linearly with concentration of concentration of dye, when the photoinitiator concentration is held constant. This linear behavior was observed for both the width sensitivity and the depth sensitivity. The linear fitting parameters for Eq. 5.6 (the y-intercept of $1/S(c_P=0.092$ mol/L, $c_D=0)$ and ε_D) are given in Table 5.2, along with the dye extinction coefficient from Tomeckova *et al*. Furthermore, the absorption model predicts that the y-intercept of Figure 5.11 of the reciprocal of resin sensitivity is simply the resin sensitivity in the

absence of dye. Although this point is an experimental point for a given composition (without dye), it is notable that the sensitivities of suspensions with dye (*i.e.*, $c_D > 0$) also extrapolate to this value. This was consistent for both the width and depth parameters. Finally, the absorption model predicts that the slopes in Figure 5.11 are equal to $(1 - \Phi)\varepsilon_D$. The literature value of the dye extinction coefficient is 0.868 L/μm-mol,[1] whereas the measured depth extinction coefficient is 4.72 L/μm-mol and the measured width extinction coefficient is 2.04 L/μm-mol. The measured depth and width extinction coefficients were 5.4 and 2.4 times larger, respectively, than the predicted extinction coefficient, indicating that the energy is attenuating more rapidly than expected. Similar to the photoinitiator, the extinction coefficient from the depth direction was larger than the extinction coefficient from the width direction, and both were larger than the literature values. Again the source of this discrepancy can be attributed to the path length effects of scattering, which is investigated further in Chapter 6.

The effect of the dye concentration on the critical energy dose was also determined. As shown in Figure 5.12A, increasing the concentration of the dye had little effect on the depth critical energy dose. The width critical energy dose (Figure 5.12B) increased strongly with the concentration of the dye in the composition. Similar to the effect of photoinitiator concentration, the critical energy dose is over an order magnitude larger in the width direction than in the depth direction. Again, this discrepancy is attributed to the small Mie scattering angles in the silica suspensions.

The effect of the dye concentration on the broadening depth was also determined (Figure 5.13). It was found that the broadening depth decreased with the concentration of dye in the system. The suspension without dye had a broadening depth of 940±140μm,

while the suspension with 0.00283 mol/L of dye had a broadening depth of 480±60μm. For applications with cure depths of 100-200 μm, there will be no broadening for any of these suspensions. However, if deeper curing is required, then the broadening depth must be accounted for. Additionally, these results suggest that it is important to account for the effect of the concentration of dye on the broadening depth, to ensure that optimal resolution is attained.

5.4 Conclusions

Broadening in ceramic suspensions and the compositional and energy dose dependence must be known. The collimated slit apparatus was verified as a method of producing controlled polymerization in photosensitive resins. This apparatus was used to determine the cured depth and width of photopolymerizable ceramic suspensions at different energy doses. As expected for Beer-Lambert absorbers, the cure depth increases with the logarithm of energy, and can be characterized by the depth critical energy dose, E_d, and the depth sensitivity, S_d. The cure width can be quantified by the excess width, which is the additional broadening width that occurs for ceramic suspensions. It was found that this excess width, w_{ex}, exhibits a quasi-Beer-Lambert behavior, with excess width related to energy dose by

$$w_{ex} = S_w \ln\left(\frac{E_0}{E_w}\right) \qquad \text{Eq. 5.18}$$

where E_0 is the incident energy dose, E_w is the width critical energy dose, and S_w is the width sensitivity. It was unexpected that the excess width would have a quasi-Beer-Lambert behavior, as the Beer-Lambert equation describes the attenuation of light in the direction of propagation. It was discovered that the depth at broadening (D_b) is an

additional parameter that can be used to describe the broadening of ceramic suspensions. This is defined as the cure depth at which the incident energy dose is equal to the width critical energy dose. In terms of suspension parameters, D_b is given by

$$D_b = S_d \ln\left(\frac{E_w}{E_d}\right) \qquad \text{Eq. 5.19}$$

If D_b is less than the layer thickness, then it is expected that broadening will not be significant for that composition. The width and the depth parameters must both be accounted for when optimizing suspensions for ceramic stereolithography.

The effects of concentration of photoinitiator and concentration of an ultraviolet-absorbing dye were also measured and compared to the absorption and inhibitor exhaustion models. The reciprocals of the width and the depth sensitivities increased linearly with the concentration of the photoactive species, as predicted by the absorption model. The photoinitiator extinction coefficient was larger when measured in the depth direction than in the width direction, and both were larger than the literature value. Similarly, the dye extinction coefficient was larger when measured in the depth direction than in the width direction, and both were larger than expected from literature. Additionally, the width critical energy dose and depth critical energy dose exhibited the behavior predicted by the inhibitor exhaustion model. It was found that increasing the reciprocal of the photoinitiator concentration increased the critical energy dose of the suspension. Increasing $1/c_D$ did not significantly change the depth critical energy dose, but did increase the width critical energy dose.

The change in the broadening depth with concentration of photoinitiator and dye was also determined. When the amount of photoinitiator was varied, it was found that the changes in the width and depth parameters offset each other and the broadening depth

did not change. However, the dye concentration does affect the broadening depth, with increasing dye concentration corresponding to decreasing broadening depth. This chapter focused on quantifying the relationship between cure depth and cure width in absorption-dominated suspensions. This allows for improved formulation of suspensions for ceramic stereolithography.

5.5 References

[1] V. Tomeckova and J. W. Halloran, "Cure depth for photopolymerization of ceramic suspensions," *Journal of the European Ceramic Society,* **30**[15] 3023-33 (2010).

[2] V. Tomeckova and J. W. Halloran, "Predictive models for the photopolymerization of ceramic suspensions," *Journal of the European Ceramic Society,* **30**[14] 2833-40 (2010).

[3] V. Tomeckova and J. W. Halloran, "Critical energy for photopolymerization of ceramic suspensions in acrylate monomers," *Journal of the European Ceramic Society,* **30**[16] 3273-82 (2010).

[4] M. L. Griffith and J. W. Halloran, "Freeform fabrication of ceramics via stereolithography," *Journal of the American Ceramic Society,* **79**[10] 2601-08 (1996).

[5] C. Sun and X. Zhang, "The influences of the material properties on ceramic micro-stereolithography," *Sensors and Actuators a-Physical,* **101**[3] 364-70 (2002).

[6] W. Zhou, D. Li, and Z. Chen, "The influence of ingredients of silica suspensions and laser exposure on UV curing behavior of aqueous ceramic suspensions in stereolithography," *The International Journal of Advanced Manufacturing Technology,* **52**[5] 575-82 (2011).

[7] T. Chartier, A. Badev, Y. Abouliatim, P. Lebaudy, and L. Lecamp, "Stereolithography process: Influence of the rheology of silica suspensions and of the medium on polymerization kinetics – Cured depth and width," *Journal of the European Ceramic Society*[0] (2012).

[8] K. C. Wu, K. F. Seefeldt, M. J. Solomon, and J. W. Halloran, "Prediction of ceramic stereolithography resin sensitivity from theory and measurement of diffusive photon transport," *Journal of Applied Physics,* **98**[2] (2005).

[9] M. L. Griffith and J. W. Halloran, "Scattering of ultraviolet radiation in turbid suspensions," *Journal of Applied Physics,* **81** 2538 (1997).

[10] T. Chartier, C. Chaput, F. Doreau, and M. Loiseau, "Stereolithography of structural complex ceramic parts," *Journal of Materials Science,* **37**[15] 3141-47 (2002).

[11] C. Sun and X. Zhang, "Experimental and numerical investigations on microstereolithography of ceramics," *Journal of Applied Physics,* **92**[8] 4796-802 (2002).

[12] Y. Abouliatim, T. Chartier, P. Abelard, C. Chaput, and C. Delage, "Optical characterization of stereolithography alumina suspensions using the Kubelka–Munk model," *Journal of the European Ceramic Society,* **29**[5] 919-24 (2009).
[13] C. Hinczewski, S. Corbel, and T. Chartier, "Ceramic suspensions suitable for stereolithography," *Journal of the European Ceramic Society,* **18**[6] 583-90 (1998).

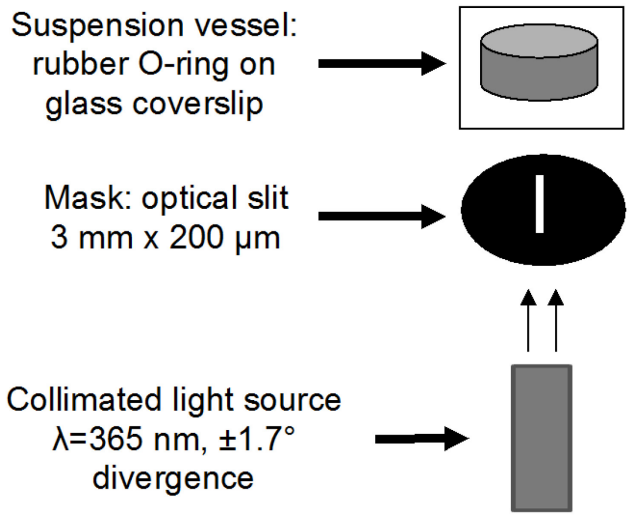

Figure 5.1 Schematic of apparatus used for controlled photopolymerization. A 365 nm collimated light source is used to pass light through an optical slit (width=200 µm, length=3 mm) onto suspension that is contained by a rubber O-ring sitting on a glass cover slip.

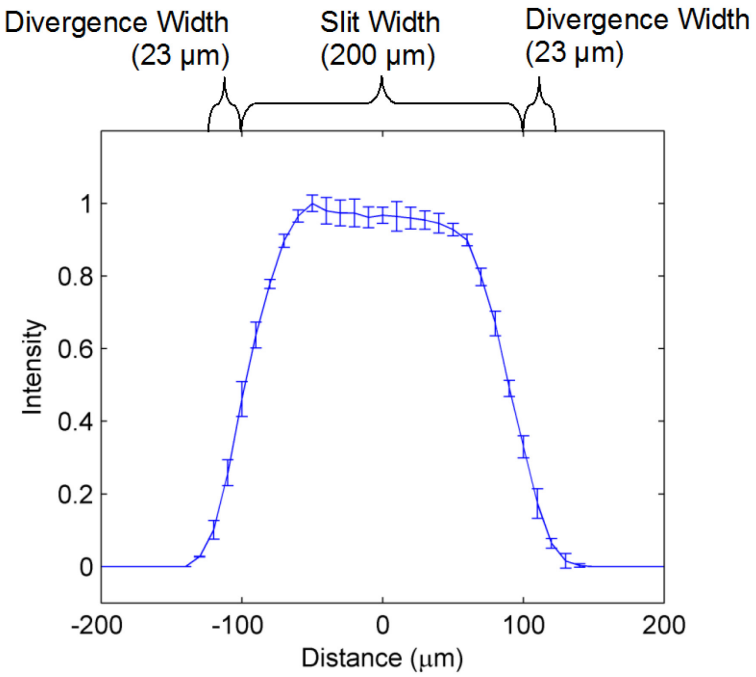

Figure 5.2 Normalized intensity of light at suspension surface. Note that the 1.7° degree divergence of the light source results in an additional 23 µm divergence width on either side of the slit width.

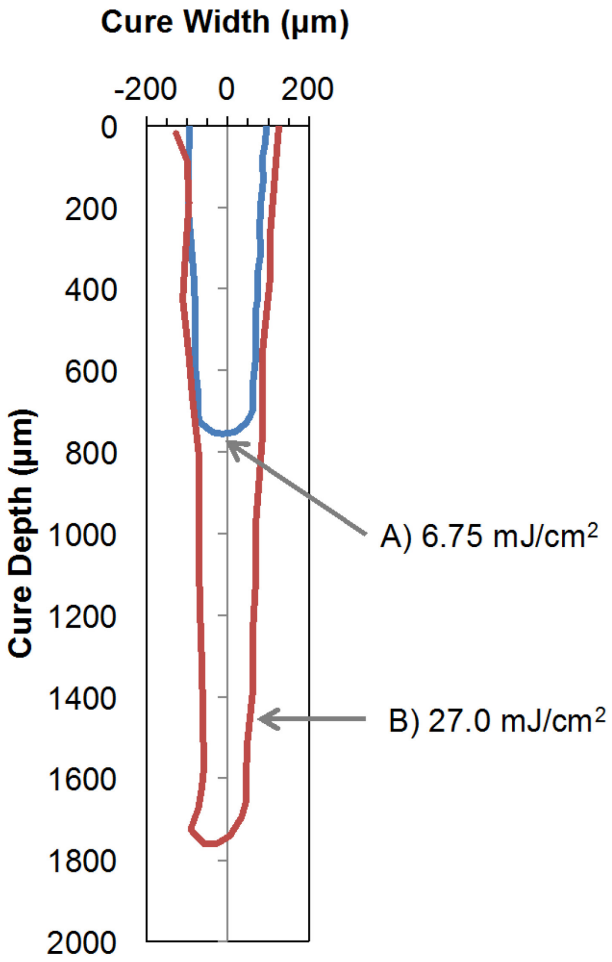

Figure 5.3 Cross section of cured line for commercial stereolithography resin at energy doses of 6.75 mJ/cm^2 (A) and 27.0 mJ/cm^2 (B).

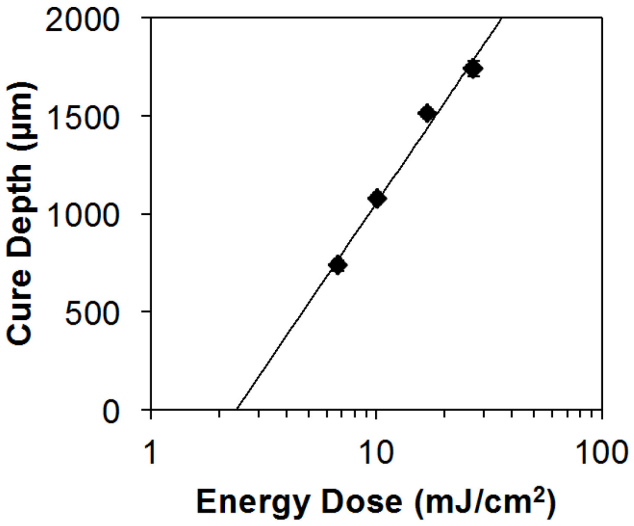

Figure 5.4 Cure depth as a function of energy dose for the commercial stereolithography resin.

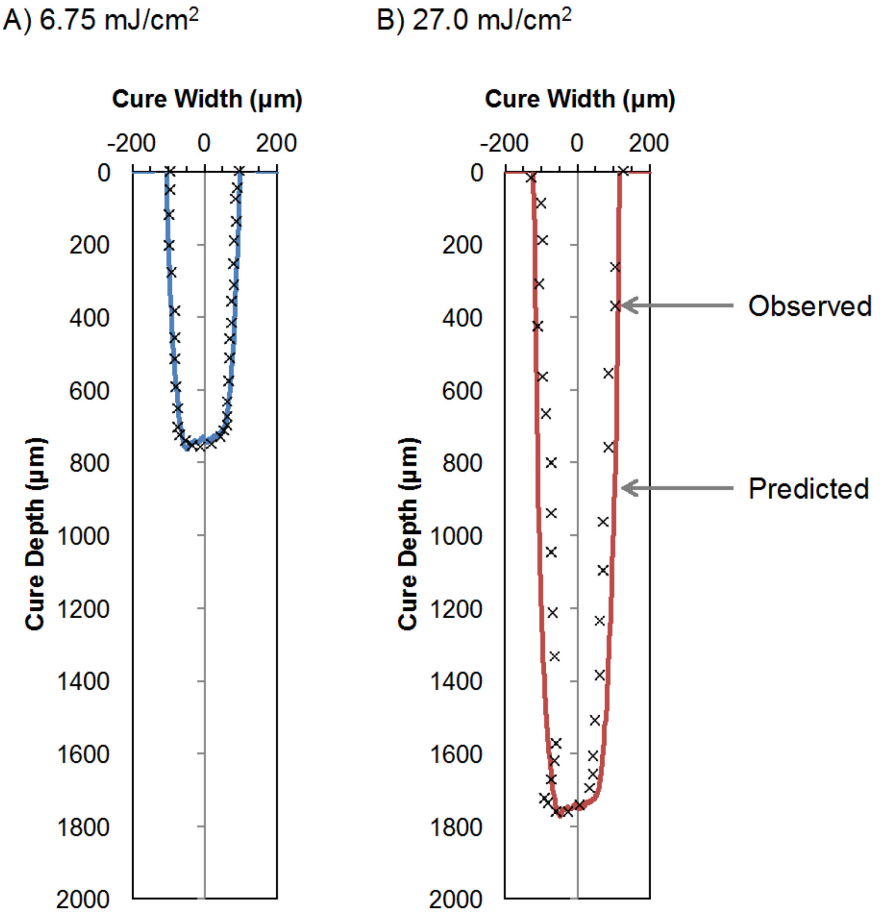

Figure 5.5 Predicted cure shape (solid line) and observed cure shape (x) for commercial resin at energy doses of 6.75 mJ/cm^2 and 27.0 mJ/cm^2. The predicted shape was calculated assuming a resin with an intensity distribution given by Figure 5.2, using S_d=727 µm and E_d=2.36 mJ/cm^2.

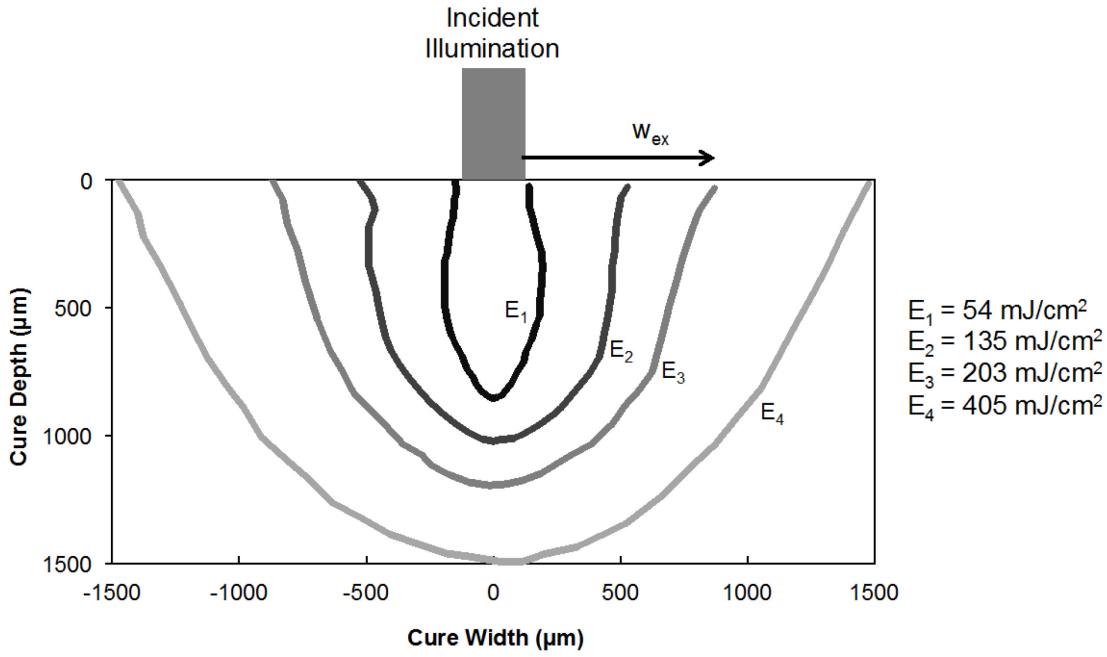

Figure 5.6 Cross-sections of linewidth samples containing 60 vol% silica powder and 0.092 mol/L photoinitiator in HDDA. The incident illumination width for all samples was 246 µm. A schematic of the cure profile is shown for energy doses of 54 mJ/cm^2, 135 mJ/cm^2, 203 mJ/cm^2, and 405 mJ/cm^2.

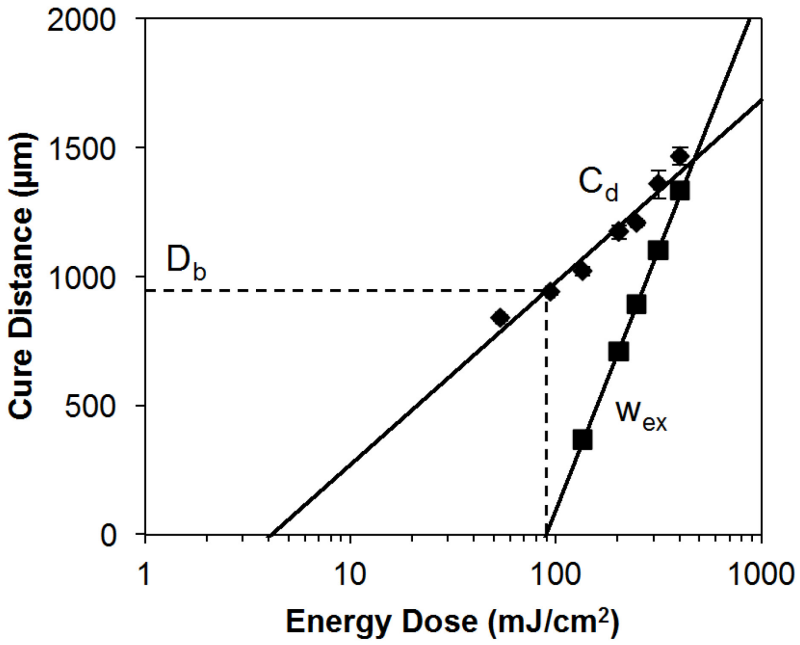

Figure 5.7 Cure depth (C_d) and excess width (w_{ex}) versus energy dose for a silica suspension containing 60 vol% SiO_2 and 0.092 mol/L photoinitiator in HDDA. Note that the broadening depth (D_b) is also indicated. This is the depth at which the energy dose is equal to the critical energy dose for broadening, as indicated by the dashed lines.

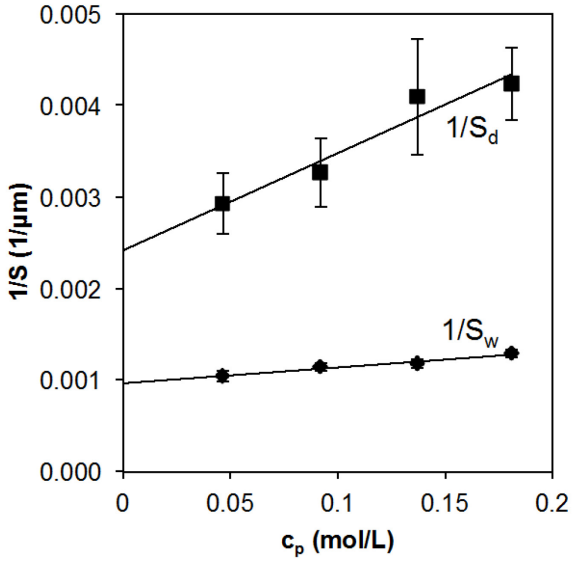

Figure 5.8 Depth sensitivity (S_d) and width sensitivity (S_w) as a function of photoinitiator concentration for 60 vol% silica. Note that the reciprocals are plotted for comparison to the absorption model.

Table 5.1 Fitting constants from the absorption model for photoinitiator extinction coefficient.

	l_{sc} (μm)	ε_P (L/μm-mol)
From Tomeckova *et al.* [1]		0.0020
Measured Depth Sensitivity	410	0.0265
Measured Width Sensitivity	1040	0.0043

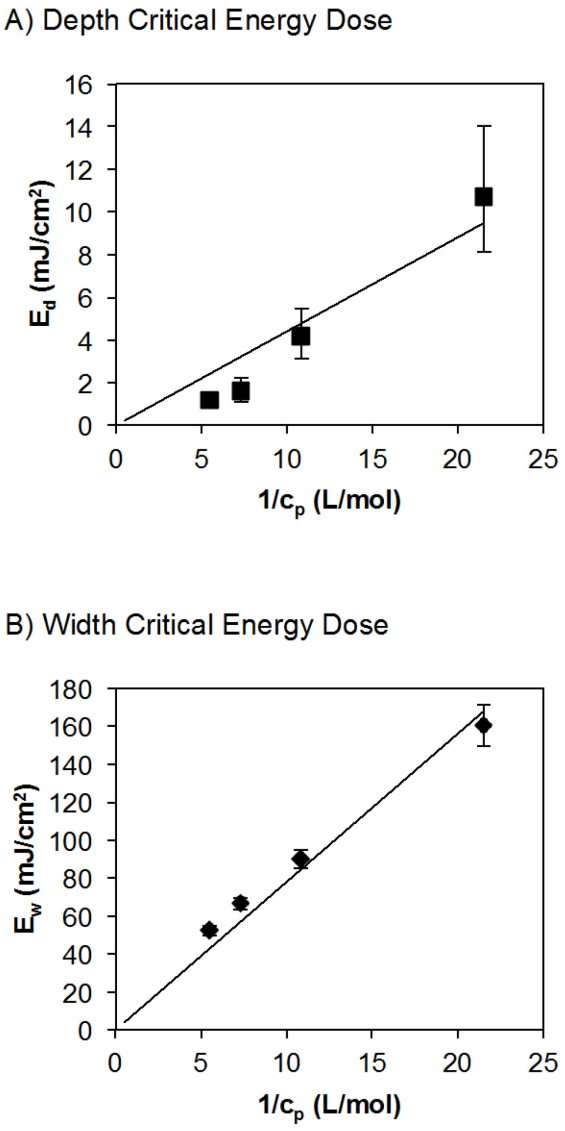

Figure 5.9 Effect of concentration of photoinitiator on the depth critical energy dose (A) and width critical energy dose (B).

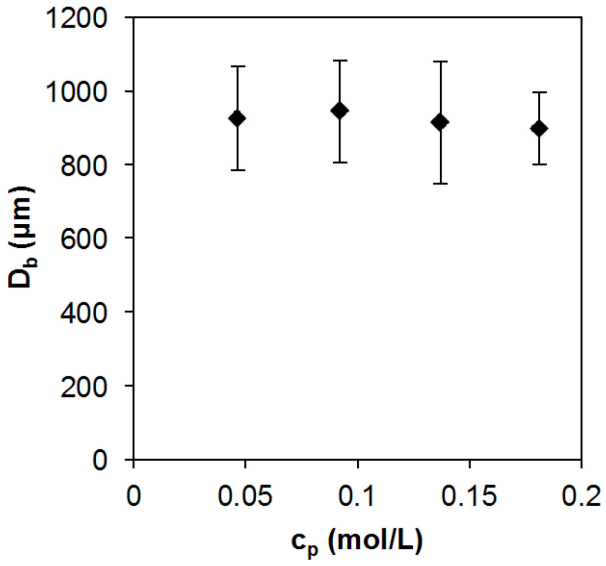

Figure 5.10 Effect of photoinitiator concentration on the broadening depth.

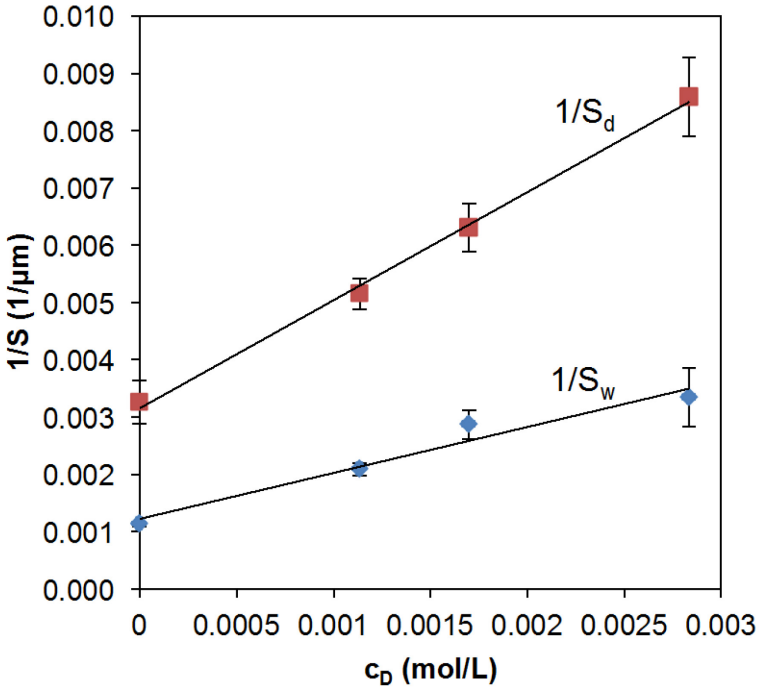

Figure 5.11 Depth sensitivity (S_d) and width sensitivity (S_w) as a function of dye concentration. Note that the reciprocals (1/S) are plotted for comparison to the absorption model.

Table 5.2 Fitting constants for absorption model as the concentration of dye is varied.

	$1/S(c_P=0.092$ mol/L, $c_D=0)$ (1/μm)	ε_D (L/μm-mol)
From Tomeckova *et al.* [1]		0.868
Measured Depth Sensitivity	0.00316	4.72
Measured Width Sensitivity	0.00123	2.04

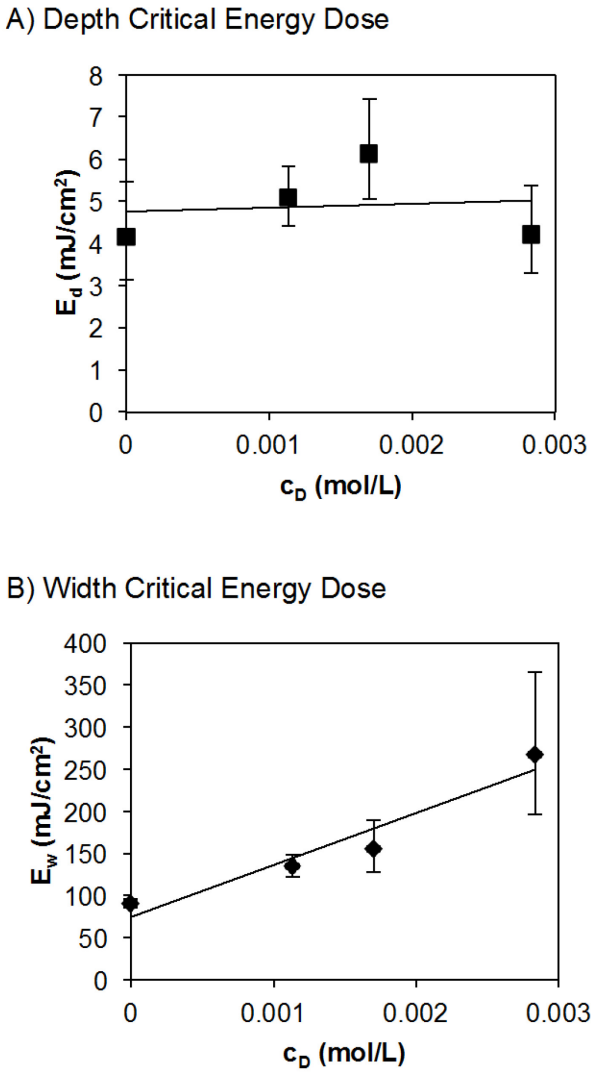

Figure 5.12 Effect of concentration of dye on the critical energy dose of the ceramic suspensions for both the depth (A) and width (B).

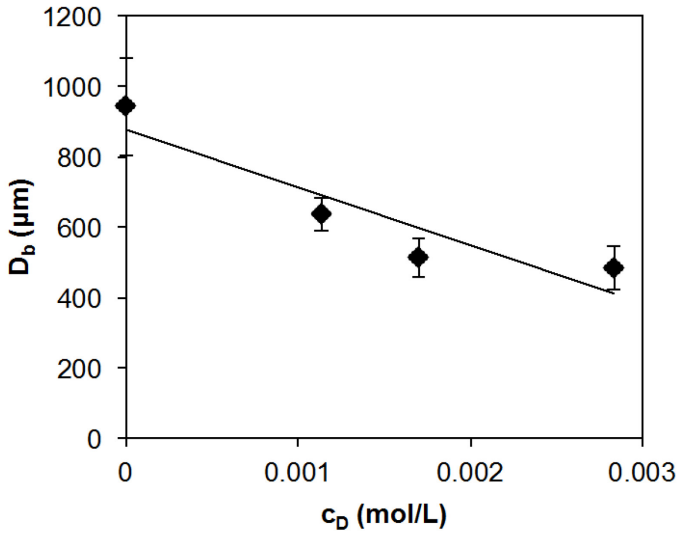

Figure 5.13 Change in broadening depth as a function of the dye concentration for silica suspensions containing 0.092 mol/L photoinitiator.

Chapter 6

Linewidth in Scattering-Dominated Suspensions

6.1 Introduction

The scattering of light within the ceramic suspension is very important to the resolution of ceramic photopolymerization processes, and is the focus of this chapter. As discussed in Chapter 5, the cross-sectional shape of a cured line of suspension is dependent on the composition of the suspension. The Beer-Lambert cure depth (C_d) is given by

$$C_d = S_d \ln\left(\frac{E_0}{E_d}\right) \qquad \text{Eq. 6.1}$$

where E_0 is the incident energy dose, S_d is the sensitivity in the depth direction (with units of length), and E_d is the critical energy dose in the depth direction. The cure width (w) can be separated into the width of the illuminating beam (w_{beam}) and the excess width on either side of the beam (w_{ex}) where

$$w = w_{illum} + 2w_{ex} \qquad \text{Eq. 6.2}$$

The excess width follows a quasi-Beer-Lambert model

$$w_{ex} = S_w \ln\left(\frac{E_0}{E_w}\right) \qquad \text{Eq. 6.3}$$

where S_w is the resin sensitivity in the horizontal direction (units of length) and E_w is the apparent critical energy dose in the width direction. Another way to describe the excess width is in terms of the broadening depth (the depth at which broadening begins):

$$D_b = S_d \ln\left(\frac{E_w}{E_d}\right) \qquad \text{Eq. 6.4}$$

where D_b is the broadening depth. This predicts the depth at which broadening becomes significant, which occurs at the energy dose where $E_0=E_w$. A large value for D_b indicates that a suspension can be cured deep before it begins to broaden, while a small D_b indicates that broadening will occur at a shallower cure depth. This has a practical consequence, since deep and narrow features cannot be cured using suspensions with a small broadening depth. In the absence of broadening, the cured width is simply equal to the width of the energy distribution that is above the critical energy dose of the suspension, and the broadening depth approaches infinity. The suspension parameters S_d, S_w, E_d, E_w, and D_b can be used to quantify suspensions for use in stereolithography.

A collimated slit apparatus has been demonstrated to provide useful information on the cure profile in a ceramic suspension (see Chapter 5). This apparatus uses a collimated light source masked by a slit. A collimated slit apparatus has been shown to yield a finite intensity distribution, and can be used for suspension characterization. Chapter 5 focused on quantifying these parameters in absorption-dominated systems. This chapter will focus on the effects of scattering and refractive index on the curing properties of the suspensions.

6.1.1 Light Scattering

One analysis of scattering is the Mie scattering model. Mie scattering analyzes the interaction of the light with a particle using electromagnetic theory. It can be used to predict the amount of light that is transmitted through a slab containing dispersed particles or reflected back from the surface. Alternatively, it can be used to predict the

distribution of scattering angles off of a particle. Mie theory assumes that the scattering is occurring in dilute monodisperse solutions, where the uniform particles are assumed to be non-interacting. Additionally, it is assumed that the medium is non-absorbing, so that any attenuation of light is due to the effect of the scattering. Unfortunately, the ceramic suspensions used for ceramic stereolithography are not as simple as this. The scattering behavior can be quantified by the scattering length, l_{sc}, which is the distance over which a photon must travel before its propagation direction becomes randomized. A large scattering length corresponds to minimal scattering, while a small scattering length indicates a large degree of scattering.

Two compositional factors that are significant in scattering are the refractive indices of the ceramic powder and the liquid medium. The refractive index contrast ($\Delta n/n_0$) is defined as

$$\frac{\Delta n}{n_0} = \frac{|n_0 - n_{cer}|}{n_0} \qquad \text{Eq. 6.5}$$

where n_0 is the refractive index of the monomer solution and n_{cer} is the refractive index of the ceramic powder. The refractive index contrast relates how light diverges when it reaches an interface of the two materials. A large refractive index contrast corresponds to a large change in propagation direction, while a small refractive index contrast results in a small change in propagation direction. If the particle and the medium are index-matched ($\Delta n=0$), the interface does not disrupt the propagation direction and the light goes straight through. Ideally, suspensions used for ceramic stereolithography would be index matched with the powder and solution. However, this is not possible due to the larger refractive indices for many ceramics as compared to the refractive indices of

monomers. Additionally, the powder composition is usually chosen for its properties after binder removal, rather than for index matching.

Ceramic stereolithography requires that the suspension have a high solids loading (50-65 vol%). The monomer is simply serving as a binder for the particles, so there must be a large fraction of particles in the solution. At these high solids loadings, the assumption of dilute limit scattering no longer holds. A structure factor must be incorporated into the scattering model, to account for the cross-interactions that arise for the high volume fraction of ceramic powders.[1] The interparticle correlations can only be neglected when the interparticle spacing is less than the wavelength of light.[2] The interparticle spacing is related to the particle size by

$$\frac{d_m}{a} = \frac{\Phi_m^{1/3} - \Phi^{1/3}}{\Phi^{1/3}} \qquad \text{Eq. 6.6}$$

where d_m is the average interparticle spacing, a is the particle diameter, Φ_m is the maximum particle packing, and Φ is the volume fraction of particles. For spherical particles, the maximum particle packing can be assumed to be 63%, which is near the close-packed density for spheres.[2] Assuming a suspension contains uniform spheres at a volume fraction of 60%, a maximum particle packing of 63%, and particle size of 4.64 μm, the expected interparticle spacing is 76 nm. The interparticle spacing is much smaller than the wavelength of light (365 nm), so interparticle correlations must be accounted for in the scattering of light. The scattering length has been shown to decrease with increasing volume fraction, with a minimum around 50% for silica suspensions with a variety of particle sizes.[3] This was confirmed by Wu *et al.*, who showed that the reciprocal of the scattering length increases linearly with the volume fraction powder, provided that the solids loading was kept low.[1] Further increasing the volume fraction

resulted in a peak in the reciprocal scattering length around 50 vol%, with a decrease beyond this point.

Additionally, the suspensions use powders that have broad polydisperse size distributions. It has been shown that the scattering is not just dependent on the volume fraction of the powder, but also the sizes of the particles. Kaplan *et al*. showed that the correlation effects in a dilute suspension were dependent on the fraction of small particles in a suspension with a fixed fraction of large particles.[4] Wu *et al*. showed that the scattering length is dependent on the fraction of small particles in a fixed fraction of particles in a highly loaded suspension.[1] Finally, the suspension medium is also an absorbing medium, rather than non-interacting. The path length is important not only because of the scattering effects, but also because it results in a longer distance for the light attenuation.

Another important aspect is the strong particle size dependence for scattering. This is particularly important as suspensions have begun to include nanoparticles, such as those by Wozniak et al.[5] In ceramic stereolithography, there is a tension between the ideal particle size for sintering shrinkage, sedimentation, and light scattering. Small particles result in a larger number of scattering sites, increasing the scattering within the suspension. However, the particle size also affects other properties within stereolithography. Sedimentation is an important concern, as stereolithography uses only the surface of the suspension for photopolymerization, so the particles must not sediment out of this layer. Small particles are beneficial for sedimentation, as the sedimentation velocity scales approximately with the square of the radius, as given by Stokes' law (see Chapter 4). Thus nanoparticles are expected to limit the effects of sedimentation on the

suspension. Sintering densification is also affected by particle size, with small particles resulting in a larger sintering shrinkage. These competing effects of scattering, sedimentation, and sintering shrinkage must be considered together when optimizing ceramic suspensions for stereolithography.

Scattering is expected to be very significant to the width of the cured illumination, but little work has been done on this. The limited work plots cure width and cure depth using Gaussian sources as a function of energy.[6-11] These are limited for two reasons: they do not remove the excess broadening from the Gaussian beam from the much larger observed width and they do not provide comprehensive analyses of the resin parameters. This chapter will examine the role of scattering by varying two parameters: 1) the volume fraction of ceramic powder in the suspension and 2) the refractive index contrast between the monomer and powder. No closed form solution for the scattering length is possible for this system, so the analysis will focus on experimental results and simplified models. The refractive index contrast can be adjusted by changing the type of powder in the suspensions (silica, alumina, etc. which have different refractive indices) and through the use of inert diluents that change the refractive index of the liquid. It is important to note that changing the composition of the powder often results in a change in powder sizes and morphologies, which can affect the scattering of light as well. If inert diluents are used (such as 1-bromonaphthalene or decahydronaphthalene), these replace a fraction of the monomer. Diluents are chosen that have a different refractive index from the monomer, so that the refractive index of the liquid solution (n_0) changes.

6.1.2 Predictive Behavior

The general behaviors for the photocuring parameters of ceramic suspensions were discussed in section 2.5.1. The resin sensitivity (S_d) has been shown to be due to the additive effects of the absorption coefficients of each of the individual components as well as the scattering off of the ceramic particles. Assuming the ceramic is UV transparent, the sensitivity can be predicted with the absorption model[12; 13]

$$\frac{1}{S_d} = \frac{1}{l_{Sc}} + (1 - \Phi)(c_P \varepsilon_P) \qquad \text{Eq. 6.7}$$

where l_{sc} is the scattering length of the suspension, Φ is the volume fraction of ceramic powder in the suspension, c_P is the concentration of the photoinitiator, and ε_P is the extinction coefficient of the photoinitiator. Note that the dye terms have been omitted, as the suspensions in this chapter do not contain UV-absorbing dyes. For the change in solids loading, this will affect both the dilution of the absorption term, $(1\text{-}\Phi)c_P\varepsilon_P$, and the scattering length. As will be discussed in further detail later, the scattering length is a function of the solids loading. The cure width follows similar trends for the concentration of photoinitiator (see Chapter 5). If suspensions contain additional diluents, these affect both the absorption and the scattering of the suspension. It will be shown in section 6.3.2.1 that 1-bromonaphthalene significantly absorbs light, so the absorption model should be extended to include this concentration as

$$\frac{1}{S_d} = \frac{1}{l_{Sc}} + (1 - \Phi)(c_P \varepsilon_P + c_{Bromo}\varepsilon_{Bromo}) \qquad \text{Eq. 6.8}$$

where c_{Bromo} is the concentration of 1-bromonaphthalene in the liquid solution and ε_{Bromo} is the extinction coefficient of 1-bromonaphthalene.

Similar to the behavior of the resin sensitivity, the critical energy dose (E_d) can be predicted from the individual components in the suspension using the inhibitor exhaustion model.[13; 14] The inhibitor is exhausted at the critical energy level, E_d, which is dependent on the composition of the suspension as

$$E_d = (\gamma_{INH} c_{INH} + \gamma_{Bromo} c_{Bromo}) \frac{h\nu}{\Omega} \times \left[\frac{\frac{1}{l_{Sc}} + (1 - \Phi)(c_P \varepsilon_P + c_{Bromo} \varepsilon_{Bromo})}{c_P^2 \varepsilon_P^2} \right] \quad \text{Eq. 6.9}$$

where c_{INH} is the concentration of the inhibitors (such as oxygen or added quinones, etc), γ_{INH} is the number of radicals removed per inhibitor, γ_{Bromo} is the number of radicals that were not generated due to the presence of the bromonaphthalene, h is Plank's constant, ν is the frequency of the light, and Ω is the number of free radicals given off per photon absorbed. Note that suspensions that do not contain diluents have a concentration of bromonaphthalene that is equal to zero, so Eq. 6.9 is the same as Eq. 2.14. Neglecting the higher order terms, this can be written as

$$E_d = (1 - \Phi) \frac{h\nu}{\Omega} (\gamma_{inh} c_{inh} + c_{Bromo} \varepsilon_{Bromo}) \frac{1}{c_P \varepsilon_P} \quad \text{Eq. 6.10}$$

Below this energy, the inhibitors absorb free radicals and no curing occurs. Above this energy, free radicals are available to cause propagation of the polymerization reaction and curing occurs. It was shown in Chapter 5 that the width critical energy dose (E_w) follows similar trends for the concentration of photoinitiator in the suspension. For absorption-dominated systems, the key compositional factors are the concentration of photoinitiator, dye, and any other absorbing species. The behavior of scattering-

dominated systems is much more complex. The refraction of light at the interfaces of the powder and monomer cause the photon direction to become randomized.

It has previously been shown that changing the volume fraction of powders and the particle size will change the cure response for both the cure width and cure depth.[9; 10; 15] These observations are limited in that they are only measuring the width at two or three energy doses. They do not provide a comprehensive look at the relationship between the compositional factors and the changes that occur at a range of energy doses. Some reported on the process parameters, such as the illumination time or the drawing speed, which further limits the scope of which their results are useful. As predicted by the inhibitor exhaustion model, increasing the solids loading is expected to decrease the critical energy dose, as the ceramic powders effectively vary the concentration of the photoinitiators and inhibitors in the system. However, a better understanding of the effects of the solids loading on the cure shape is needed. A more thorough understanding of the compositional factors is needed, so that these results can be applied broadly to photopolymerization processes.

Another factor that this chapter will address is the refractive index contrast. A model is desired that incorporates the refractive index difference between the powder and monomer solution. In an earlier paper by Griffith and Halloran, it was suggested that S_d changes with refractive index difference, and that there is no effect on E_d.[16] However, this is not consistent with the results presented in the Griffith paper. The physics presented in the inhibitor exhaustion model predict that E_d should be relatively independent of the refractive indices, since these do not contribute to the scattering.

However, it will be shown in section 6.5.2 that different trends can be expected for the apparent values of E_d and S_d, due to the path length of the photon propagation.

A limitation of the absorption and inhibitor exhaustion models is that they require calculation of the scattering length for the suspensions, which is not possible to solve in closed form, but only by detailed simulation. Based on these models, it is expected that scattering affects the resin sensitivity but not the critical energy dose. Increasing the amount of scattering corresponds to a decrease in the scattering length (l_{sc}). More light is redirected to the side, causing the light to attenuate more quickly in suspensions with scattering. Stronger scattering results in an increase in $1/l_{sc}$ and $1/S_d$. The behavior of sensitivity with solids loading is more complicated, with sensitivity reaching a minimum ($1/S_d$ maximized) around Φ=0.50 due to the effects of multiple scattering. Changing the scattering is not expected to affect the critical energy dose, as this energy required for polymerization is not dependent on the path that the light takes to reach that point. These extrapolated values are used in the predictions of the suspension behavior.

6.1.3 Discussion of Griffith Results

One of the early papers on stereolithography proposed that the sensitivity could be predicted based on the refractive index contrast and a variety of other factors (such as particle size). The equation proposed by Griffith *et al*. is

$$S_d = \frac{2\langle d \rangle}{3\tilde{Q}} \left(\frac{n_0}{\Delta n}\right)^2 \qquad \text{Eq. 6.11}$$

where $\langle d \rangle$ is the average particle size, $\tilde{Q}$ is the scattering efficiency, and $\Delta n/n_0$ is the refractive index contrast.[16] This is supported by plotting the cure depth as a function of refractive index, and showing that this scales with the square of the refractive index. This

Griffith paper varied the cure depth by altering the composition of aqueous/acrylamide-based ceramic suspensions, effectively using ethylene glycol as a diluent. However, closer examination of the article shows that this model is not supported by the data. One of the plots (Figure 2a in Griffith's paper, reproduced in Figure 6.1) shows the cure depth as a function of dose for three refractive index contrasts. It can be seen that all three data sets have similar slopes, corresponding to similar sensitivities. Instead, the critical energy dose (x-intercept) is changing, although this is not discussed. So although a number of papers reference this relationship, plotting cure depth versus refractive index difference, these results are not valid.

6.1.4 Effect of Scattering on Cure Width

The above models all focus on cure *depth*, but there still is the question of cure *width*. As discussed above in section 6.1.2, scattering is often quantified by the scattering length (l_{sc}). A ceramic suspension with a large scattering length is expected to have a cured profile that is closer to that of an ideal resin. It has been shown that varying the particle concentration, size, and refractive index can change both the cured width and the cured depth in the suspension.[1; 10; 15-18] Hinczewski *et al*. has proposed a model for the linewidth of ceramic suspensions, suggesting that line width in ceramic suspensions can be predicted by modifying the equation for the linewidth of an ideal suspension (Eq. 2.8). Chapter 5 shows that their model is given by the following equation:[7]

$$w = F_1\sqrt{2}\sqrt{\ln\left(\frac{E_{max}}{E_{Hincz.}}\right)} \qquad \text{Eq. 6.12}$$

where F_1 is the equivalent beam width and E_{Hincz} is the apparent critical energy dose (which is different than E_d). However, a new model was needed, so that the broadening can be described independent of the light source.

Instead, Chapter 5 showed that the broadening in ceramic suspensions follows a pseudo-Beer-Lambert behavior. Varying the concentration of photoinitiator and dye, it was demonstrated that the pseudo-Beer-Lambert excess width follows the trends predicted by the absorption model for sensitivity and the inhibitor exhaustion model for the critical energy dose. This chapter will determine the effect that scattering has on the width sensitivity (S_w) and width critical energy dose (E_w), as well as the broadening depth (D_b).

6.2 Experimental Procedure

Photopolymerizable ceramic suspensions were prepared for a variety of compositions. Four sets of suspensions were prepared: suspensions with 40 vol% powder (either alumina (Al_2O_3), silica (SiO_2), mullite ($Al_6Si_2O_{12}$), or zircon ($ZrSiO_4$) powders), suspensions with 10% diluents (and 60 vol% SiO_2), suspensions with 20% diluents (and 60 vol% SiO_2) and suspensions with 0-60 vol% alumina powder. A summary of these suspensions is given in Table 6.1. Table 6.2 contains the material properties for each of the powders used, with the particle size distribution and a micrograph of each powder given in Figure 6.2. Note that the particle size distributions were measured by Union Process Inc. using a Microtrac S3000. Suspensions contained 4.17 ml of dispersant (Variquat CC-59, Evonik, 1.1 g/cm^3) for each 100 ml of powder. The ketone photoinitiator (Irgacure 184, Ciba, molecular weight of 204.3 g/mol) was included at the

given concentrations (listed as mol/L liquids). The remainder was the monomer: 1,6 hexanediol diacrylate (HDDA, SR238B, Sartomer, molecular weight of 226 g/mol). The monomer solution without diluents had a density of 1.020 g/cm^3 and a refractive index of 1.4560. Suspensions were allowed to homogenize by rolling for 24 hours.

Two of the sets of photopolymerizable ceramic suspensions were prepared with inert diluents added in place of a portion of the monomer. The two diluents were 1-bromonaphthalene (Aldrich, MW=207.07 g/mol, density=1.48 g/cm^3, n=1.6570) and decalin (1-decahydronaphthalene, Alfa Aesar, MW=138.25 g/mol, density=0.896 g/cm^3, n=1.4750). Either 10% or 20% of the monomer volume was replaced by a mixture of the diluents. For the 20% diluent suspension, the overall suspension composition was 60 vol% SiO_2, 2.5 vol% dispersant, 29.8 vol% monomer, 7.45 vol% diluents, and 0.0375 mol/L photoinitiator. For the 10% diluent suspension, the overall suspension composition was 60 vol% SiO_2, 2.5 vol% dispersant, 33.5 vol% monomer, 3.72 vol% diluents, and 0.042 mol/L photoinitiator. The volume ratio of the diluents varied from 0% 1-bromonapthalene/100% decalin to 100% 1-bromonaphthalene/0% decalin.

The refractive indices of the solutions were measured using a refractometer (r2i300, Reichert, error ±0.0001). The refractive index of the silica was measured using refractive index liquids (Cargille Labs, error ±0.0002).[19] The absorption of the inert diluents was also found using a UV-visible spectrophotometer (Cary 50, Varian) to determine whether there was significant absorption due to the diluents. PhotoDSC (DSC Q2000 with Photocalorimetry Apparatus, TA Instruments) was performed at an intensity of 6.5 mW/cm^2 on suspensions containing monomer, diluent, and photoinitiator to determine the effect of the diluents on the polymerization kinetics.

Linewidth specimens were prepared using the collimated slit apparatus as discussed in further detail in Chapter 5. Lines of ceramic suspension were cured using a collimated slit apparatus, which uses a 365 nm collimated light source illuminating a 200 μm wide slit to result in a controlled distribution of energy. Samples were imaged and then measured.

6.3 Results and Discussion: Effect of Refractive Index

6.3.1 Refractive Index Contrast Varied Using Different Powders

The refractive index difference between the powder and the monomer solution is expected to significantly affect scattering, so suspensions were measured varying the refractive index of the powder. The cure depth and cure width were measured for ceramic suspensions containing 40 vol% of either silica, alumina, mullite, or zircon powder. It is shown in Figure 6.3 that the cure depths fit the Beer-Lambert curing behavior, while the excess widths follow a quasi-Beer-Lambert curing behavior. This observation is significant, as the particle size, morphology, and refractive index varied between the powders. (Note that micrographs of powders are given in Figure 6.2). For example, the silica powder was spherical with an average particle size of 4.64 μm and a refractive index of 1.4603, while the mullite powder was angular with an average particle size of 25.6 μm and a refractive index of 1.654. Both of these had depths and excess widths that had a semilogarithmic dependence on energy dose (Figure 6.3A and B). This shows that the curing behavior is not limited to a certain size or shape of particles, but is consistent across ceramic suspensions. Four different powders followed the Beer-

Lambert and quasi-Beer-Lambert curing behaviors, increasing the confidence in the relationships.

The broadening behavior was quantified for these suspensions. Based on the best fit lines in Figure 6.3, the critical energies and sensitivities of the suspensions were determined. For example, the cure depth and excess width for the suspension containing 40 vol% silica are shown in Figure 6.3A. The depth sensitivity is 242±54 μm whereas the width sensitivity is 1000±33 μm. The depth critical energy dose is 2.63 mJ/cm^2 with an error range of 1.45-4.78 mJ/cm^2. Note that the error range is the range of values that are within one standard deviation of the mean value. The width critical energy dose is 195 mJ/cm^2 with an error range of 187-204 mJ/cm^2. For this composition, the broadening depth, as defined by Eq. 6.4, was 1040±270 μm. Table 6.3 contains a summary of the photocuring parameters (S_d, E_d, S_w, E_w, D_b) for all four suspensions from Figure 6.3A-D. The measured width parameters can be several times larger than the depth parameters. For the resin sensitivity, the width sensitivity was as much as four times larger than the depth sensitivity (i.e., the slope was steeper). For the critical energy dose, the width critical energy dose was as much as two orders of magnitude larger than the depth critical energy dose. Note that there were no significant trends in the resin sensitivities (S_d/S_w) or critical energies (E_d, E_w) with refractive index contrast. This can be attributed to the differences in particle size and morphology. These are significant to the scattering, so the effect of refractive index cannot be simply isolated from other scattering effects when the powder is varied.

For the suspensions varying the ceramic powder, it was found that the broadening depth decreased with the logarithm of the contrast ($\Delta n/n_q$), as shown in Figure 6.4. The broadening depth can be described by the refractive index difference as

$$D_b = -B_1 \ln\left(\frac{\Delta n/n_0}{B_2}\right) \qquad \text{Eq. 6.13}$$

where B_1 is the broadening strength and B_2 is the broadening index. Eqs. 6.4 and 6.13 can be combined to predict the relation between the width critical energy dose and depth critical energy dose for any value of refractive index contrast as

$$E_w = E_d \left[\frac{B_2}{\Delta n/n_0}\right]^{\frac{B_1}{S_d}} \qquad \text{Eq. 6.14}$$

The broadening power describes how severely the broadening depth changes with refractive index contrast. A small value for B_1 indicates that there is little change with refractive index contrast, while a large value indicates that there is a large change in the broadening depth with refractive index contrast. B_2 represents the contrast that is sufficiently large that broadening occurs for all depths. B_1 and B_2 are expected to be experimental constants that depend on the concentration of photoinitiator, incident intensity, etc. For these suspensions, the broadening strength (B_1, the slope of the semilogarithmic line) was found to be 220 μm and the broadening index (B_2, the intercept of the semilogarithmic line) was found to be 0.35.

6.3.2 Refractive Index Contrast Varied Using Diluents

A second method of varying the refractive index contrast is through the use of diluents in place of a portion of the monomer. These change the refractive index of the liquid solution. Two sets of suspensions were measured using diluents: one replacing

10% of the monomer volume with inert diluents and the other replacing 20% of the monomer volume with inert diluents. The 10% diluent suspension contained 60 vol% silica powder, 7.45 vol% diluents, and 0.042 mol/L photoinitiator. The 20% diluent suspension had 60 vol% silica, 3.72 vol% diluents, and 0.0375 mol/L photoinitiator.

6.3.2.1 Characterization of Suspensions Containing Diluents

The properties of the suspensions were measured without powder to determine the effects of the diluents on curing. The refractive indices of the 20% diluent solutions were measured as a function of the amount of diluents in the solution, as given by Figure 6.5. The solution composition maintained a constant fraction of HDDA (80 vol%) while varying the ratio of decalin and bromonaphthalene in the solution. The refractive indices varied from 1.4601±0.0001 to 1.4942±0.0001, with the refractive index increasing linearly with composition. Note that this can also be extended to give the refractive indices of the suspensions with only 10% diluents. The refractive index of the silica was determined to be 1.4603±0.0002, as measured using refractive index liquids. Thus, the magnitude of the refractive index contrasts are 0.0002±0.0003 to 0.0339±0.0003.

The absorption of the inert diluents was found using spectrophotometry to determine whether there is significant absorption due to the diluents. The concentration, c, and the molar extinction coefficients, ε, of the components are given in Table 6.4, along with the calculated absorption length (where $\alpha = c * \varepsilon$). These were measured at a wavelength of 365 nm, to match the wavelength of the UV light source in the collimated slit apparatus. Note that the concentration and molar extinction coefficient of the Variquat are not given, as the molecular weight is not provided. Instead, the absorption

of Variquat listed has been adjusted to account for the volume fraction of dispersant within the suspension. As expected, the absorbance of the photoinitiator has the largest effect on the absorbance of the overall suspension. It was found that 1-bromonaphthalene also significantly absorbs light. The remaining components absorb less than 5% of the light compared to the absorption of the photoinitiator, so will be ignored. Thus, the absorption model should be adapted for the case of suspensions containing inert diluents. For a ceramic suspension containing decalin and 1-bromonaphthalene as diluents, S_d is predicted to be given by

$$\frac{1}{S_d} = \frac{1}{l_{sc}} + (1 - \Phi)\left(c_p \varepsilon_p + c_{Bromo} \varepsilon_{Bromo}\right) \qquad \text{Eq. 6.15}$$

where c_{Bromo} is the concentration of the 1-bromonapthalene, and ε_{Bromo} is the extinction coefficient of 1-bromonaphthalene.

Photo-differential scanning calorimetry (photoDSC) was performed to compare the effect of the diluents on the curing kinetics of the system. For this, solutions were prepared that contained monomer, photoinitiator, and either decalin or bromonaphthalene. These allowed for a simple analysis of the pure systems on the photopolymerization. The heat flow was measured as a function of time under isothermal conditions, using an incident illumination of 6.5 mW/cm^2. This intensity was chosen as it is comparable to the 6.75 mW/cm^2 illumination of the collimated slit apparatus. The percentage of conversion for each of the suspensions (decalin + HDDA or bromonaphthalene + HDDA) is shown as a function of time (Figure 6.6). Both solutions began polymerizing almost instantly, with no discernable onset time. It was observed that the decalin solution polymerized faster than the solution containing bromonaphthalene, indicating a difference in polymerization rate. The decalin

suspension had an enthalpy of 459±46 J/g, while the bromonaphthalene suspension had an enthalpy of 431±16 J/g. However, this must be understood in terms of the amount of energy required for gelation. If 70% conversion is taken to correspond to the gelation point of the two solutions, then curing occurs an energy dose of 95 mJ/cm^2 for the solution containing decalin and 260 mJ/cm^2 for the solution containing bromonaphthalene. This would correspond to an increase in critical energy dose from a solution containing decalin to one containing bromonaphthalene. When these are used as a mixture replacing a portion of the monomer in a ceramic suspension, the gelation energy dose and refractive index contrast increase as the fraction of bromonaphthalene increases. Thus, it is expected that the critical energy dose will increase with refractive index contrast due to the effects of the diluent.

These analyses have shown the effect of the diluents on the suspension properties. The change in refractive index has been quantified, which is needed for the remainder of work in this chapter. Additionally, the effects of the diluent on the absorption and polymerization enthalpy have been investigated. Bromonaphthalene contributes to the absorption and the ratio of diluents affects the critical energy dose of the suspension.

6.3.2.2 Effect of Refractive Index Contrast on Cure Shape

Suspensions were illuminated with varying energy doses to determine how the shape changes with refractive index. Profiles of the largest and smallest refractive index contrasts with 20% diluents are given in Figure 6.7. For equal energy doses, the suspension with a large refractive index contrast ($\Delta n/n_0$=0.0227, Figure 6.7A) cured shallower and wider than the suspension with the small refractive index contrast

($\Delta n/n_0$=0.00014, Figure 6.7B). For instance, compare the outline of the cure profiles at an energy dose of 203 mJ/cm^2. The suspension with a large $\Delta n/n_0$ cures to a depth of 505 μm and a width of 957 μm (w_{ex}=356 μm). In contrast, the suspension with a small $\Delta n/n_0$ cures to a depth of 878 μm and a surface width of only 473 μm (w_{ex}=114 μm). Additionally, the shape of the cured region in the suspension with $\Delta n/n_0$=0.00014, (Figure 6.7B) at 203 mJ/cm^2 shows the ballooning profile, which occurs for suspensions with large amounts of forward scattering. Increasing the energy dose results in both compositions having deeper and wider cure profiles. However, the incremental increase in depth and width for large $\Delta n/n_0$ are less than the increments by which the suspension with small $\Delta n/n_0$ increases. The suspension with small $\Delta n/n_0$ cures deeper and increases its cure depth at a larger rate than suspension with large $\Delta n/n_0$. For the cure width, the suspension with small $\Delta n/n_0$ cures narrower but increases its cure width at a larger rate than the suspension with large $\Delta n/n_0$. These differences can be attributed to the large change in refractive index contrast for the two suspensions. The one suspension has a larger refractive index contrast ($\Delta n/n_0$=0.0227 versus $\Delta n/n_0$=0.00014) which means that there is more scattering occurring during the photon propagation. The increased contrast causes more of the light to get redirected to the side where it contributes to broadening, rather than propagating down and contributing to the cure depth. Additionally, more of the light will get redirected toward the surface, where it will escape the suspension. This results in smaller, broader cure shapes. Note that the suspension with small refractive index contrast (B) showed very little broadening (w_{ex}=7.3 μm) at an energy dose of 54.0 mJ/cm^2, despite a cure depth of 659 μm. The broadening increases at a large rate as the energy increases, but the cure depths remain much deeper than the suspension with larger

refractive index difference. The refractive index contrast is very significant on the shape of the cured line, due to the effects of scattering in the system.

The cure depth and cure width were measured for a variety of suspensions, each with a different refractive index contrast. The effect of refractive index on the curing behavior was measured for both sets of suspensions containing diluents. Figure 6.8A shows the change in cure depth with energy for the suspensions with increasing refractive index contrast for the suspension with 20% diluents. Note that the individual data points are not shown, only the best fit lines, for clarity. Each line is fit to the cure width or cure depth at 4-8 energy doses, with repeated measurements for each dose. It can be seen that there is little change to the slope of the cure depth with respect to energy (depth sensitivity, S_d), while the energy dose intercept (depth critical energy dose, E_d) increases with refractive index contrast. Figure 6.8B shows a different behavior for the relationship between excess width and energy dose. The width sensitivity (S_w) decreases with increased refractive index contrast, while the width critical energy dose (E_w) increases with refractive index contrast.

6.3.2.3 Effect of Refractive Index on Cure Parameters

The overall behaviors of the curing parameters were also quantified for suspensions containing 10% and 20% diluents (Figure 6.9, Figure 6.10, and Figure 6.11). For both sets of suspensions, it was found that $1/S_d$ slightly decreased with refractive index contrast, while $1/S_w$ increased with refractive index contrast (Figure 6.9). In other words, the depth sensitivity increased with refractive index contrast while the width sensitivity decreased with refractive index contrast. The width sensitivity was 1.9 to 3.7

times larger than the depth sensitivity. This difference in magnitudes is comparable to those seen with other solids loadings or powder compositions, as shown in section 6.3.1 and 6.4. From equation 6.15, it is expected that the diluent will affect both the scattering term, $1/l_{sc}$, and the absorption term, $(1-\Phi)\left(c_p\varepsilon_p + c_{Bromo}\varepsilon_{Bromo}\right)$. Increasing the refractive index contrast will increase the scattering in the suspension (corresponding to an increase in $1/l_{sc}$). Increasing the refractive index contrast corresponds to an increase in the concentration of bromonaphthalene, resulting in an increase in the absorption term with refractive index contrast. Since both of these terms increase with contrast, the reciprocal of sensitivity ($1/S_d$ or $1/S_w$) is expected to increase. Furthermore, the absorption term is maximized for the suspension with 20% bromonaphthalene (c_{Bromo}= 1.34 mol/L, c_P=0.0375 mol/L). This predicts that the largest absorption contribution to $1/S_d$ is $4.4\text{x}10^{-5}$ 1/μm for the suspensions with 20% diluents. From Figure 6.9, it can be seen that the sensitivities are on the order of $1\text{x}10^{-3}$ 1/μm, so the absorption contribution is negligible. Thus, only the scattering contribution of the bromonaphthalene has to be included, and this increases with contrast.

Increasing the refractive index contrast (through an increase in the relative fraction of bromonaphthalene in the suspension) is expected to increase $1/l_{sc}$ and the reciprocal of sensitivity. This trend was seen for the width sensitivity, but not for the depth sensitivity. Additionally, $1/S_d$ for the suspension containing only 10% diluents was smaller than that of the composition containing 20% diluents. This is surprising, as the absorption effect of the diluents was shown to be negligible. It is also important to note that the reciprocal of the width sensitivity increases with refractive index contrast while the reciprocal of the depth sensitivity decreases with refractive index contrast. The

different responses for the width and depth parameters will be discussed later in section 6.5.5. However, it is surprising that the depth sensitivities are not overlapping for the different concentrations of diluents. It is possible that the diluents are interacting with the system in some way that we do not understand. The origin of this discrepancy is not known.

The effect of the refractive index contrast on the critical energy of the suspension was also investigated (Figure 6.10). It was found that the depth critical energy dose (E_d) increased with refractive index contrast, while the width critical energy dose (E_w) decreased with contrast. These trends were consistent for both the 10% and 20% diluent suspensions. The width critical energy dose was 3.5 to 54 times larger than the depth critical energy dose. The fraction of diluents in the system was found to affect the critical energy dose. This behavior is not predicted by the inhibitor exhaustion model. However, the concentration of bromonaphthalene increases with refractive index contrast and bromonaphthalene has a higher gelation energy dose, so it is expected that the critical energy dose would increase with refractive index contrast. The width critical energy dose was larger for the suspensions containing 20% diluents than it was for similar suspensions with only 10% diluents. This can also be attributed to the different gelation energy doses for the diluents as determined from DSC.

The broadening depth decreases linearly with the logarithm of refractive index contrast, consistent with the results from section 6.3.1. Figure 6.11 shows the broadening depth for both the 10% and 20% diluent suspensions overlaid. It can be seen that the amount of diluent in suspension does not change the broadening depth. The broadening depth decreases semilogarithmically with refractive index contrast as given by Eq. 6.13.

The broadening strength (B_1) is 119 μm and the broadening index (B_2) is 0.994. Note that the error bars for the refractive index difference are also indicated. Since the error is uniform for all samples (±0.0003), this is only significant for the nearly-index matched suspension. Thus, the broadening model fits both sets of data well.

6.3.3 Compiled Relationship Between Refractive Index and Broadening Depth

The effect of the refractive index difference was also determined for the depth at broadening for all of the suspensions. The broadening depth decreases with the logarithm of the refractive index difference for a variety of suspensions. Figure 6.12 shows a comparison of suspensions that were measured with the refractive index contrast varied through the use of either inert diluents or different powders. It can be seen that for all suspensions, the broadening depth decreases with the logarithm of normalized refractive index difference with the relationship given by

$$D_b = -B_1 \ln\left(\frac{\Delta n/n_0}{B_2}\right) \qquad \text{Eq. 6.16}$$

This holds over three and a half orders of magnitude in the refractive index contrast. Furthermore, the broadening depth approaches infinity as the refractive index contrast approaches zero. An index-matched suspension ($\Delta n/n_0=0$) is not expected to exhibit this broadening behavior. Plotting all three sets of data demonstrates that this behavior is observed for suspensions with a large variety of refractive index contrasts, over three orders of magnitude overall. The physics of this are not clear, but this provides valuable information for the design of suspensions for ceramic stereolithography. The broadening model can be used to extrapolate broadening depths for ceramic suspensions.

The suspensions exhibit large variations in broadening depth. From Figure 6.4, it can be seen that the silica suspension has a large broadening depth, at 1040±270 μm, whereas the broadening depth is 285±81 μm in mullite and 143±35 μm in alumina. In the zircon suspension, the depth of broadening occurs at a cure depth of only 55.2±13.4 μm. Since most direct digital manufacturing systems have layer thicknesses of 50-200 μm, the silica or mullite suspensions can be used in stereolithography without concern for broadening. The cured line width is expected to be approximately equal to that of the beam. In contrast, an alumina or zircon suspension used in a process that has a cure depth of 200 μm is expected to have a cured line width that is larger than the beam, since the broadening depth is smaller than the cure depth.

When these suspensions are used for ceramic stereolithography, the energy dose will be set to cure to a desired depth. Each stereolithography system will have a different preferred range of energy doses that can be used, depending on the laser intensity and speed of the drawing mechanism. However, a small sensitivity is generally desired to prevent large variations in cure depth with energy fluctuations (as shown in section 3.4). Thus, if only the cure depth is accounted for, zircon suspensions appear ideal for ceramic stereolithography, since they have the lowest depth sensitivity. When the broadening of the ceramic suspensions is also accounted for, zircon suspensions are much less ideal. Their small broadening depth (D_b=55.2±13.4 μm) indicates that broadening will occur for all cure depths that are 55.2 μm or larger. Many applications require a specific type of ceramic, such as the use of silica in investment casting molds. Thus, it is important to understand the width and depth parameters for the given system to be used.

It is important to account for the broadening depth in ceramic suspensions used for photopolymerization. Note that broadening will become less of a factor as layer thickness decreases, as D_b only needs to be larger than the layer thickness. For instance, it is expected that zircon suspensions can be used for ceramic stereolithography with layer thicknesses of 50 μm or less. No broadening would be expected in this case. The onset of broadening can be understood through a hindered random walk model, as will be shown in section 6.5.3. As layer thicknesses decrease to improve the resolution of the system, broadening will become less of an issue. Additionally, the empirical relationship in Eq. 6.16 can be used to predict the effect of diluents using powders other than silica. For instance, assume that a given application requires 100 μm layers without broadening. Silica, mullite and alumina suspensions have broadening depths larger than 100 um, so can be used. However, the broadening depth of zircon is smaller than the layer thickness. An option to evaluate is whether the change in refractive index contrast due to diluents is enough to decrease the broadening depth in zircon suspensions. Using B_1=220 μm, B_2=0.35 (as found in section 6.3.1), and a maximum refractive index of the solution of 1.4942 (corresponding to 20% diluents in HDDA), the broadening depth can be predicted to be 85 μm. Thus, silica, mullite, and alumina suspensions can be used for applications with cure depths of 100 μm while zircon suspensions cannot be used, even with diluents in the solution.

6.4 Results: Effect of Solids Loading

The effect of volume fraction on the cure parameters was also measured for alumina suspensions with 0-60 vol% powder and 0.048 mol/L photonitiator. The

expected behavior of the resin sensitivity with the volume fraction is complicated, as the scattering contribution and absorption contribution are both dependent on the volume fraction of ceramic powder. This section used alumina suspensions to ensure that the observed behavior was in the scattering-dominated regime (since the refractive index contrast is 0.216 for alumina suspensions compared to that of 0.0030 for silica suspensions). The reciprocal of the width and depth sensitivities as a function of solids loading are in Figure 6.13. Note that the width sensitivity was not able to be determined for the suspension without powder (Φ=0); the samples for this composition ranged from 550-1700 μm deep without significant broadening. Overall, the reciprocal of the width sensitivity increases with the volume fraction of powder in the suspension. It is expected that the reciprocal of the sensitivity would increase with volume fraction, with a maximum around 50 vol%, as this is the behavior of the reciprocal of scattering length. This prediction is consistent with the observed behavior for the depth sensitivity. For the width sensitivity, there was no significant change with volume fraction powder.

The effect of alumina solids loading on the critical energy dose was also investigated (Figure 6.14). It was expected that the solids loading would have an effect, as it decreases the volume fraction of the liquids that are participating in polymerization as well as changes the scattering length. However, this was not observed. Instead, the depth critical energy dose and width critical energy dose did not change with volume fraction of powder. The reasons for this behavior are not known. The width values were also several times larger than the depth values. Note again that the width critical energy dose was not determined for suspensions that do not contain ceramic powder, as measurable broadening was not observed.

For the scattering-dominated alumina suspensions, it was found that the broadening depth was relatively stable with the volume fraction of ceramic powder, provided that the volume fraction was non-zero (Figure 6.15). It is important to note that the broadening depth of suspensions in the absence of powder is expected to be greater than 1700 μm. The neat suspension (without powder) was cured to a depth of 1700 without broadening observed. Curing to larger depths was not possible due to the depth of the reaction vessel and the mechanical stability of the cured segment. The negligible effect of powder on the broadening depth is important, because it suggests that the solids loading can be varied to optimize the suspension rheology and green density, without affecting the shape of the cured region.

6.5 Photon Random Walk Models

Previous sections have shown the experimental relationship between cure shape and the composition. For instance, it was shown that the cure depth and excess width fit the absorption model and inhibitor exhaustion model as the composition of absorbers (photoinitiator, dye) were varied. The effect of scattering was also quantified. However, the experimental results also demonstrated some unexpected behavior that was not predicted by either the absorption or inhibitor exhaustion model. It was observed that the sensitivity changed little with contrast, even though this was predicted to have a significant effect. Instead, the critical energy changed with contrast, even though this was expected to be independent. Furthermore, the absorption and inhibitor exhaustion models do not provide a framework for understanding how to relate the width parameters (S_d, E_d) to the depth parameters (S_w, E_w). The models predict that the values should be

the same in both directions, but this was not observed. Thus, more work was needed to investigate the physics of scattering in an absorbing medium.

6.5.1 Overview

Curing models can be used to gain insight into the curing behavior of scattering-dominated ceramic suspensions. The curing models can either account for the suspension composition in a diffusive or ballistic transport model. These differ in how they account for the propagation of light through the system. The ballistic transport models assume that light propagates straight down through the suspension. Scattering simply causes a fraction of the light to be redirected to the side, reducing the overall intensity of the light that continues in the forward direction. Examples of these types of models are the absorption model and the inhibitor exhaustion model. In contrast, a diffusive transport model assumes that the path of the photon is very random due to scattering. In this model, absorption is assumed to occur over the entire path length of the photon, rather than simply accounting for the end-to-end distance. Increasing the scattering results in a more-randomized photon path and longer path lengths for the same cure depth.

Two simplified models based off of a random walk will be used to gain insight into the physics of scattering in an absorbing medium. These assume that a change in the refractive index contrast changes the severity of the scattering. With more scattering, the total path length of the photons does not change, but the apparent cure depth changes. It will be shown that these predict that the increased tortuosity of the photons causes *apparent* changes to S_d and E_d.

The paths of the photons will be modeled assuming that scattering simply changes the propagation direction. As shown in the schematic in Figure 6.16, the model assumes that a packet of photons are travelling together, scattering as a group at the scattering sites. The initial energy dose of the photon packet is E_0. The photons travel a characteristic length, l^*, before encountering a scattering event. At this point, the photons are redirected by scattering, with the angle between the incoming and outgoing rays called the scattering angle, θ. As the photons travel, the energy attenuates as expected for a Beer-Lambert suspension, with an energy given by

$$E_1 = E_0 \exp\left(\frac{l^*}{S_d}\right) \qquad \text{Eq. 6.17}$$

The photons continue propagating for a total path length, P, until the energy has attenuated to the critical energy dose ($E=E_d$). The path length is related to the initial energy dose as

$$P = S_d \ln\left(\frac{E_0}{E_d}\right) \qquad \text{Eq. 6.18}$$

In the case of diffusive transport, the cure depth (C_d) is defined as the end-to-end distance of the photon path. Two similar models will be considered: 1) a random walk model where all scattering directions are equally probable and 2) a hindered random walk model where the scattering preferentially occurs in the forward directions. For the random walk (illustrated in Figure 6.17A), all scattering angles are equally probably, and the characteristic length is equal to the scattering length ($l^*=l_{sc}$). The hindered random walk model (Figure 6.17B) is more refined, and attempts to plot the path as it scatters between each point. In this case, the scattering angles have a distribution given by Mie scattering of an isolated particle, and the characteristic length is equal to the mean free path length

(the distance between particles).[11] These two simplified models are used to understand the scattering in an absorbing medium.

6.5.2 Photon Random Walk Model

The path of the photons is initially modeled as a three-dimensional walk, as this is the simplest case. The behavior of a random walk is well known, and used to make predictions in atomic diffusion within materials. These equations will be used to provide insight into the behavior of the photon attenuation within the suspension. The random walk model assumes that *m* steps are taken, each in direction $\vec{r}$. All steps are of the same length, *r*. The vector from the start location to the final location of the photon after *m* steps is simply equal to the sum of the vectors from each step:

$$\overrightarrow{R_m} = \overrightarrow{r_1} + \overrightarrow{r_2} + \overrightarrow{r_3} + \cdots + \overrightarrow{r_m} \qquad \text{Eq. 6.19}$$

In the case of photon diffusion, the step length is equal to the scattering length ($r = l_{sc}$). The photon random walk does not "end" until all photons are absorbed, however the end of the random walk can be taken as the end of their contribution to curing. The end of the random walk will be measured at the point where E(photon packet)=E_d, with the magnitude of the vector sum assumed to be equal to the cure depth ($R_m = C_d$).

For a traditional random walk, it can be shown that

$$\langle R^2 \rangle = mr^2 \left\{ 1 + \frac{2}{n} \sum_{j=1}^{m-1} \sum_{i=1}^{m-j} \langle \cos \theta_{i,i+j} \rangle \right\} \qquad \text{Eq. 6.20}$$

where *R* is start-to-end distance of the photon path, $<R^2>$ is the average value of R^2, $\cos \theta_{i,i+j}$ is the angle between the step vectors r_i and r_{i+j} and $<\cos \theta_{i,i+j}>$ is the ensemble

average of all values of cos $\theta_{i,i+j}$. If m is sufficiently large and the step direction is random, then <cos $\theta_{i,i+j}$>=0 and

$$\langle R^2 \rangle = mr^2 \qquad \text{Eq. 6.21}$$

Note that the photon path does not necessarily have an integer number of steps for the case of photon scattering. However, m can be approximated by dividing the total path length by the scattering length:

$$m = \frac{P}{l_{sc}} \qquad \text{Eq. 6.22}$$

Applying this to the photon random walk,

$$\langle C_d^2 \rangle = m l_{sc}^2 \qquad \text{Eq. 6.23}$$

where $<C_d^2>$ is the average value of C_d squared.

The attenuation over the path of the photons will be used to determine the cure depth as a function of intensity. The energy attenuates exponentially along this path length, with the total path length given by Eq. 6.18. Scattering simply increases the path length of the photon through the suspension. Attenuation occurs over the distance as the photon travels through the absorbing medium, due to the presence of photoinitiators and other absorbers. Combining Eqs. 6.18, 6.22, and 6.23, the following relationship can be derived between energy dose, scattering length, and cure depth:

$$C_d = \sqrt{l_{sc} S_d \ln(E_0/E_d)} \qquad \text{Eq. 6.24}$$

Eq. 6.24 predicts the cure depth for a suspension with known scattering length (l_{sc}). Note that several assumptions have been made to simplify the problem:

- The path length for C_d=l_{sc} is equal to l_{sc}. That is, ballistic transport occurs over the distance of the scattering length. The actual path length over this distance is likely to be larger, but this is a more complicated case since the scattering direction is not random.
- m is sufficiently large such that <cos θ>=0.

- Paths which extend deeper than C_d and return back are ignored. In reality, these would cause a deeper cure depth.
- The effect of the loss of photons which escape the suspension is ignored.
- The random walk model can be used to predict the number of steps given a known end-to-end distance and step length, that is $C_d^2 = \langle m l_{sc}^2 \rangle$.

The photon random walk model considers the longer path length travelled for curing to any depth, z. Eq. 6.24 can be used to predict the cure depth of a ceramic suspension, provided that the scattering length, resin sensitivity, and critical energy dose are known. A model suspension will be analyzed, with S_d=100 μm, E_d=10 mJ/cm^2 and the scattering length varying from 10 to 100 μm. The cure depth versus energy for each of these conditions, as calculated using Eq. 6.24, are plotted in Figure 6.18. Note that cure depths less than the scattering length (C_d<l_{sc}) are omitted, as these would not be accurately modeled by diffusive transport. The predicted behavior in the absence of scattering (ballistic behavior) is also shown with a dashed line. It can be seen that scattering drastically reduces the observed cure depths, due to the increase in path length. Increasing the scattering length (decreasing the amount of scattering) results in larger cure depths, but these are still significantly smaller than for suspensions without scattering.

The discrepancy between the ballistic behavior and the random walk behavior arises out of the increased path length for curing. The ballistic behavior is predicted using the absorption and inhibitor exhaustion models treat scattering as a decrease in the energy propagating in the forward direction. It is possible that different behavior is exhibited, depending on the scattering length and desired cure depth. Ballistic transport might be applicable for cases where the depth, z, is the same as the path length, while the random walk model should be incorporated when the photon path has more tortuosity

The ballistic transport model predicts that only the sensitivity is affected by scattering (not the critical energy dose). In contrast, the random walk model shows a deviation from this behavior. This is not suggesting that the physics of curing are changing with scattering, but rather that the apparent sensitivity and critical energy dose are changing. A significant limitation of the random walk model is that it does not differentiate between the width and depth curing. It is assumed that curing is equally likely in all directions, with no ability to relate the width and depth parameters.

To determine the effect of scattering length on the sensitivity and critical energy dose, apparent sensitivities and critical energy doses can be inferred from the predictions. The predicted scattering behavior in Figure 6.18 is fit to a semilogarithmic behavior at a given cure depth, characterized by the slope ($S_{d,app}$) and intercept ($E_{d,app}$). Note that $S_{d,app}$ and $E_{d,app}$ are going to be highly dependent on the cure depth, as the original function is not monotonic with the logarithm of energy. Figure 6.19 shows the apparent sensitivity (A) and apparent critical energy dose (B) as a function of scattering length. Note that small reciprocal of scattering length ($1/l_{sc}$) corresponds to little scattering while a larger $1/l_{sc}$ corresponds to more scattering. The critical energy dose and the reciprocal of the sensitivity both increased with the reciprocal of scattering length (decreasing contrast). In other words, increasing the scattering length results in an increase in the apparent sensitivity and an increase in the apparent critical energy dose. Furthermore, it can be seen that these apparent values are very different than the ballistic values represented by the dashed line in Figure 6.18. The apparent sensitivities ($S_{d,app}$) range from 2-25 μm, while the ballistic sensitivity is 100 μm. Similarly, the apparent critical energy doses ($E_{d,app}$) are 0-0.2 mJ/cm^2, while the ballistic critical energy dose is 10 mJ/cm^2. Thus, for

ceramic suspensions, increasing the refractive index contrast can be expected to change both the resin sensitivity and critical energy dose.

The experimental results presented in sections 6.3 and 6.4 can be interpreted as the apparent sensitivities and critical energy doses for the suspensions as measured with the collimated slit apparatus. Experimentally, it was found that $1/S_d$ decreases with refractive index contrast and $1/S_w$ increased with refractive index contrast (see Figure 6.9). Note than an increase in refractive index contrast corresponds to an increase in $1/l_{sc}$. The random walk model predicts that 1/S will increase with $1/l_{sc}$ (increased contrast). This does not fit the observed depth behavior, but fits the width behavior. For the critical energy dose, it was found experimentally that the width critical energy dose decreases with refractive index contrast and the depth critical energy dose increases with refractive index contrast (Figure 6.10). The random walk model predicts that the critical energy dose will decrease as $1/l_{sc}$ increases (corresponding to increasing contrast). Again, the random walk model fits the width behavior. For both the sensitivity and the critical energy dose, the random walk model fits the behavior observed in the width direction, but not in the depth direction. This could indicate that the silica suspensions with a varying refractive index contrast are in a mixed-behavior region, where both the ballistic and random walk models are important.

6.5.3 Hindered Random Walk Model

To better account for the scattering behavior in ceramic suspensions, the random walk model is modified to account for the scattering angles from the particles. The random walk model assumes that all angles are equally probable, as it is based off of the

scattering length. However, the scattering length can be the end-to-end distance of a photon that has undergone many scattering events. A suspension that is highly scattering only requires a few scattering events for the propagation direction to become randomized. In contrast, a suspension with relatively little scattering (such as silica) requires many scattering events for the propagation direction to become randomized. Over this time the direction can become randomized. The hindered random walk model looks at a more specific case of scattering, accounting for these individual events.

Several assumptions and simplifications will be made as follows:

- The scattering angle (θ) is the angle between the incoming and outgoing rays, and has a probability distribution given by Mie scattering theory for a single isolated sphere.
- The particles are monodisperse.
- The distance between scattering events can be approximated by the mean free distance

$$\lambda_d = \frac{2d}{3\Phi} \qquad \text{Eq. 6.25}$$

  where λ_d is the mean free distance, d is the particle diameter, and Φ is the volume fraction of powder in the suspension.[11]
- The distribution of incident light is given by the intensity distribution of the light source (see Figure 5.2).
- Incident light is perpendicular to surface of suspension.
- Photons that propagate out of the suspensions are terminated at that point.
- Surface reflections are ignored.

For a single photon, these assumptions are used to calculate the path taken. This is then done for each of the photons to be mapped.

This section will compare the predicted photon paths for alumina and silica suspensions. The scattering parameters for the model suspensions are given in Table 6.5; note that these particle sizes and solids loadings have been chosen to mimic the silica and alumina data presented in section 6.3.1 (see Table 6.2). To determine the scattering angles for these suspensions, the simplification will be made that the particles are

monodisperse and isolated in the suspension. This allows standard Mie scattering theory for a dilute sphere to be applied to this application, neglecting cross-correlations of secondary scattering. The scattering angles are determined using the MiePlot software, which uses the common BHMIE algorithm[20] by Bohren and Huffman to calculate the scattering. Figure 6.20 shows the predicted scattering angles for silica and alumina suspensions as calculated using the MiePlot software. Note that the intensities have been normalized so that the integrated area is the same for both compositions. From Figure 6.20, 4.64 μm silica particles ($\Delta n/n_0$=0.0030) have scattering angles within about ±4°, so scattering events do not change the direction of the photons much. The photons will mostly propagate straight ahead, with small deviations. In contrast, 1.54 μm alumina particles ($\Delta n/n_0$=0.21) have larger scattering angles, ranging up to about ±15°. This will result in a larger deviation from the forward path as compared to silica particles. Additionally, the mean free path of the alumina particles in suspension is smaller than the silica particles, as the smaller alumina particles require a larger number density of particles to reach the same solids loading. This results in more scattering events per unit length, further increasing the deviations for the alumina suspensions. The mean free path and Mie scattering angles are determined for the scattering of alumina and silica suspensions.

To understand the effect of these scattering angles on the cure shape, the paths of photons were modeled within the suspension. Each photon path represented a packet of photons with an incident energy dose of 10^3, 10^4, or 10^5 mJ/cm^2. The path of the packet was traced as it propagated through the suspension. The initial location was randomly determined using the intensity distribution of the collimated slit apparatus (Figure 5.2) as

a probability distribution. The photons initially propagate straight down. After the photon has traveled the length of the mean free path (which serves as l^*), the direction changes. This angle is randomly assigned using the distribution of scattering angles (Figure 6.20) as a probability distribution. The energy attenuated with a sensitivity (S_d) of 100 μm; propagation continued until the energy had reached the critical energy dose (E_d) of 10 mJ/cm^2. This was repeated for 500 photon paths for each composition and incident energy dose. Figure 6.21 shows the photon paths for silica and alumina suspensions, at energy doses of 10^3, 10^4, and 10^5 mJ/cm^2. The extent of these photon paths can be approximated as the cure shape, allowing for simple insight into the effects of scattering on both the cured depth and width.

The modeled cure shapes for the silica and alumina suspensions demonstrate very different behavior. The two model suspensions in Figure 6.21 vary in their scattering and mean free path length, not their sensitivity or critical energy dose. The predicted cure shape for the silica suspension is observed to be "brush-like", characterized by narrow, deep curing. Minimal broadening is seen beyond the width of the illumination (246 μm). Photons propagate generally in the forward direction, only beginning to deviate significantly at the largest energy dose (E_0=10^5 mJ/cm^2). In contrast, the alumina suspension exhibits a broad hemispherical predicted cure shape. Broadening occurs even for the lowest energy dose (E_0=10^3 mJ/cm^2), and the cure depths are much reduced as compared to the silica suspensions. Note that the path length travelled for both suspensions is the same, since the critical energy dose and sensitivity are the same. Rather, the changes in the cure depth and cure width are simply due to scattering within the suspension. Mie theory predicts that the alumina suspension scatters more than the

silica suspension, and this effect was seen in the modeled cure shapes. In terms of the cure parameters, measuring the suspension with the smaller refractive index contrast (silica) would find that the apparent depth sensitivity is larger and the apparent width sensitivity is smaller than for the suspension with the larger refractive index contrast. Similarly, increasing the refractive index contrast results in a decrease in the depth critical energy but an increase in the width critical energy. These model suspensions provide insight into the expected behavior of the cure shape as the refractive index is varied.

Although the model suspensions have different composition than the suspensions which varied diluents concentration (section 6.3.2), the photon paths can help to inform the understanding of the shapes that are observed. Figure 6.7 shows the experimental change in cure shape as a function of energy dose for suspensions with two different values of contrast. For the suspension with low contrast (Figure 6.7B, $\Delta n/n_0=0.00014$), it is observed that the cure shape is very narrow with minimal broadening for the lowest energy dose ($E_1=54$ mJ/cm^2). This is comparable to the brush-like cure shape observed in the modeled silica suspension. However, the cure shape observed in Figure 6.7B broadens with a much larger width sensitivity than the modeled brush-like suspension. The experimental cure shape for the higher contrast suspension (Figure 6.7A, $\Delta n/n_0=0.0227$) is broad, similar to the hemispherical cure shape modeled for the alumina suspension (Figure 6.21B). Note that for all suspensions, the modeled energy doses are much larger than the experimental energy doses. Furthermore, the modeled behavior predicts a much narrower cure distribution than observed experimentally. However, it

has been shown that the modeled behavior can provide qualitative insight into the broadening of ceramic suspensions.

6.5.4 Hindered Random Walk: Effect of Particle Size

The effect of particle size on the scattering shape was also investigated using the hindered random walk model. The Mie scattering angles for 1, 2, and 4.64 μm diameter particles are shown in Figure 6.22, assuming a 60 vol% silica suspension with n_0=1.4560 and n_{cer}=1.4603 (corresponding to $\Delta n/n_0$=0.0030). This shows a large change in scattering angles with particle size. For the 4.64 particles, the scattering angles are within a range of ±4°, while the 2 μm particles have scattering angles within ±10°. The 1 μm particles have the largest range, with scattering angles falling within ±20°. This is a drastic change in scattering angles as the particle size is decreased within this range.

The photon random walks are plotted in Figure 6.23 for the three particles sizes, similar to the analysis for the model silica and alumina suspensions in section 6.5.3. Again, 500 photon paths are traced, assuming a suspension with D_p=100 μm and E_d=10 mJ/cm^2. Note that the mean free path (used as the step length, l^*) scales with particle size; the mean free path lengths are 5.16, 2.22, and 1.11 μm for the particle diameters of 1, 2, and 4.24 μm, respectively. The 1 μm particles (Figure 6.23A) exhibit hemispherical curing, with significant broadening already visible at an energy dose of 1x10^3 mJ/cm^2. Increasing the energy dose results in the cure shape becoming broader and deeper at approximately similar rates. The cure depths are decreased as a result of the more tortuous random walks. The 4.64 μm particles (Figure 6.23C) cure with "brush-like" cure shapes, as discussed in section 6.5.3. These are narrow and deep, with mostly

straight cure paths. Increasing the energy dose increases the cure depth much more than for the 1 μm particles. Additionally, broadening is only evident for the large 4.64 μm particles at the largest energy dose. The 2 μm particles (Figure 6.23C) cure with an intermediate shape between that of the 1 μm and 4.64 μm particles. For the lowest energy dose ($1x10^3$ mJ/cm^2), the 2 μm particles have a brush-like cure profile, with minimal broadening seen. However, increasing the energy dose to $1x10^4$ mJ/cm^2 results in a ballooning cure profile, which is narrow at the surface and broader below the surface. Increasing the energy dose further to $1x10^5$ mJ/cm^2 results in a rounder cure shape with more broadening. It can be extrapolated that this will approach the hemispherical curing condition when exposed with very large energy doses. Experimentally, this type of behavior was seen for the silica/diluent suspension with a refractive index contrast of $\Delta n/n_0=0.00014$ (Figure 6.7B). At an energy dose of 54 mJ/cm^2, the cure shape is brushlike. However, at an energy dose of 203 mJ/cm^2, the cure profile is balloon-like, and increasing the energy dose to 608 mJ/cm^2 results in a nearly hemispherical cure shape. It has been shown that small changes in the particle size can drastically change the cure shape. This is significant, as the ceramic powders have broad particle size distributions, which are going to affect the scattering behavior of the suspension and the broadening behavior. The scattering behavior of the highly-loaded ceramic particles in an absorbing medium is complex, but simplified models have been used to provide qualitative insight into the curing behavior.

6.5.5 Relationship Between Cure Depth and Cure Width

The cure shapes in the above section provide insight into the relationship between the cure width and depth parameters. When scattering is such severe enough that each particle results in a randomized scattering angle, this means that the scattering length is on the order of the interparticle spacing. In this case, the cure shapes are hemispherical, and the width sensitivity and critical energy should be similar to the depth sensitivity and critical energy. Suspensions with little scattering (small refractive index contrast and large scattering length) cure deeper with a brush-like cure shape. Most suspensions measured for ceramic stereolithography fall between these two extremes. The incident energy dose provides a certain amount of energy that can be distributed in a variety of ways throughout the suspension. Conservation of energy has been accounted for by modeling the path of the packet of photons until it reaches the critical energy dose. This predicts that the suspension can cure deep and narrow or shallow and wide when the scattering parameters are changed. Broadening will occur at the expense of the cure depth.

The predicted cure shapes provide insight into the relationship between the width and depth parameters. A deep, narrow cured suspension (such as the one in Figure 6.21A) will have a larger sensitivity and smaller critical energy in the depth direction than in the width direction. In contrast, a wide, shallow cured suspension (Figure 6.21B) will have a smaller sensitivity and larger critical energy in the depth direction than in the width direction. It is important to note that conservation of energy does not result in cured areas that are equivalent sizes. This is because the energy can contribute to increased cross-linked density within the cured regions or can escape at the surface.

However, the conservation of energy does provide insight into the discrepancies between the width and depth parameters as refractive index contrast is increased.

When the absorption of the suspension is varied, through factors such as the concentration of photoinitiator or dye (Chapter 5), this changes the path length or number of scattering events. Thus, if there is less absorption, the photon travels farther in both the depth and the width directions. This means that the trends should be the same for the width and the depth; these parameters should increase or decrease together. For instance, both the width and depth sensitivity increase with photoinitiator concentration (see Chapter 5). As noted in Chapter 5, the absorption model held for both the width and the depth sensitivities as the photoinitiator concentration and dye concentration were varied. The qualitative predictions of the hindered random walk model are consistent with the observed behavior for cure depth and excess width.

However, when the scattering is varied, the scattering angle is changed while the path length stays the same. This means that the trends should be different for the width and the depth directions. For instance, the reciprocal of depth sensitivity is predicted to increase with increased scattering length (smaller refractive index contrast). Thus, it is expected that the reciprocal of the width sensitivity should decrease with increased scattering length. This behavior predicted by the random walk model is consistent with the experimental results presented in section 6.3.2.

Note that changing the solids loading affects both the absorption and the scattering terms. The solids loading affects the relative concentration of the photoinitiator and the dye within the suspension. Also, the scattering length is a function of the solids loading, as discussed in section 6.4. Thus, the predictions for the

relationship between the width and the depth terms will depend on the relative intensity of these two effects.

6.6 Conclusions

Scattering effects are significant to the shapes of cured lines in photopolymerization. The absorption model and inhibitor exhaustion model assume that scattering is resulting in a portion of the energy being lost to side scattering, but that the critical energy dose is a property of the inhibitors and photoinitiator in the system. These models predict that the sensitivity is affected by the scattering, but that there is no change to the critical energy dose with scattering. However, this chapter more closely investigated the role of scattering on the curing of photopolymerizable ceramic suspensions.

The effects of scattering (through refractive index contrast) on sensitivity, critical energy dose, and broadening depth were presented. The refractive index contrast (defined as $\Delta n/n_0$) was varied by changing the powder composition as well as by changing the refractive index of the monomer solution using inert diluents. It was shown that the quasi-Beer-Lambert behavior fits a wide variety of suspensions, such as silica, mullite, alumina and zircon powders. Varying the powder within the suspension did not lead to clear trends in the sensitivity and critical energy dose, and this was attributed to the wide variety of particle sizes and morphologies. However, it was discovered that the broadening depth (D_b) is proportional to the logarithm of contrast as

$$D_b = -B_1 \ln\left(\frac{\Delta n/n_0}{B_2}\right) \qquad \text{Eq. 6.26}$$

where B_1 is the broadening strength and B_2 is the broadening index.

The effect of inert diluents on the suspension properties was also determined, for suspensions replacing 10% and 20% of the monomer volume with a mixture of 1-bromonaphthalene and decahydronaphthalene. It was shown that varying the refractive index contrast can result in very different cure shapes at comparable energy levels. The depth sensitivities increased ($1/S_d$ decreased) with refractive index contrast while the width sensitivities decreased ($1/S_w$ increased). The depth critical energy doses increased and the width critical energy doses decreased with refractive index contrast. Again the broadening depth decreased with the logarithm of contrast. This relationship was demonstrated to hold across three orders of magnitude of refractive index contrast.

Finally, the effect of solids loading on the photocuring parameters was measured. The depth sensitivity decreased ($1/S_d$ increased) with solids loading while there was little change to the width sensitivity. Neither the depth critical energy dose nor the width critical energy dose changed with solids loading, which was unexpected. The broadening depth did not change with solids loading. These anomalous trends can be attributed to the competing effects of solids loading on the behavior. The volume fraction of powder affects the absorption of light by increasing the effective concentration of photoinitiator and dye in the overall suspension. However, solids loading also affects the scattering.

Two random walk models were used to investigate the curing behavior of ceramic suspensions. These treat scattering as simply redirecting the path of the photons, separating the cure depth (observed depth of cure) from the path length traveled by the photon. The random walk model assumes that all scattering angles are equally probable,

with the distance between scattering events given by the scattering length (l_{sc}). The random walk model predicts that the cure depth is related to the scattering length by

$$C_d = \sqrt{l_{sc} S_d \ln(E_0/E_d)} \qquad \text{Eq. 6.27}$$

An apparent sensitivity and critical energy dose can be defined by finding the tangent of the equation at any point. The random walk model showed that the apparent sensitivity decreased ($1/S_{d,app}$ increased) with scattering (smaller l_{sc}) while the apparent critical energy dose decreased with scattering.

The hindered random walk model was used to gain insight into the cure shape of ceramic suspensions. This model looks at the scattering that occurs off of each particle. The distribution of scattering angles are given by Mie scattering theory for dilute monodisperse spheres, and the scattering distance is equal to the mean free path length. This was done comparing the effect of silica versus alumina suspensions as well as comparing the effect of particle size. It was found that the cure shape can be characterized as brush-like, balloon-like, or hemispherical, depending on the energy dose (path length) and scattering angles. It was shown that the differences in depth (S_d, E_d) and width (S_w, E_w) can be attributed to the redirection of the path length, and that broadening occurs at the expense of the cure depth.

6.7 References

[1] K. C. Wu, K. F. Seefeldt, M. J. Solomon, and J. W. Halloran, "Prediction of ceramic stereolithography resin sensitivity from theory and measurement of diffusive photon transport," *Journal of Applied Physics,* **98**[2] (2005).

[2] R. Garg, "Stereolithographic processing of ceramics: Photon diffusion in colloidal dispersion," Ph.D. Dissertation, Princeton University, (1999).

[3] R. Garg, R. K. Prud'homme, I. A. Aksay, F. Liu, and R. R. Alfano, "Optical transmission in highly concentrated dispersions," *Journal of the Optical Society of America A-Optics Image Science and Vision,* **15**[4] 932-35 (1998).
[4] P. D. Kaplan, A. G. Yodh, and D. J. Pine, "Diffusion and Structure in Dense Binary Suspensions," *Physical Review Letters,* **68**[3] 393-96 (1992).
[5] M. Wozniak, T. Graule, Y. de Hazan, D. Kata, and J. Lis, "Highly loaded UV curable nanosilica dispersions for rapid prototyping applications," *Journal of the European Ceramic Society,* **29**[11] 2259-65 (2009).
[6] T. Chartier, C. Chaput, F. Doreau, and M. Loiseau, "Stereolithography of structural complex ceramic parts," *Journal of Materials Science,* **37**[15] 3141-47 (2002).
[7] C. Hinczewski, S. Corbel, and T. Chartier, "Ceramic suspensions suitable for stereolithography," *Journal of the European Ceramic Society,* **18**[6] 583-90 (1998).
[8] O. Dufaud and S. Corbel, "Oxygen diffusion in ceramic suspensions for stereolithography," *Chemical Engineering Journal,* **92**[1-3] 55-62 (2003).
[9] Y. Abouliatim, T. Chartier, P. Abelard, C. Chaput, and C. Delage, "Optical characterization of stereolithography alumina suspensions using the Kubelka–Munk model," *Journal of the European Ceramic Society,* **29**[5] 919-24 (2009).
[10] W. Zhou, D. Li, and Z. Chen, "The influence of ingredients of silica suspensions and laser exposure on UV curing behavior of aqueous ceramic suspensions in stereolithography," *The International Journal of Advanced Manufacturing Technology,* **52**[5] 575-82 (2011).
[11] C. Sun and X. Zhang, "Experimental and numerical investigations on microstereolithography of ceramics," *Journal of Applied Physics,* **92**[8] 4796-802 (2002).
[12] V. Tomeckova and J. W. Halloran, "Cure depth for photopolymerization of ceramic suspensions," *Journal of the European Ceramic Society,* **30**[15] 3023-33 (2010).
[13] V. Tomeckova and J. W. Halloran, "Predictive models for the photopolymerization of ceramic suspensions," *Journal of the European Ceramic Society,* **30**[14] 2833-40 (2010).
[14] V. Tomeckova and J. W. Halloran, "Critical energy for photopolymerization of ceramic suspensions in acrylate monomers," *Journal of the European Ceramic Society,* **30**[16] 3273-82 (2010).
[15] T. Chartier, A. Badev, Y. Abouliatim, P. Lebaudy, and L. Lecamp, "Stereolithography process: Influence of the rheology of silica suspensions and of the medium on polymerization kinetics – Cured depth and width," *Journal of the European Ceramic Society*[0] (2012).
[16] M. L. Griffith and J. W. Halloran, "Scattering of ultraviolet radiation in turbid suspensions," *Journal of Applied Physics,* **81** 2538 (1997).
[17] M. L. Griffith and J. W. Halloran, "Freeform fabrication of ceramics via stereolithography," *Journal of the American Ceramic Society,* **79**[10] 2601-08 (1996).
[18] C. Sun and X. Zhang, "The influences of the material properties on ceramic micro-stereolithography," *Sensors and Actuators a-Physical,* **101**[3] 364-70 (2002).

[19] R. M. Allen, "Practical refractometry by means of the microscope: with listings of index liquids, and other aids for mineralogists." R.P. Cargille Laboratories, (1954).
[20] C. F. Bohren, D. R. Huffman, and l. Wiley online, "Absorption and scattering of light by small particles." Wiley: New York, (1998).

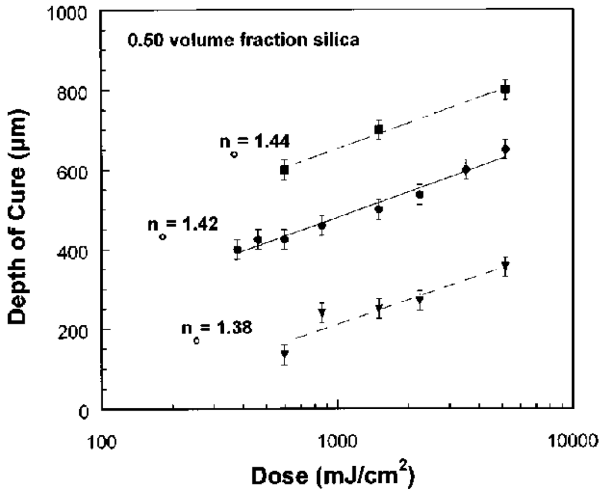

Figure 6.1 Griffith's depth of cure (µm) versus dose (mJ/cm^2) for 0.50 volume fraction silica in three aqueous UV-curable solutions. Note that the normalized refractive index difference ($\Delta n/n_0$) has been added, assuming n_{Silica}=1.56. (Griffith Figure 2a) [17]

Table 6.1 Summary of the sets of suspensions that were tested.

Description	Powder	Φ	c_P (mol/L)	% Monomer Replaced with Diluents
Vary Powder	Al_2O_3, SiO_2, $Al_6Si_2O_{12}$, or $ZrSiO_4$	0.40	0.049	--
10% Diluents	SiO_2	0.60	0.042	10%
20% Diluents	SiO_2	0.60	0.0375	20%
Vary Solids Loading	Al_2O_3	0-0.60	0.048	--

Table 6.2 Ceramic powders used in photopolymerizable ceramic suspensions, along with their average particle size weighted by volume (d_{50}), density, and refractive index.

Material (Product Name, Supplier)	Chemical Formula	d_{50} (μm)	Density (g/cm^3)	Refractive Index
Silica (Tecosphere-A, CE Minerals)	SiO_2	4.64	2.2	1.4603
Refractory-grade Mullite (MU-101, Micron Metals)	$Al_6Si_2O_{12}$	25.6	3.16	1.654
Alumina (A-152 SG, Almatis)	Al_2O_3	1.54	3.98	1.77
Zircon (Zirconium Silicate, Alfa Aesar)	$ZrSiO_4$	1.78	4.56	1.85

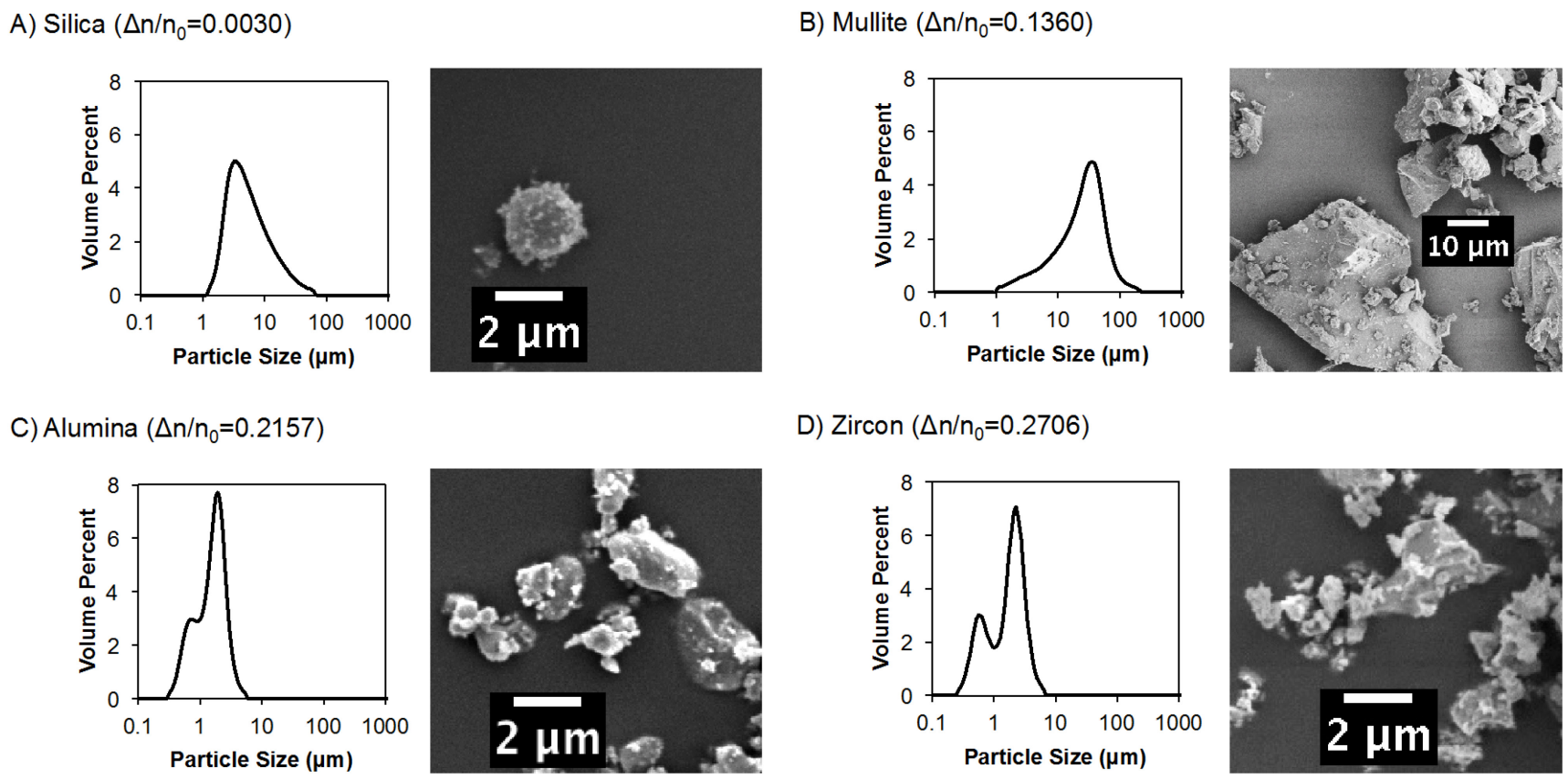

Figure 6.2 Particle size distribution and micrographs of the powders used: A) Silica (SiO_2), B) Mullite ($Al_6Si_2O_{12}$), C) Alumina (Al_2O_3), and D) Zircon ($ZrSiO_4$).

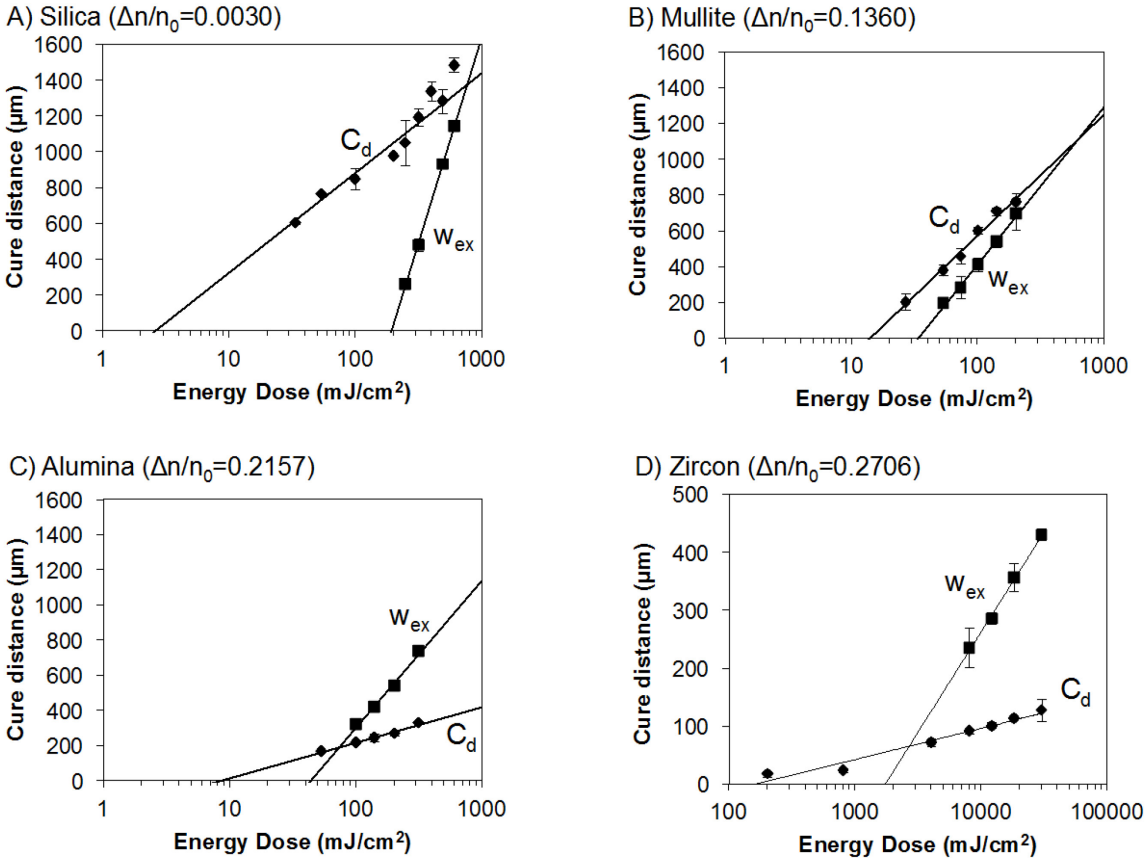

Figure 6.3 Cure profile measurements for suspensions containing 40 vol% ceramic powder (either silica (A), mullite (B), alumina (C), or zircon (D)) with 0.0486 mol/L photoinitiator. Note that the axes scaling is different for the zircon suspension.

Table 6.3 Summary of photocuring parameters for ceramic suspensions containing 40 vol% powder and 0.0486 mol/L photoinitiator. Note that the error range on the critical energies is ±σ for a lognormal distribution.

	S_d (µm)	E_d (mJ/cm^2) (error range)	S_w (µm)	E_w (mJ/cm^2) (error range)	D_b (µm)
Silica ($\Delta n/n_0$=0.0030)	242±54	2.63 (1.45-4.78)	1000±33	195 (187-204)	1040±270
Mullite ($\Delta n/n_0$=0.1360)	290±30	13.9 (11.6-16.7)	406±50	37.3 (31.0-44.8)	285±81
Alumina ($\Delta n/n_0$=0.2157)	88.2±12.5	8.73 (6.51-11.7)	365±28	44.1 (39.0-49.9)	143±35
Zircon ($\Delta n/n_0$=0.2706)	23.4±2.9	164 (69-389)	150±14	1730 (963-3120)	55.2±13.4

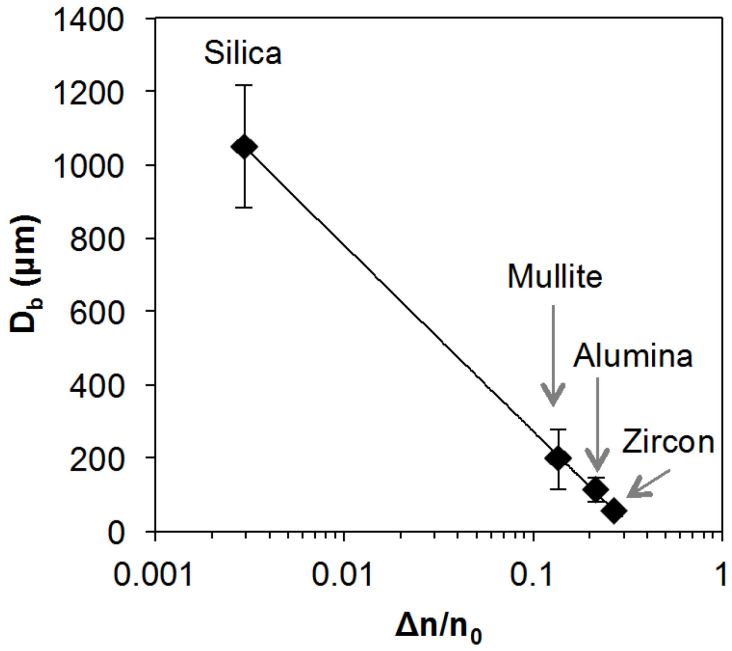

Figure 6.4 Effect of refractive index contrast ($\Delta n/n_0$) on the depth at broadening (D_b), as measured for suspensions containing silica, mullite, alumina, and zircon powders.

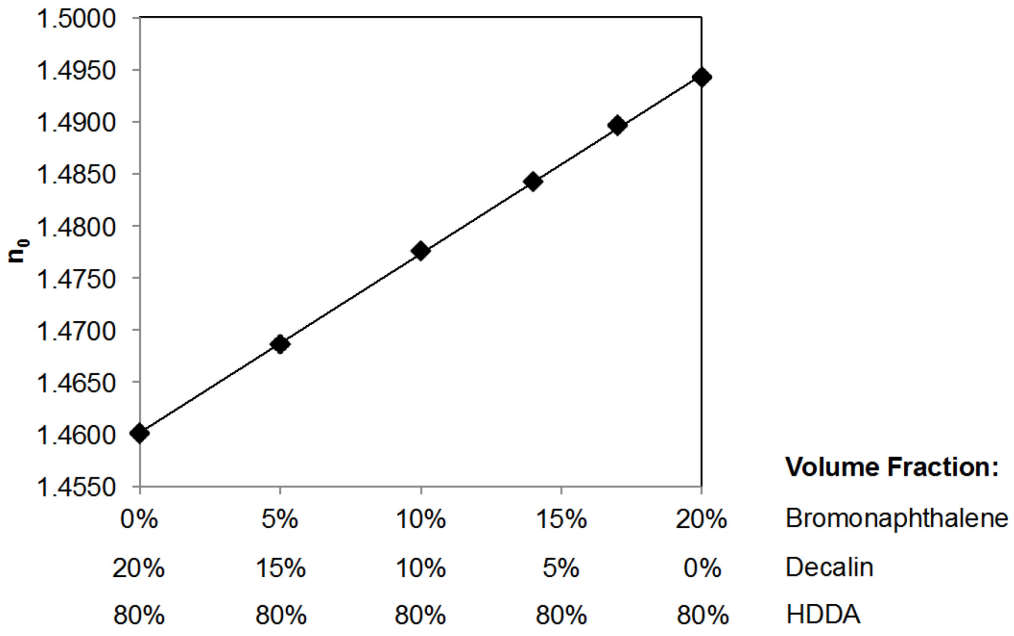

Figure 6.5 Change in refractive index as solution composition is varied using 20 vol% diluents (mixture of bromonaphthalene and decalin) and 80 vol% HDDA.

Table 6.4 Summary of absorption parameters for each component of the suspension at a wavelength of 365 nm. The concentration (c) of the component in the liquid solution is given, along with the extinction coefficient (ε). The total absorption length (α) is also calculated assuming 60 vol% powder and that 20 vol% of the monomer is replaced by diluents.

	Concentration in liquids (mol/L)	ε (L/mol-cm)	α (1/cm)
HDDA	3.38	0.00549	0.00742
Irgacure 184	0.0375	20	0.30
Variquat CC-59	--	--	0.00941
Decalin	0-1.21	0.00144	0-0.000702
1-Bromonaphthalene	0-1.34	0.268	0-0.144

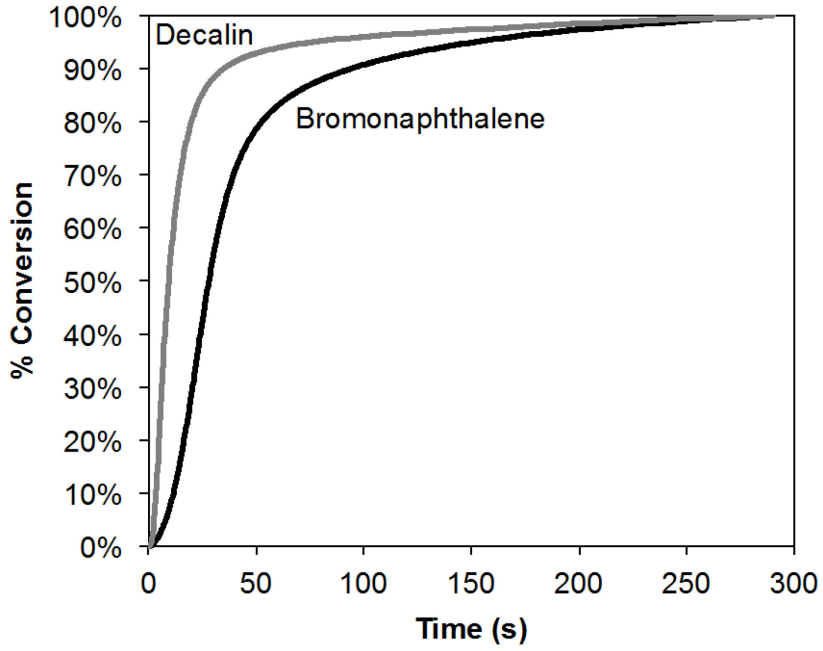

Figure 6.6 PhotoDSC solution conversion as a function of illumination time for suspensions containing 20 vol% decalin or bromonaphthalene and the remainder HDDA and 0.0375 mol/L photoinitiator, at a constant illumination of 6.5 mW/cm^2.

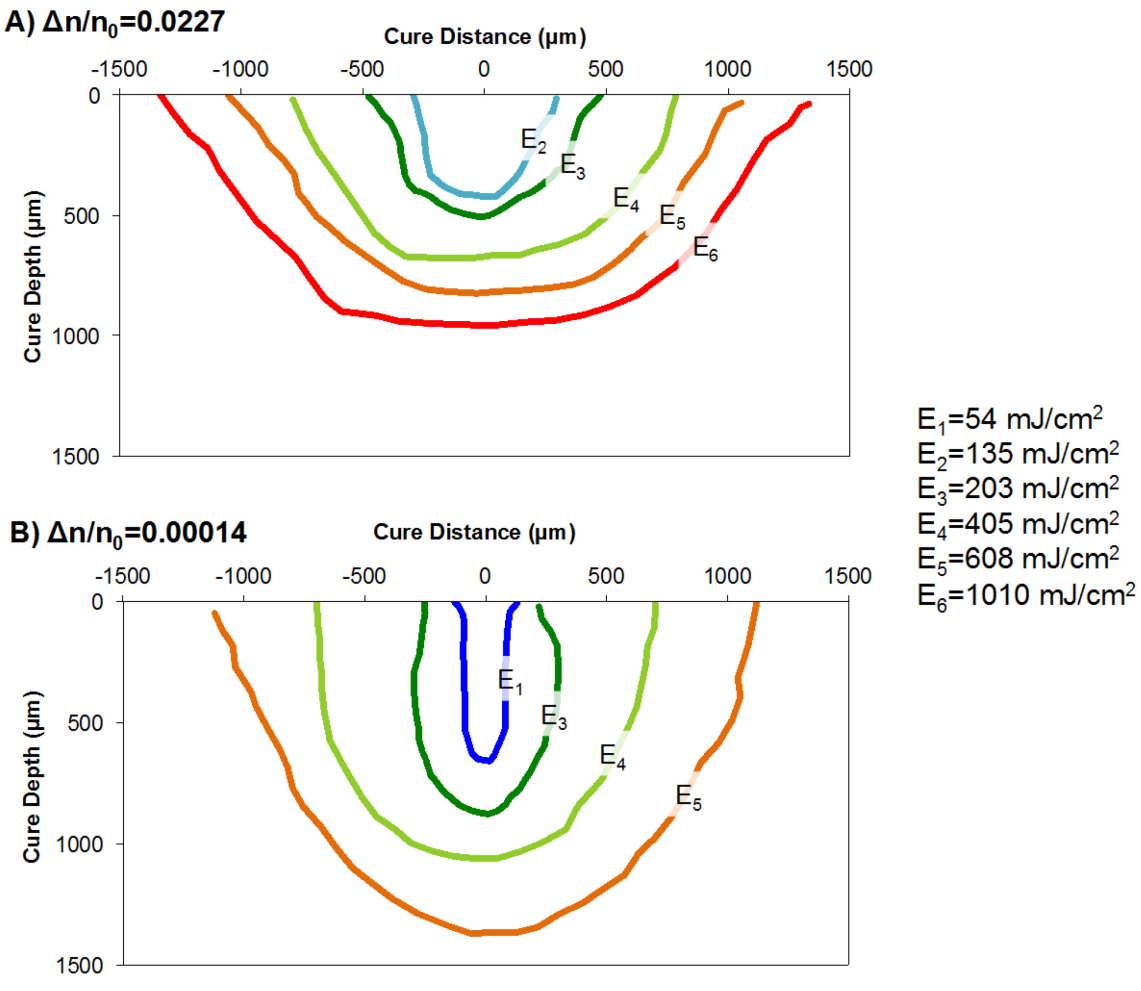

Figure 6.7 Cure profiles for suspensions containing 20% diluents with refractive index contrasts of 0.0227 (A) and 0.00014 (B). Note that the shapes are provided for a number of different energy doses.

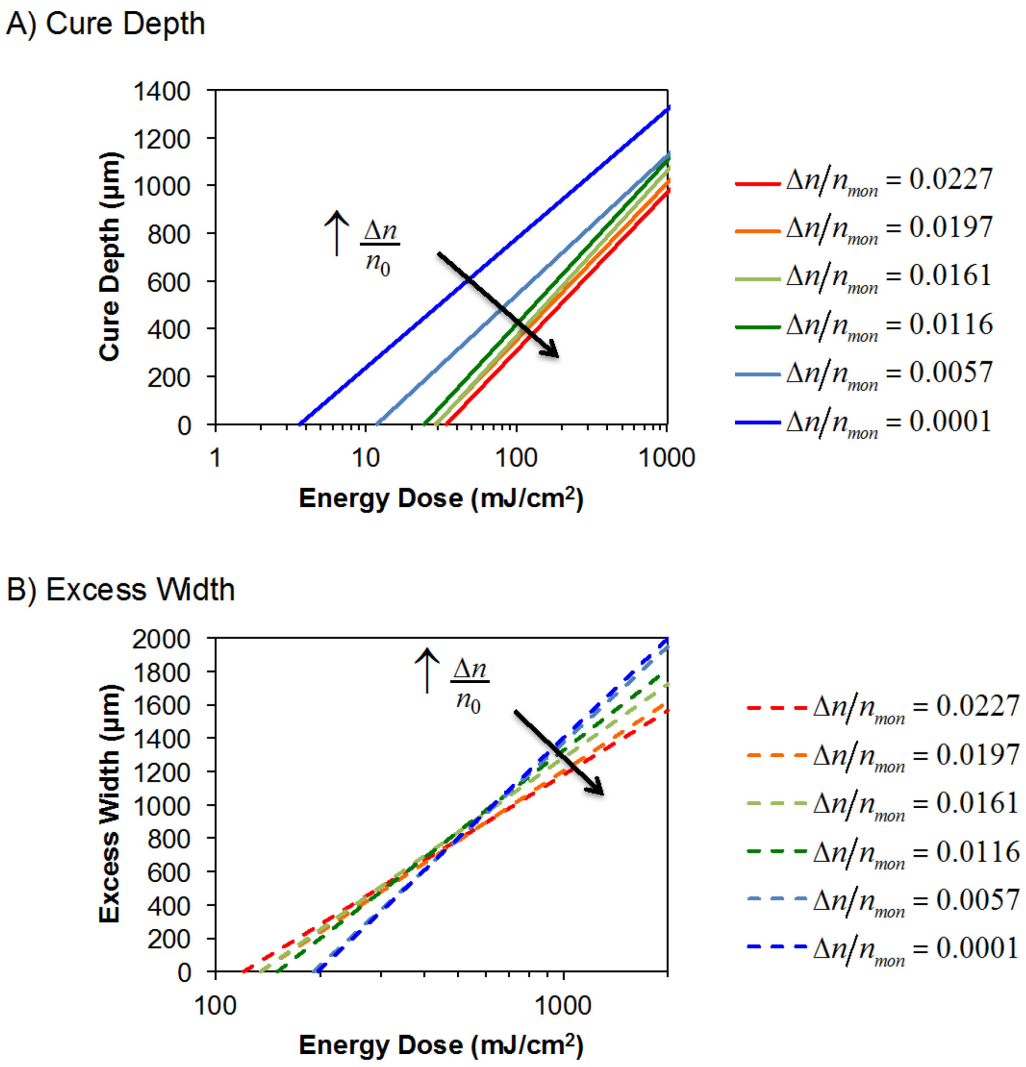

Figure 6.8 Effect of refractive index contrast on cure depth (A) and excess width (B) for suspensions with 20% diluents. The best fit line for each suspension is shown; individual data points are removed for clarity. Note that the arrow indicates the direction of increasing refractive index difference.

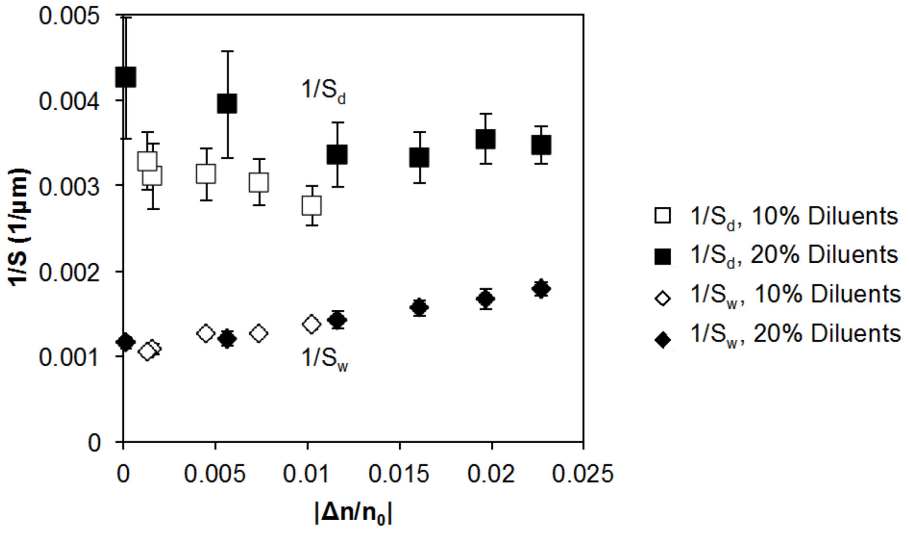

Figure 6.9 Effect of the refractive index contrast on the sensitivity of the ceramic suspensions.

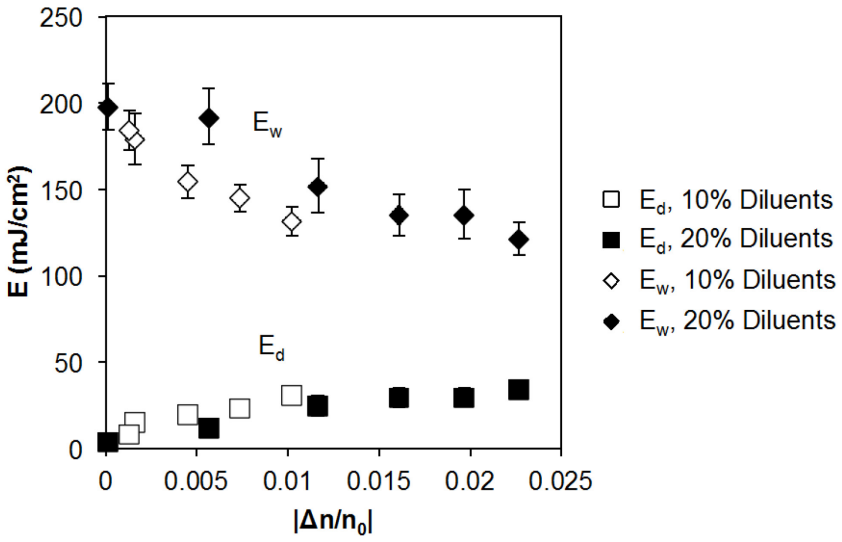

Figure 6.10 Effect of refractive index contrast on the critical energy dose of the ceramic suspensions.

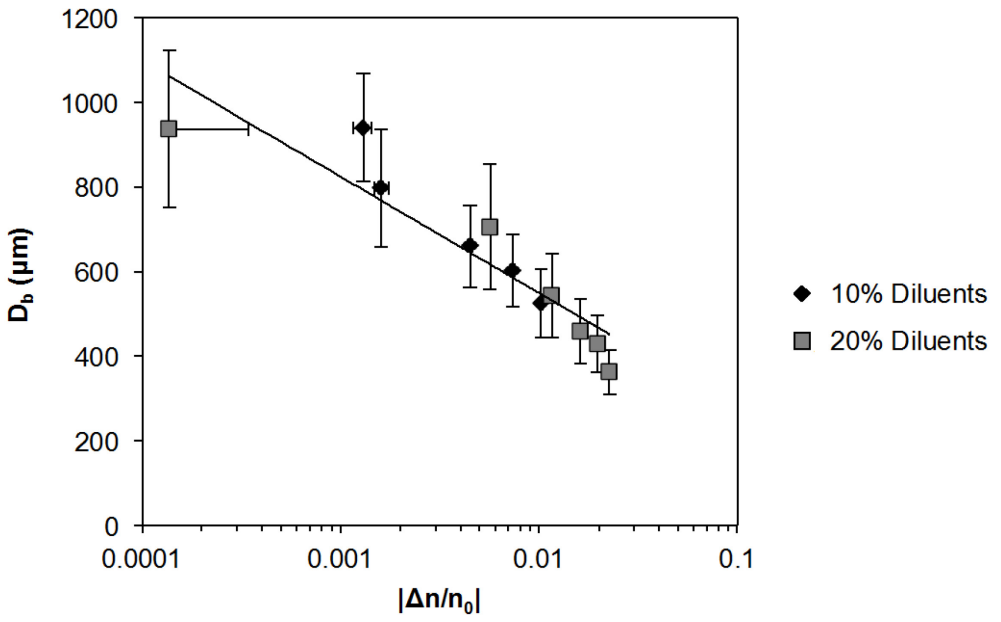

Figure 6.11 Change in broadening depth with refractive index contrast, as measured for suspensions containing 10% and 20% diluents.

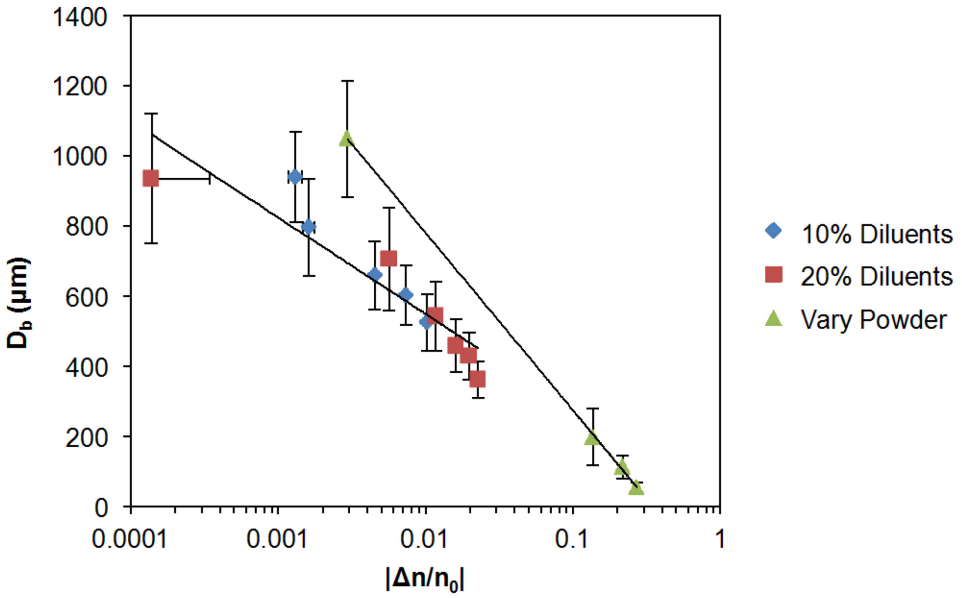

Figure 6.12 Compiled data for the broadening depth as a function of the refractive index contrast.

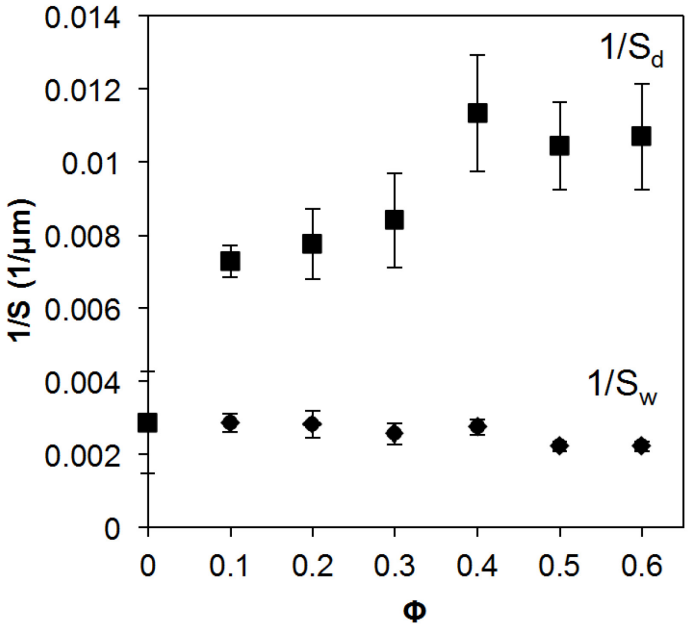

Figure 6.13 Effect of volume fraction alumina powder on the resin sensitivity of ceramic suspensions, in both the width direction ($1/S_w$) and the depth direction ($1/S_d$).

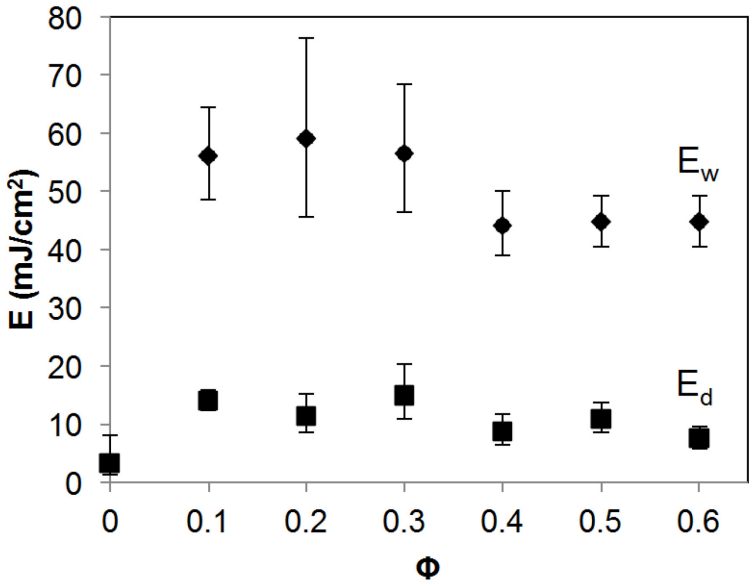

Figure 6.14 Change in critical energy dose as a function of the solids loading in the alumina suspension.

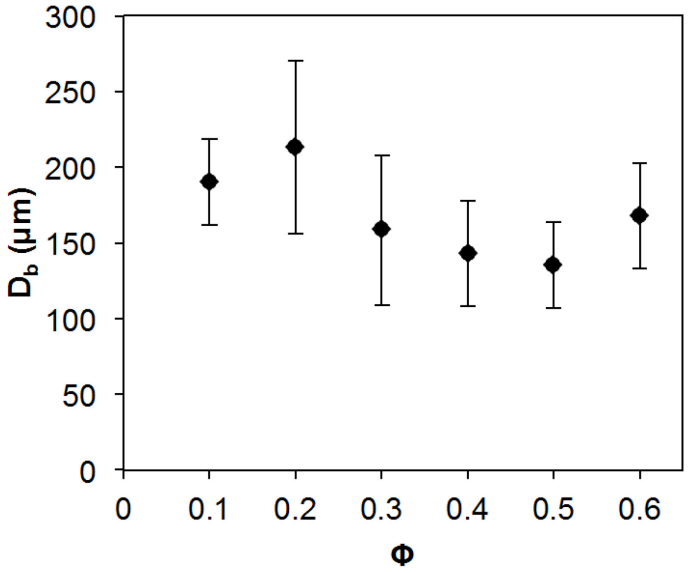

Figure 6.15 Change in broadening depth with increasing volume fraction of alumina powder.

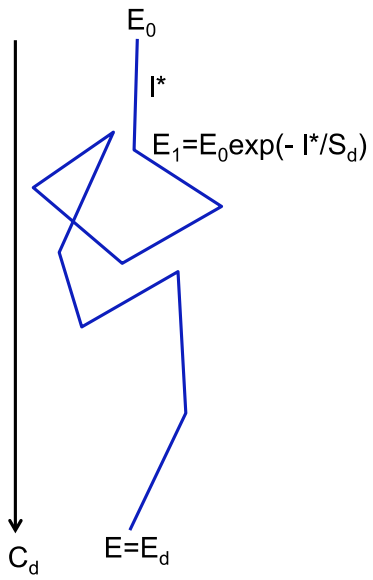

Figure 6.16 Schematic showing a sample random walk path for a packet of photons with energy dose E_0. The incident energy is given by E_0, the step length is l^*, and the cure depth is C_d.

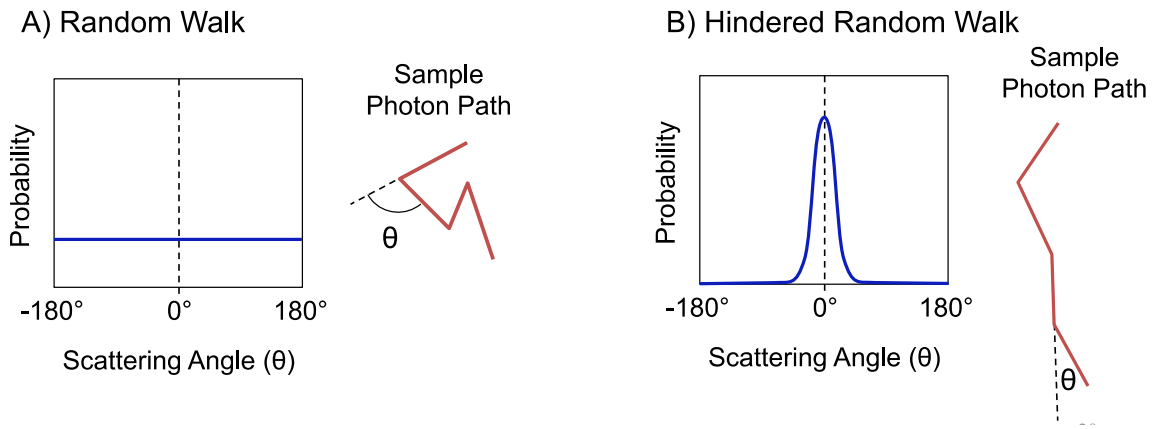

Figure 6.17 Comparison of random walk and hindered random walk models. A sample probability versus scattering angle is given for each, along with a sample photon path. Note that the scattering angle, θ, is defined as the angle between in the incoming and outgoing rays.

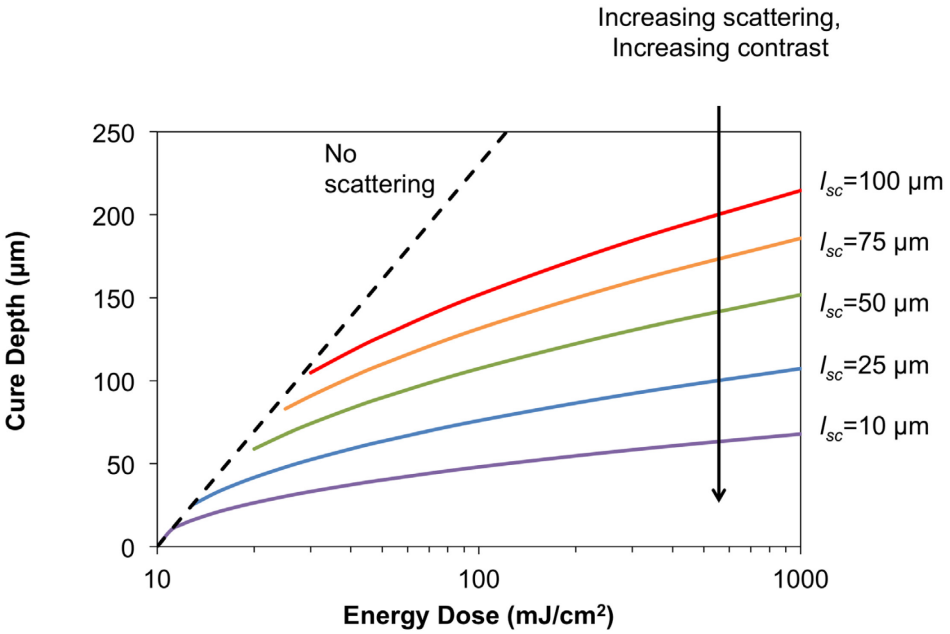

Figure 6.18 Predicted effect of scattering length on the curing of ceramic suspensions, assuming a random walk with S_d=100 µm and E_d=10 mJ/cm^2. Five scattering lengths were modeled: 10, 25, 50, 75, and 100 µm. The dashed line is the predicted behavior assuming no scattering in the suspension. Note that the random walk assumptions are not valid for cure depths less than the scattering length.

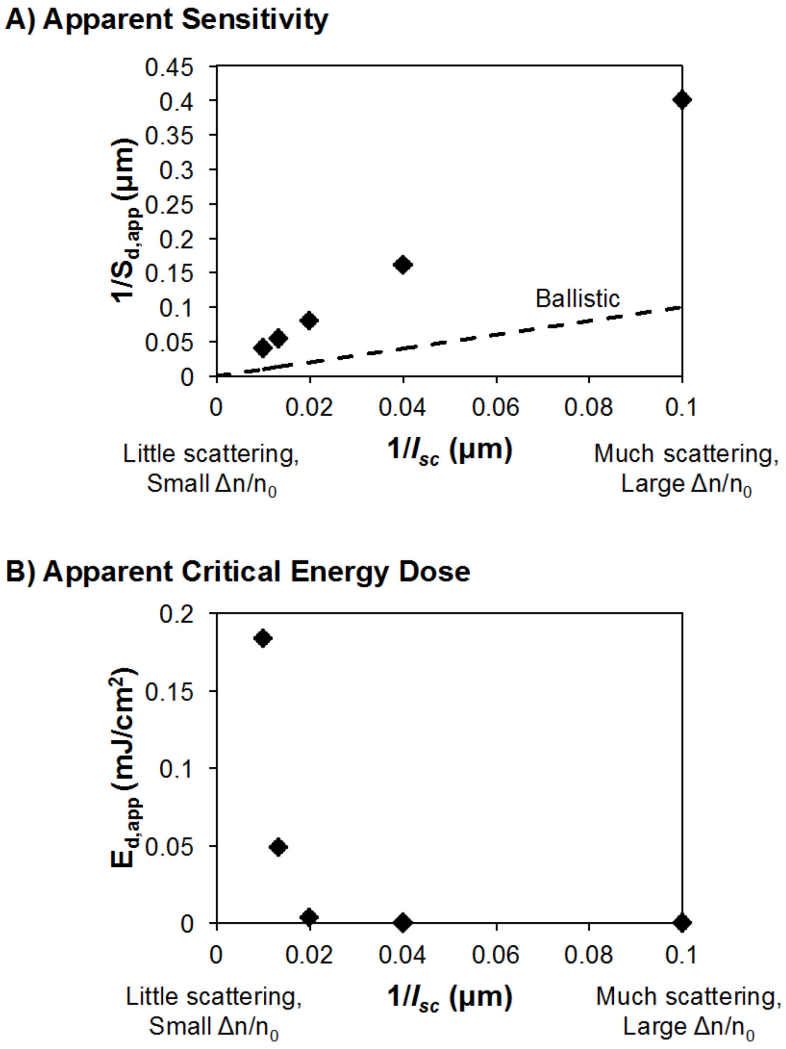

Figure 6.19 Apparent sensitivity (A) and apparent critical energy dose (B) as a function of scattering length. The dashed line in the apparent sensitivity plot (A) indicates the prediction for a ballistic, scattering-dominated suspension.

Table 6.5 Comparison of scattering parameters for hindered random walk model.

	Silica Suspension	**Alumina Suspension**
n_0	1.4560	1.4560
n_{cer}	1.4603	1.77
Contrast ($\Delta n/n_0$)	0.0030	0.21
Diameter	4.64 μm	1.54 μm
Φ	40%	40%
Mean Free Length	7.73 μm	2.57 μm
# of Photons	500	500

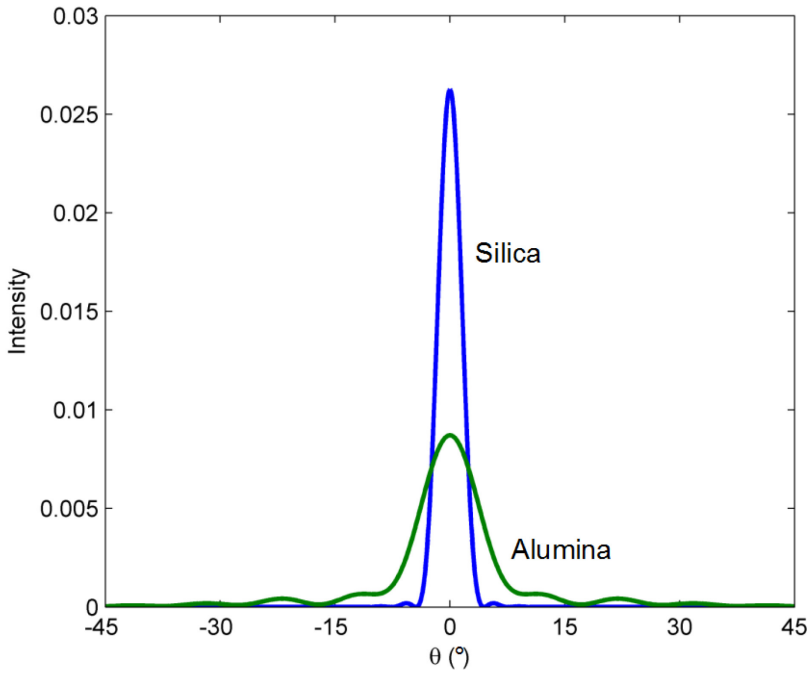

Figure 6.20 Prediction of scattering angles for alumina and silica suspensions. Note that the intensity is normalized such that the integrated area is the same for both.

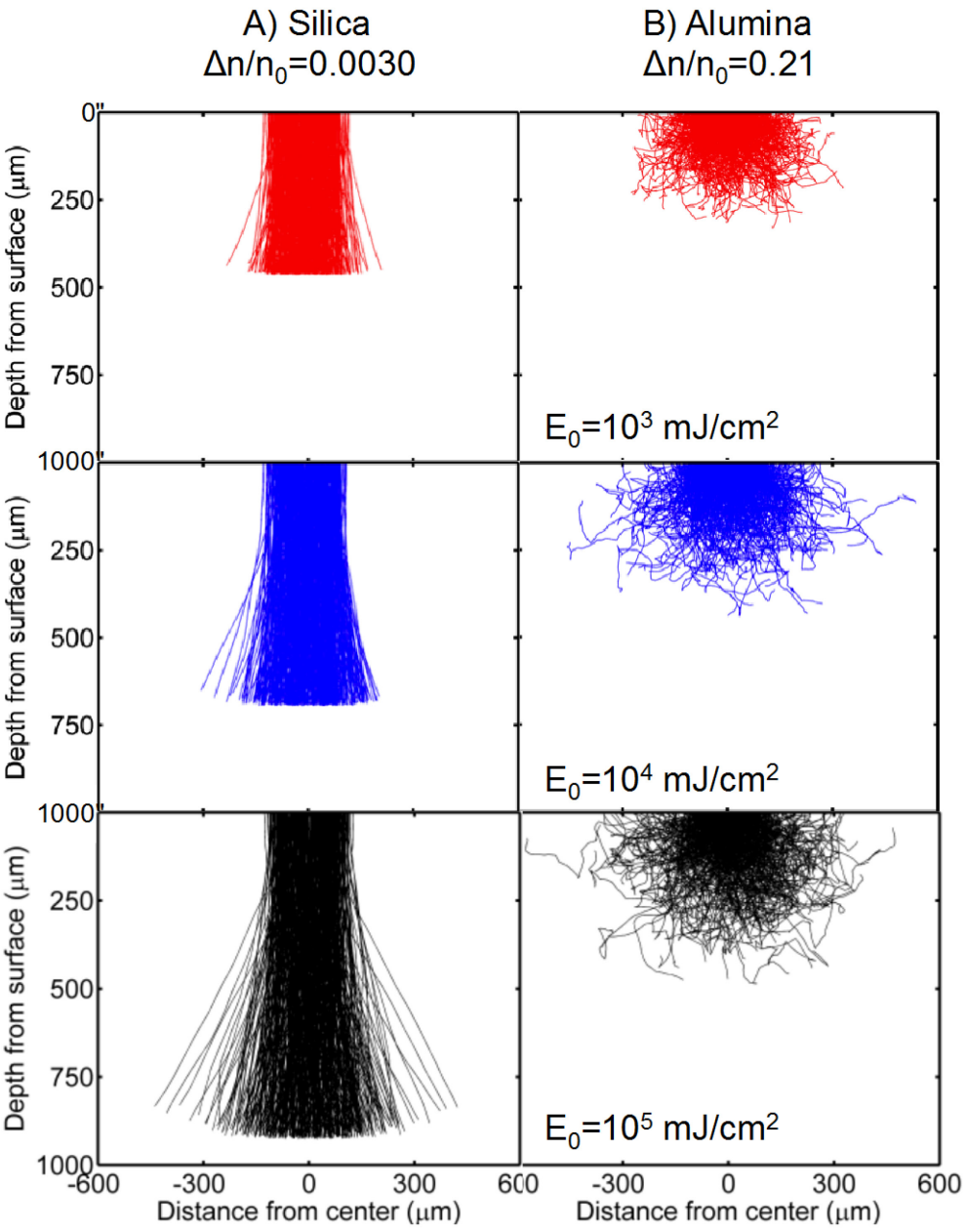

Figure 6.21 Comparison of predicted cure shape for silica (A) and alumina (B) suspensions at energy doses of 10^3, 10^4, and 10^5 mJ/cm^2.

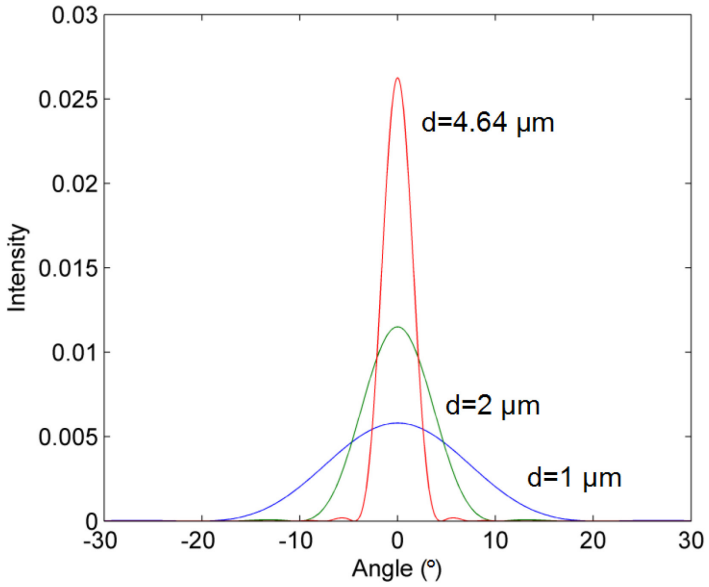

Figure 6.22 Effect of particle size on scattering angles assuming a silica suspension (n_{cer}=1.4603, n_0=1.4560) with particle sizes of 1, 2, and 4.64 µm.

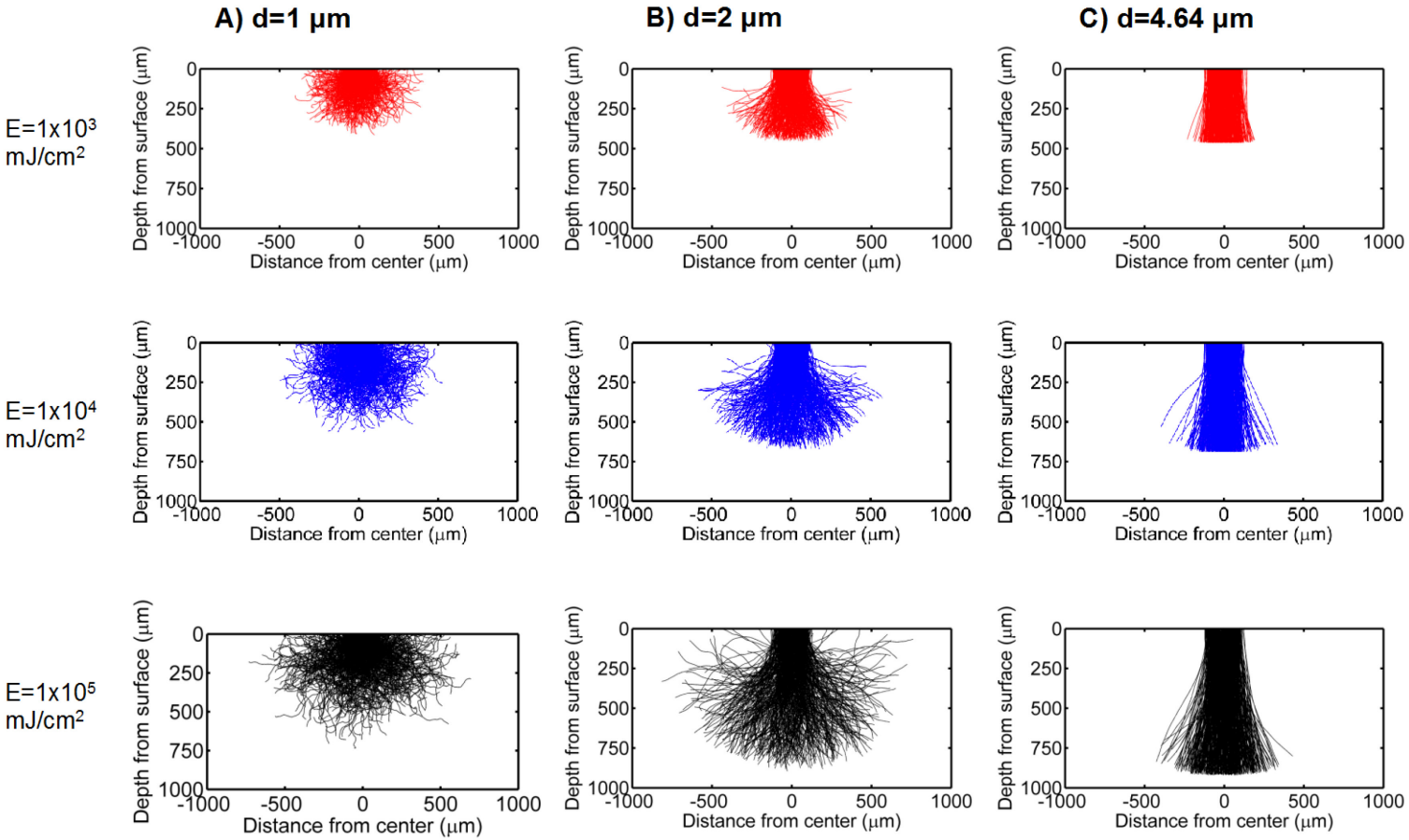

Figure 6.23 Predicted paths of 500 photons for suspensions containing silica powder with a particle size of 1 µm (A), 2 µm (B) or 4.64 µm (C) at energy doses of $1x10^3$, $1x10^4$, and $1x10^5$ mJ/cm^2.

Chapter 7

Conclusions

7.1 Resolution Limitations

Direct digital manufacturing of airfoils is needed to allow for faster production of parts and to allow for more flexibility in the designs. Ceramic stereolithography and large area maskless photopolymerization (LAMP) are two photopolymerization processes that can be used for the manufacture of complicated ceramic parts. Many different facets of the resolution of ceramic stereolithography and LAMP were investigated in this dissertation.

The machine parameters and software were found to significantly limit the resolution of ceramic stereolithography and other photopolymerization processes. Previously it was acknowledged that beam width, layer thickness, and particle size were important factors for resolution. Additionally, the initial design must account for machine limitations. For example, large overhangs or unsupported islands in the build must be prevented at the CAD design stage. Furthermore, the slicing algorithm used by the commercial software significantly affects the resolution of fine features. If the fine feature detail is lost during file preparation, then these will not be built. Fluctuations in the laser power limit the sensitivities that can be used when designing resins. The maximum sensitivity is given by

$$S_d \leq \frac{\Delta C_d}{f} \qquad \text{Eq. 7.1}$$

where ΔC_d is the maximum acceptable variation in cure depth and f is the percent fluctuation in laser power. For an application that requires no more than ±5 μm fluctuations in cure depth and uses a beam with 3% power fluctuations, the sensitivity can be no larger than 170 μm. These limitations must be accounted for in the process, so that the resolution can be optimized.

Particle settling due to gravity was shown to change the curing parameters, changing the cure depth from the nominal cure depth. Sedimentation had previously been noted as affecting the homogeneity of solids loading within the ceramic part, but has now been analyzed for its effect on the surface polymerization. This effect is significant, as ceramic stereolithography only uses the top 100 μm of suspension for photopolymerization. Changes in the solids loading at this small length scale need to be considered. A model suspension was analyzed, assuming that an absorption-dominated suspension is composed of monodisperse particles settling with a velocity given by the Stokes' equation, using the Richardson-Zaki modification for highly loaded suspensions. The absorption model and inhibitor exhaustion model were used to predict the change in the surface curing with increased settling time. It was found that this leads to the creation of a denuded surface region above the bulk, which is significant since stereolithography polymerizes the surface. At short times ($t<t_1$), the denuded region and a portion of the ceramic suspension underneath polymerize. However, at longer times, either the denuded region polymerizes without the ceramic suspension ($t>t_2$) or there is a liquid gap between layers of cured denuded region and cured ceramic suspension ($t_1<t<t_2$). The characteristic times t_1 and t_2 depend on both the curing and sedimentation constants as

$$t_1 = \frac{S_d(\Phi = 0)}{v_h} \times \ln\left(\frac{E_0}{E_d(\Phi = 0)}\right) \qquad \text{Eq. 7.2}$$

and

$$t_2 = \frac{S_d(\Phi = 0)}{v_h} \times \ln\left(\frac{E_0}{E_d(\Phi = 60\%)}\right) \qquad \text{Eq. 7.3}$$

where $S_d(\Phi=0)$ is the sensitivity of the denuded region, v_h is the hindered settling velocity, E_0 is the incident energy dose, $E_d(\Phi=0)$ is the critical energy dose of the denuded region and $E_d(\Phi=60\%)$ is the critical energy dose of the bulk suspension. Decreasing the particle size decreases the sedimentation velocity, and reduces the effect of sedimentation on the cure parameters.

For comparison, predictions on the curing were also made using experimental sedimentation data for a silica suspension. The sedimentation velocities from an analytic centrifuge were used to determine the volume fraction as a function of depth for different curing times. For a ceramic suspension with 60 vol% CE44CSS silica powder and photoactive components given in Table 4.1, it was predicted that the cure depth would decrease from about 350 μm to 75 μm over 48 hours. This is significant, as builds can take 24-48 hours. The sedimentation models using the hindered Stokes' velocity and the experimental results showed that sedimentation can significantly change the curing of the suspension and that care must be taken to ensure that the surface is homogenous.

7.2 Linewidth in Photopolymerizable Suspensions

The resolution of photopolymerization processes can also be improved by understanding the physics that influence the cure depth and cure width. The cure depth had previously been extensively modeled, but there was limited work describing the

broadening of ceramic suspensions. This work quantified the change in cure shape with energy dose for over 30 ceramic suspension compositions. As has been shown throughout literature, the cure depth, C_d, has a Beer-Lambert dependence on energy dose, and can be quantified by the semilogarithmic relationship

$$C_d = S_d \ln\left(\frac{E_0}{E_d}\right) \qquad \text{Eq. 7.4}$$

where S_d is the depth sensitivity, E_0 is the incident energy dose, and E_d is the depth critical energy dose. The line width can be divided into the width of the source and the excess width on either side due to broadening. This work showed for the first time that the excess width exhibits a pseudo-Beer-Lambert curing behavior, increasing with the logarithm of energy dose as

$$w_{ex} = S_w \ln\left(\frac{E_0}{E_w}\right) \qquad \text{Eq. 7.5}$$

where w_{ex} is the excess width, S_w is the width sensitivity, E_0 is the incident energy dose, and E_w is the width critical energy dose. Note that S_w and E_w are new parameters that are considered to be analogous to the depth parameters S_d and E_d. The dependence of S_w and E_w on composition were not known, so this work investigated this relationship. It was also discovered that the broadening parameters are linked through the broadening depth, D_b, where

$$D_b = S_d \ln\left(\frac{E_w}{E_d}\right) \qquad \text{Eq. 7.6}$$

The broadening depth is the cure depth at which broadening begins (where E_0=E_w). If the desired cure depth is less than the broadening depth, then broadening is not expected. Cure depths larger than the broadening depth will exhibit broadening.

7.2.1 Effect of Composition on Cure Depth and Excess Width as Determined Through Collimated Slit Experiments

When the concentration of photoinitiator or dye was varied in absorption-dominated systems, such as silica with a high concentration of dyes and photoinitiator, it was found that the behavior for both the depth and excess width fit the predictive models. The depth sensitivity and width sensitivity were in agreement with the absorption model, but the extinction coefficients were larger than the literature value. Furthermore, the extinction coefficients from the width sensitivities were consistently smaller than the extinction coefficients from the depth sensitivities. The critical energy doses were found to fit the inhibitor exhaustion model. Increasing $1/c_P$ increased the depth critical energy dose and width critical energy dose. Increasing $1/c_D$ did not affect the depth critical energy dose but increased the width critical energy dose. When these were combined to calculate the broadening depth, it was found that the concentration of photoinitiator does not affect the broadening depth, while the dye concentration increases the broadening depth. This can be used to tune the suspensions for their cure depth and broadening depth.

The effect of scattering on the cure depth and cure width was also measured experimentally, through the refractive index contrast ($\Delta n/n_0$). The refractive index contrast was varied by using powders with different refractive indices as well as by replacing a portion of the monomer with inert diluents that changed the refractive index of the liquid solution. The different powders did not show systematic variation to the depth sensitivity, width sensitivity, depth critical energy dose, and width critical energy dose, and this scatter was attributed to variations in particle size and morphology. Tuning

the refractive index contrast with inert diluents showed that the depth sensitivities increased ($1/S_d$ decreased) and the width sensitivities decreased ($1/S_w$ increased) with refractive index contrast. The depth critical energy dose (E_d) increased with refractive index contrast while the width critical energy dose (E_w) decreased with contrast. Furthermore, it was empirically found that the broadening depth decreased with the logarithm of contrast as

$$D_b = -B_1 \ln\left(\frac{\Delta n/n_0}{B_2}\right) \qquad \text{Eq. 7.7}$$

where B_1 is the broadening strength and B_2 is the broadening index. This behavior was consistent for all sets of suspensions varying contrast, which spanned three orders of magnitude of refractive index contrast.

The final compositional variable was the solids loading in a scattering-dominated alumina suspension. The depth sensitivity decreased ($1/S_d$ increasd) with solids loading, as expected. However, there was little change to the width sensitivity, depth critical energy dose, width critical energy dose, and broadening depth. This is attributed to the powder affecting both the attenuation and scattering of light within the suspension.

Note that this systematic study of the cure depth *and cure width* was unprecedented. Previous work had reported some limited results showing that cure width increased with energy dose or was dependent on the powder composition. However, these did not provide an understanding of the relevant models and the applicable physics.

7.2.2 Random Walk Curing Models

Two random walk models were used to investigate the curing behavior of ceramic suspensions. These traced the paths of photon packets throughout the suspension, assuming that scattering only served to redirect the energy. The photons travelled for a characteristic length, l^*, and then were scattered, with the angle between the incoming and outgoing rays given by the scattering angle. This continued on until the energy of the photon packet had fallen below the critical energy dose of the suspension.

For the first case, the scattering events were considered to be randomized, with the characteristic length equal to the scattering length ($l^*=l_{sc}$). Using three-dimensional random walk statistics, it was shown that the cure depth can be related to the scattering length by

$$C_d = \sqrt{l_{sc} S_d \ln(E_0/E_d)} \qquad \text{Eq. 7.8}$$

From this, the apparent critical energy dose and apparent sensitivity were found from the tangent at a given point. It was found that the apparent sensitivity decreased with scattering (smaller l_{sc}) and the apparent critical energy dose decreased with scattering. Note that the resin sensitivity has not changed, but rather observation has changed. However, a limitation of this model is that it does not separate the width from the depth.

The hindered random walk model accounted for the scattering off of individual particles. In this case, the characteristic length (l^*) was equal to the mean free path length, and the distribution of scattering angles was given by Mie scattering. Note that the Mie scattering angles are a simplification assuming that the particles are monodisperse and dilute, rather than highly loaded ceramic suspensions with a broad distribution of particle sizes. The hindered scattering analysis showed that different cure

shapes are possible depending on the scattering conditions, with shapes ranging from brush-like to balloon-like and finally hemispherical for the case of large scattering. For a silica suspension with 4.64 μm particles, it was shown that photon propagation is mostly straight down (scattering angles between ±4°), resulting in a brush-like cure shape. In contrast, a silica suspension with smaller 1 μm particles has scattering angles between ±20°, resulting in a hemispherical cure shape. The analysis of cure shape shows that the differences in the depth (S_d and E_d) and width (S_w and E_w) parameters can be attributed to scattering within the ceramic suspension. This is due to the conservation of energy within the suspension, so that the photon paths are either down into the suspension or redirected to the side. Broadening comes at the expense of cure depth. The modeled behavior was qualitatively consistent with the measured changes, although the magnitudes of the energy doses and cure distances do not match. However, it was shown that the simplified scattering behavior of the hindered random walk model is sufficient to demonstrate the effect of path length on the cure width and depth of ceramic suspensions with scattering.

7.3 Future Work

Despite the gains that have been made, more work is still needed to improve the resolution of ceramic stereolithography. One specific need is for a rigorous statistical analysis of the processing variables. For example, the binder burnout schedule was developed through trial and error, but has not been quantitatively assessed. It would be useful to run large numbers of samples, to know the variation within a given processing condition and to know how changing ramp rates and hold times affects the part. This

would also be useful as the process is scaled up, to know whether changes are due to the process or the natural variation within the system. Additional areas that can be looked at include the polymerization shrinkage, sintering shrinkage, and other dimensional changes related to the casting process. More generally, more work needs to be done on the process of getting a ceramic green body to a sintered part with the desired dimensions.

Specifically related to line broadening, more work can be done to develop a predictive model for the excess width. This work focused on presenting the excess width as a new parameter for stereolithography and describing the relationship between this and compositional factors. However, changing the composition (such as using a different photoinitiator) would require a repeating the analysis. It would be useful to know how these compositional factors interact with each other, or to be able to predict how wide the line will be for a given photoinitiator. A predictive model for the excess width, similar to the predictive models for the cure depth, would aid suspension formulation.